On the modelling of the unstable breaching process

Weij, D.

DOI
10.4233/uuid:5d4e0db3-c50c-4f33-b261-c3ec7514139e

Publication date
2020

Document Version
Final published version

Citation (APA)
Weij, D. (2020). *On the modelling of the unstable breaching process*. [Dissertation (TU Delft), Delft University of Technology]. https://doi.org/10.4233/uuid:5d4e0db3-c50c-4f33-b261-c3ec7514139e

On the modelling of the unstable breaching process

On the modelling of the unstable breaching process

Proefschrift

ter verkrijging van de graad van doctor
aan de Technische Universiteit Delft,
op gezag van de Rector Magnificus prof. dr. ir. T.H.J.J. van der Hagen,
voorzitter van het College voor Promoties,
in het openbaar te verdedigen op 2 april 2020 om 10:00

door

Dave WEIJ

Civiel Ingenieur, Technische Universiteit Delft, Nederland
geboren te Amstelveen, Nederland.

Dit proefschrift is goedgekeurd door de

promotor: prof. dr. ir. C. van Rhee,
en de copromotor: dr. ir. G.H. Keetels

Samenstelling promotiecommissie:

Rector Magnificus	voorzitter
Prof. dr. C. ir. van Rhee	Technische Universiteit Delft, promotor
Dr. ir. G.H. Keetels	Technische Universiteit Delft, copromotor
Onafhankelijke leden:	
Prof. dr. ir. C. Vuik	Technische Universiteit Delft
Prof. dr. ir. W.S.J. Uijttewaal	Technische Universiteit Delft
Prof. dr. ir. A. Bezuijen	Universiteit Gent, België
Dr. ir. W.P. Breugem	Technische Universiteit Delft
Dr. J. Chauchat	Université Grenoble Alpes, Frankrijk

Keywords: Dredging, numerical modelling, turbidity currents, breaching.

Printed by: Ipskamp Printing.

Front & Back: Photo by Pok Rie from Pexels.

Compiled on: March 5, 2020

ISBN 000-00-0000-000-0

An electronic version of this dissertation is available at
`http://repository.tudelft.nl/`.

Summary

Breaching is an important production mechanism for stationary suction dredgers. It is a process occurring in submerged sandy slopes, which mostly occurs in dense sandy soils with a low permeability. The process is initiated by the formation of a slope under water, whose angle is steeper than the internal friction angle, called the breach face. For dredging related breaching, this steep slope is created by a suction dredger, but it can also be formed after initial shear failure, caused by over steepening due to erosion, an earthquake, or an outwardly directed water flow. During breaching process, this steep slope is semi-stable due to negative pore pressure. Instead of a shear failure, particles are released one by one from the breach face, making it seem like the breach face is slowly moving backwards. The released particles form a density current that flows away from the breach face, and can be collected by a stationary suction dredger. When the size of the breach face increases over time, we have an unstable breach.

In recent years, the breaching process has lost popularity as a production mechanism in favour of trailing suction hopper dredgers and cutter suction dredgers, However, stationary suction dredgers are still used in many smaller scale sand collection projects, and damage due to unstable breaching still occurs. Furthermore, unstable breaching has also caused several large scale slope failures unrelated to sand collection, causing an increased interest in the mechanism in recent years. This thesis focuses on the development of a numerical model capable of modelling the unstable breaching process.

To support the development of this model large scale laboratory experiments were carried out. The experimental setup consist of a tank with a height of 2 meters, a length of 5.1 meters and a width of 0.5 meters, with glass panels for observation on one side. The tank is divided into two parts, by a impermeable removable gate, which can be lifted vertically. A breach is initiated by filling the tank with water, filling one side of the tank with sand, and lifting the gate. By choosing the correct height and slope of the breach,

unstable breaches could be triggered. During these experiments the size and frequency of larger slides during the breaching process was recorded. It was found that slides occur more frequently with steeper breach faces. Unexpectedly, these slides were not found to increase the speed of the breach face. The experiments also showed that the formula used to predict slope angles forming at the toe of the breach, predict a steeper slope than observed.

A numerical model capable of modelling the unstable breaching process should be able to model:

- Turbulent turbidity currents, and their interaction with surrounding water.
- The slides frequently occurring during breaching, for this we require a model which can reproduce the transition from static to yielding soil, and the large scale deformations after this transition.
- The interaction of the turbidity current with the dense sandy soil: The pick-up of sediment from the bed, and the sedimentation of particles from the turbidity current to the bed

The created model is an extension of an existing mixture model (SettlingFOAM), suitable for modelling sand-water mixtures with sand concentrations up to 30%. This model was extended to be able to model higher concentrations of sand (>50%), where there will be sustained contact between particles, and friction forces between particles will dominate the flow. In this regime, the mixture will remain static unless a large enough shear stress, called the yield stress, is applied. The model achieves this by modelling the sand-water mixture as a Bingham-like fluid with a yield stress. Numerically this is implemented as a fluid with a viscosity dependent on the shear rate and yield stress. To determine the yield stress, the effective pressure needs to be known. This effective pressure is calculated using the mixture pressure and the momentum balance of the water. The model also includes dilatancy, and its effect on the pore pressure.

This model is able to model the flow of sand-water mixtures, the formation of a sand bed due to settling, the soil mechanical behaviour of the dense bed, erosion of the sand bed by a flow, and the formation of negative pore pressure due to dilation. The model is also able to reproduce the (unstable) breaching process in both 2D and 3D simulations.

Samenvatting

Bressen is een belangrijk productiemechanisme voor zandwinning met winzuigers. Het is een proces dat voorkomt bij hellingen van zand onder water. Het komt vooral voor in dichtgepakt zand met een lage doorlatendheid. Het bresproces start met het ontstaan van een stuk helling steiler dan de inwendige wrijvingshoek van het zand. Dit steile stuk wordt de breswand genoemd. Bij bressen gerelateerd aan zandwinning, wordt deze steile wand gevormd door een zuigkop, maar het is ook mogelijk dat deze gecreëerd wordt door een afschuiving als gevolg van erosie, aardbevingen, of grondwater stroming. Tijdens het bres proces is dit steile stuk semi-stabiel door negatieve poriën druk. In plaats van een afschuiving, laten zandkorrels een voor een los van de breswand, waardoor het lijkt alsof deze langzaam achteruit beweegt. De losgelaten korrels vormen een dichtheidsstroming die van de breswand af stroomt, en kan worden opgezogen door een winzuiger. Als de grootte van breswand groeit dan spreken we over een instabiele bres.

De laatste jaren wordt het winnen van zand vooral gedaan door sleephopperzuigers en snijkopzuigers, in plaats van winzuigers die gebruik maken van het bresproces. Maar voor kleinschalige zandwinprojcten wordt nog steeds gebruik gemaakt winzuigers, en schade door instabiele bressen komt hier nog steeds voor. Daarnaast hebben instabiele bressen ook meerdere, niet aan baggeren gerelateerde, grootschalige oevervallen veroorzaakt. Dit zorgde voor een groei aan interesse voor het proces. Dit proefschrift richt zich op het ontwikkelen van een numeriek model dat dit bresproces kan modelleren.

Ter ondersteuning van de ontwikkeling van dit model zijn grootschalige laboratoriumproeven uitgevoerd. De opstelling bestond uit een bak met een hoogte van 2 meter, een lengte van 5.1 meter en een breedte van 0.5 meter, met aan één kant glazen wanden zodat het proces geobserveerd kon worden. De bak was in tweeën gedeeld door een wand die opgetild kon worden. Een bres werd geïnitieerd door de gehele bak te vullen met water, één helft van de bak te vullen met zand, en de wand op te tillen. Door de hoogte en de helling van de

bres te variëren kon een instabiele bres geïnitieerd worden. Tijdens de experimenten werden ook grotere afschuivingen waargenomen. Deze afschuivingen kwamen vaker voor bij een steilere breswand. Onverwacht, bleek dat de totale erosiesnelheid niet verhoogd werd door deze afschuivingen. The experimenten lieten ook zien dat de formule voor het voorspellen van de hellingen aan de teen van de bres een steilere helling dan geobserveerd voorspelde.

Een numeriek model dat het instabiel bresproces modelleert moet het volgende kunnen modelleren:

- Turbulente dichtheidsstromingen en hun interactie met de omgeving.
- De grotere afschuivingen. Hiervoor is een model nodig dat de overgang van statisch naar afschuivende grond kan modelleren, en de grote vervormingen tijdens deze afschuiving.
- De wisselwerking tussen de dichtheidsstromging en de zandbodem: De erosie van de bodem door de stroming, en het sedimenteren van zand vanuit de stroming.

Het ontwikkelde model is een uitbreiding van een bestaand mengselmodel (SettlingFOAM), geschikt voor het modelleren van zand-water mengsels tot een concentratie van 30%. Dit model is uitgebreid om het geschikt te maken voor het modelleren van hogere concentraties zand (>50%), waar er langdurig contact bestaat tussen zanddeeltjes, en wrijvingskrachten belangrijk worden. In dit regime zal het mengsel niet afschuiven totdat een schuifspanning, groter dan de zogenaamde vloeispanning, wordt toegepast. Dit effect wordt nagebootst door het zand-water mengsel te modelleren als een Bingham-vloeistof met een bijbehorende vloeispanning. In numerieke zin is dit geïmplementeerd als een vloeistof met een viscositeit afhankelijk van de vloeispanning en de afschuifsnelheid. Om de vloeispanning te bepalen is de effectieve spanning nodig. Deze effectieve spanning wordt berekend met behulp van de mengseldruk en de massabalans van de continue fase (water). Het model bevat ook dilatantie en het effect hiervan op de poriëndruk.

Met dit model kan de stroming van zand-water mengsels, de formatie van een zandbodem als gevolg van sedimentatie, erosie van de zandbodem, afschuivingen, en het ontstaan van negatieve poriëndruk als gevolg van dilatantie worden gemodelleerd. Met dit model kunnen ook (instabiele) bressen worden gemodelleerd in zowel 2D- als 3D-simulaties.

Contents

Chapter 1

Introduction

Breaching is an important production mechanism for stationary suction dredgers. Therefore much research was devoted to this process (Meijer and Os, 1976; Breusers, 1977; van Rhee and Bezuijen, 1998). They also found that the breaching process can become unstable, which in turn can lead to loss of land as seen in Figure 1.1 In recent years, however, the breaching process has lost popularity as a production mechanism in favour of trailing suction hopper dredgers and cutter suction dredgers, leading to a decrease in research on the topic.

Figure 1.1: A lake shore damaged by the unstable breaching process at Hooidijk, 2008. (Source: D.R. Mastbergen)

However, stationary suction dredgers are still used in many smaller scale sand collection projects, and damage by unstable breaching still occurs. This occurred, for example, in 2008, in the Dutch town of Staphorst, where dredging

activity initiated the breaching process, which resulted in the damage shown in Figure 1.1 (De Groot and Mastbergen, 2008), and during the nineties many failures due to unstable breaching occurred in sand production pits in the Dutch province Overijssel Mastbergen (2001). Increased scale of dredging activities also increases the chance of a breach becoming unstable.

Furthermore, unstable breaching has also caused several large scale slope failures unrelated to sand collection, causing an increased interest in the mechanism in recent years. For example, between 2011 and 2014, Beinssen et al. (2014) monitored a stretch of beach adjacent to a tidal inlet in Australia, called Amity Point, and recorded 44 breaching related failure events. In September, 2015, an event occurred nearby at Inskip Point, Australia, resulting in a slowly regressing erosion scarp of eventually 200 meters wide, which swallowed part of a camping site. In this case the process was initiated by oversteepening by erosion due to tidal currents, however a breach failure can also be initiated by dredging activity. Breaching failures also occurred in 2007, during the construction of a sludge depot in Hollandsch Diep. And breaching was also identified as a source for large oceanic turbidity currents (Mastbergen and Van Den Berg, 2003; Eke et al., 2011).

Breaching is a process occurring in submerged sandy slopes, which mostly occurs in dense sandy soils with a low permeability (van Rhee and Bezuijen, 1998; Mastbergen and Van Den Berg, 2003). The process is initiated by the formation of a slope under water, whose angle is steeper than the internal friction angle, called the breach face. For dredging related breaching, this steep slope is created by a suction dredger, but it can also be formed after initial shear failure, caused by over steepening due to erosion (As happened at Inskip Point), an earthquake, or an outwardly directed water flow. Because a slope steeper than the internal friction angle is not stable, it will start to move, and shear deformation occurs. This shear deformation can be accompanied by dilatancy, i.e. the increase of pore volume, especially in dense sands. Because the compressibility of the pore water is negligible, this increase in pore volume is accompanied by an inflow of water, driven by a decrease in pore pressure inside the sand. The decrease in pore pressure leads to an increased effective pressure between grains, leading to an increased resistance against shear deformation.

It is possible that at a certain point the pore pressure decreased so much, that no further acceleration of shear deformation occurs. When the permeability of the sand is low, this point is reached at very small shear deformations. The sand will appear stable, while at the front sand particles are released one by one as water flows into the sand, to accommodate dilation. These particles are pulled down by gravity and together form a turbidity current. This results

in a steep breach face slowly regressing away from its original position, while releasing sand particles into a turbidity current (Figure 2.1). This current can be used by the dredgers to collect sand without moving, as the current transports sand toward the suction mouth. This current interacts with the slope downstream of the breach face through erosion and sedimentation.

A breach can be stable or unstable. When the breach is unstable, the breach face increases in size over time (See Figure 1.2). When this happens, of the process can go on for a long time, sometimes exceeding a day. The end result can be large sections of land disappearing into the water, as seen in Figure 1.1.

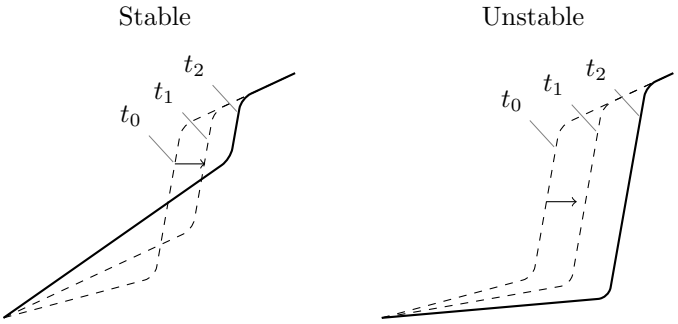

Figure 1.2: The difference between stable and unstable breaching.

1.1 Observed breach failures

Unstable breaches have been observed in a variety of environments. Unstable breaches can occur along rivers, at beaches near tidal inlets, near sand collection activity, and during the construction of submerged sandy slopes.

Bank failures in the Mississippi river are common. The Waterways Experiment Station documents, and classifies these bank failures as either shear failure, or flow failure. Shear failures are failures by sliding, which only cause damage close to the river. During a flow failure on the other hand, the failure can reach up to 100 metres inland. One such flow failure was observed near Montz, Louisiana (Figure 1.3).

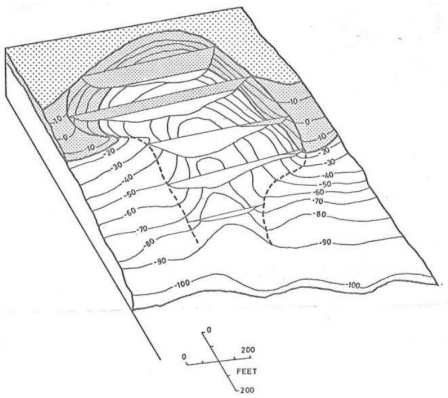

Figure 1.3: Isometric view of the failure at Montz, Louisiana, 1973. (Taken from Padfield (1978)).

These kind of failures occur multiple times each year. For example, between 1954 and 1964, 37 flow failures have been observed (Caldwell, 1966). Initially these failures were seen as the result of liquefaction (e.g. Hvorslev (1949)). However, soil samples showed no pockets of loose soil near the failures, and, according to eyewitness reports, many failures took place over several hours or even days. Therefore, Torrey III et al. (1988) and Padfield (1978) concluded that liquefaction is unlikely, and these failures are probably the result of breaching, triggered by a shear failure after oversteepening of the river bank due to erosion.

Mastbergen (2001) identifies several breach failures in the Dutch province Overijssel, between 2001 and 1997, reaching up to 36 metres inland. These breach failures are all triggered by collection of sand by suction dredging in lakes with soils consisting mostly of dense sands.

In 2007, during the construction of a sludge depot in Hollandsch Diep, 4 failures were observed. The amount of soil that was moved during these failures was estimated to be between $10\,000\,\mathrm{m}^3$ to $200\,000\,\mathrm{m}^3$. Deltares concluded that at least some of the failures were caused by unstable breaching (van der Ruyt et al., 2008). In 2008, in the Dutch town of Staphorst, dredging for sand collection initiated the breaching process, which resulted in the damage shown in Figure 1.1 (De Groot and Mastbergen, 2008).

Between 2011 and 2014, Beinssen et al. (2014) monitored a stretch of beach adjacent to a tidal inlet in Australia, called Amity Point. Here breaching is likely triggered by oversteepening due to erosion by the tidal current.

They recorded 44 breaching related failure events. The aftermath of one such breaches, with a width of approximately 90 metres, can be seen on satellite images (Figure 1.4). The largest of these resulted in the loss of 2980 m^2 of beach. In September, 2015, a similar event occurred nearby at Inskip Point. A beach collapse resulting in a slowly regressing erosion scarp of eventually 200 meters wide developed, which swallowed a four-wheel drive vehicle, a caravan and a camper trailer (Shipway, 2015). Similar events have been observed near tidal inlets in the south of France (Nedelec and Revel, 2015), and on the Dutch island Ameland (Rijkswaterstaat, 2017).

Figure 1.4: Before and after a breach failure at Amity Point. Satellite images at 2-8-2014 (left), and 18-8-2014. Taken from Google Earth.

1.2 Previous Research

A description of the breaching process was first published by Breusers (1974), who describes the formation of steep walls after the insertion of a suction tube into a layer of sand, which move away from the suction tube with a constant speed. The performed tests were used by Breusers (1977) for the optimisation of dredging by suction dredgers. Breusers (1977) also created a theoretical formula to estimate the velocity at which the steep walls move away from the suction tube. This velocity was called the wall velocity. This velocity depends on the initial porosity and permeability, and the porosity and permeability just before particles are released, and the angle of the wall.

Meijer and Os (1976) created a numerical model to estimate the steady state pore pressures, for a steady state breach, with constant wall height, angle, and velocity. They did this by linking the change in pore volume due

to change in stresses, to pore pressures, using the Darcy equation. They assumed a fixed, rectangular, profile, which moves in the horizontal direction with a constant wall velocity. They assumed that in this steady state, there also exists a steady state pore pressure profile. Their model required a stress distribution as input. Based on this distribution they estimated the elastic volumetric strain, and the dilatant volumetric strain. They found that the effects of elastic volumetric change are negligible compared to the dilatant volumetric chain, for their chosen sand type (with a median grain size, D_{50}, of 210 µm, and a permeability, k, of 0.15 mm s^{-1}).

Later, Padfield (1978) and Torrey III et al. (1988), showed that breaching is a possible failure mechanism for river banks. In this case triggered by a initial shear failure, instead of a suction tube. Padfield (1978) carried out small scale experiments in a centrifugal tank, to support his claims. Later, also van den Berg et al. (2002) and van den Berg et al. (2017), proposed breaching as a mechanism for large scale failures. Their evidence suggests that the Vlierzele Sands, a 10 to 20 metres thick layer of sand found at or slightly below the land surface in large parts of northern and western Belgium, were transported there via turbidity currents created by large unstable breaching events.

van Rhee and Bezuijen (1998) carried out larger scale experiments, with heights up to 2.2 m. Like Breusers (1977), they initiate the breaching with a suction tube. They found that the wall velocity could not be predicted using the theoretical formula of Breusers (1977). They proposed two possible reasons: 1) At higher breach heights, dual mode slope failure is more likely, which could increase the total wall velocity, and 2) the formation of a large turbidity current at the lower part of the breach face, increasing the erosion of the breach face. They also measured the pore pressure inside the soil, and the concentrations and velocities of the turbidity current.

Mastbergen and Van Den Berg (2003) created a quasistatic 1D depth averaged numerical model of a turbidity current on an erodible slope. The model is derived from the momentum balance for the sand-water mixture, and mass balance for the sand and water. In this model the breach acts as source of sediment, with the size of the sediment flux source depending on the wall velocity, and the height of the breach. In this qua see static model the movement of the breach face, and its change in height, are not taken into account. They apply this model to support their theory that breaching is the driving mechanism for flushing events in the Scripps Submarine Canyon (Shepard, 1951). Using the same equations, Mastbergen (2009) created another depth averaged 1D numerical model, simulating the formation of a steady-state breach during collection of sand by suction dredging. This steady state can form for a fixed velocity of the suction dredger parallel to the breach, although the formation

of a steady state breach is not guaranteed.

A similar model was developed by Eke et al. (2011). They validated this model with laboratory experiments of a breach with an initial height of 0.7 m. Like Mastbergen and Van Den Berg (2003), they applied their model to a flushing event in a submarine canyon, the Monterey submarine canyon.

van Rhee (2002) created a 2D numerical model, for the simulation of the sedimentation process in a trailing suction dredger. The model simulated the flow of sand-water mixture up to concentrations of 30%. The interaction of the sand-water mixture with the more dense soil was done by using an immersed boundary, whose location is updated based on calculated values of sedimentation and erosion. This model was later used for modelling stable and unstable breaches (van Rhee, 2015).

Yao You carried out a series of breaching experiments (You et al., 2012; You et al., 2013; You et al., 2014), with heights of 0.3 m and 0.9 m. Instead of initiating the breach by a suction tube, they build a breach by filling a section, closed off by a movable gate, with sand. The breaching process is initiated by lifting the gate. For the breach with a height of 0.9 m they, like van Rhee and Bezuijen (1998), observe dual mode slope failure for higher breach heights. They also measured pore pressure inside the soil during their experiments.

1.3 Suction dredging breaching

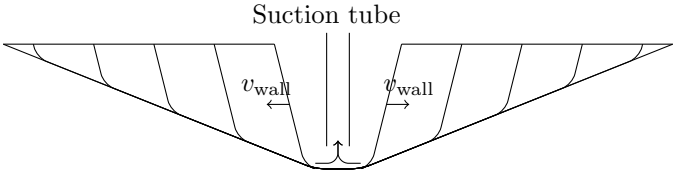

Figure 1.5: The development of a suction pit after vertically inserting a suction tube into a dense sandy soil.

Breaching is an essential process for the collection of sand by suction dredging. Suction dredging is initiated by inserting a suction tube vertically into a sand bed. This creates a suction pit, with steep walls (steeper than the internal friction angle of the sand) and thus initiates the breaching process. Due to the breaching process, these steep walls start retrogressing away from the suction tube, while the sand released forms a turbidity current which flows toward the suction tube. The suction tube can then collect sand without having

to move, making suction dredging an energy efficient way of collecting sand. The velocity at which the steep walls retrogress is known as the wall velocity, v_{wall}. This wall velocity depends on the angle of the steep walls, and the sand's density, porosity, and permeability (See Section 2.1.2 for more information). For constant sand properties, the wall velocity reduces as the wall angle becomes milder, and drops to zero when the wall angle becomes milder than the internal friction angle.

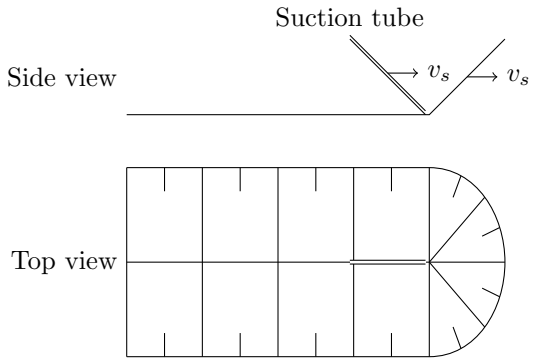

Figure 1.6: The formation of an equilibrium slope as the suction tube moves at a constant horizontal velocity.

Usually, after injecting the suction tube vertically, and creating a suction pit, the tube is moved horizontally at a fixed velocity. During this movement an equilibrium slope, relative to the moving suction tube, can form. When the eroding effect of the turbidity current formed during breaching is ignored, this equilibrium slope has a constant slope angle. This slope angle is the one at which the wall velocity is equal to the velocity of the suction tube. As the velocity of the tube increases, the equilibrium wall angle becomes steeper.

As the size of the breach increases, so does the size of the turbidity current and its contribution to the erosion of the breach face. The erosion by the turbidity current increases the retrogression velocity. Therefore, to match the velocity of the suction tube, a milder angle is required. This leads to an equilibrium slope which becomes milder further down the breach face, as the erosion by the turbidity current increases, creating a curved breach face (Figure 1.7). This equilibrium slope can be predicted using the HMBreach model of Mastbergen (2009)

To avoid damage by breaching during dredging activities, the expected slope at the end of suction dredging is estimated. Using this estimated slope,

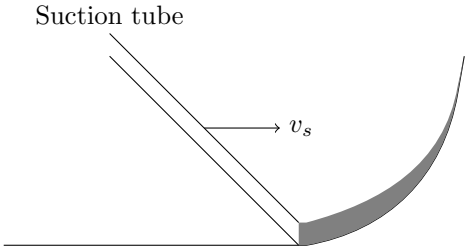

Figure 1.7: The formation of an equilibrium slope as the suction tube moves at a constant horizontal velocity, for larger breach heights. The slope of the breach wall becomes milder, as the turbidity current increases in size.

a minimum distance from the shore, and a maximum depth can be determined for dredging activities. For more coarse sands ($D_{50} > 200\,\mu m$, $D_{15} > 100\,\mu m$), these slopes can be found in tables. For finer sands, where the chance of unstable breaching is greater, it is recommended to carry out more detailed calculations with a numerical model. This is usually done by calculating the equilibrium slope with HMBreach.

HMBreach predicts equilibrium slopes during dredging with a horizontally moving suction dredger, taking into account the eroding effect of the turbidity current. It does not predict what happens after dredging activities cease. After ceasing the dredging activities, the breaching process continues until the height of the breach face is reduced to zero. For calculations it is assumed that the breach is stable, and therefore stops quickly after stopping of dredging activity. This method does not check for the formation of unstable breaches. It is also not appropriate to simulate a breach not initiated by a suction dredger (e.g. the large breaching events on the Australian coast).

To predict the stability of a breach, several methods are available. The simplest is an analytical formula derived by van Rhee (2015) (See also Section 2.5), which predicts the size of the turbidity current by multiplying the breach height with the calculated wall velocity, and combines this with an empirical formula which predicts the equilibrium slope for this turbidity current. If this equilibrium slope is milder than the slope of the profile above the breach, an unstable breach can be expected. Another method employs the HMTurb model of Mastbergen and Van Den Berg (2003), which also predict the size of the turbidity current by multiplying the breach height with the predicted wall velocity, but then models the behaviour of this current downstream of the breach, instead of using an empirical model. Finally, the 2D model of van

Rhee (2002) might be used to predict the stability of a breach, as has been done by van Rhee (2015). However, these methods are not able to incorporate the effect of sliding wedges on the breaching process, and, all methods mentioned are two dimensional, while the breaching process is a three-dimensional process (See for example the final profile in Figure 1.3).

1.4 Objectives

Current models commonly used to simulate the breaching process, and do not include all the effects of larger breach heights, and are two-dimensional. Most importantly, the formation of large slides during dual mode slope failure is not modelled by the current models, while it is believed the have a significant effect on the process. Therefore, the main research question to be answered in this thesis is:

How can we improve the prediction of the (unstable) breaching process?

To successfully answer this questions, it has been sub divided into several subquestions.

What is the effect of increasing breach height on the breaching process?

To properly predict the effects of larger breach heights, these effects must first be clear. It is believed that the large slides will form more often at larger breach heights, and the turbidity current will become stronger, possibly eroding the breach face itself and increase the total erosion velocity.

How does changing from a two-dimensional to a three-dimensional setup affect the breaching process?

Current models are all two-dimensional, and all known experiments use a limited width, and essentially model a two-dimensional process. However, as observations in the field show, three-dimensionality plays an important role in the breaching process. As the process progresses, the breach face spreads in all directions, forming a shell shaped hole. Furthermore, it is expected that erosion by the turbidity current can form gullies, which will affect the further

movement of the current.

1.5 Methods

The breaching process is often investigated using laboratory experiments (e.g. Breusers, 1977; You et al., 2012; van Rhee and Bezuijen, 1998). However, laboratory have several downsides. They are usually limited in size, with a maximum breach height of 2.2 m by van Rhee and Bezuijen (1998), because larger scale experiments are very costly.

It is also difficult to observe three dimensional effects in laboratory experiments. During experiments using a wider flume, the turbidity current obscures the view further from the sides. Complicated measurement methods are needed to follow the development of the breach face away from the sides (van Rhee and Bezuijen, 1998).

Therefore numerical simulation is used to investigate the problem. Numerical simulation is a cost effective method, and allows to easily increase in scale. It also makes observation of the process easier as data at every location can be collected easily. However, numerical simulation requires several simplifications. To make sure these simplifications do not lead to wrong results, the numerical model is validated.

Available numerical models used (e.g. van Rhee, 2015) for breaching do not include movement of the dense soil. They assume the soil the be completely static, with only particles leaving the soil at the soil-water interface at a steady rate. However, large slides during breaching are expected to have a large impact for higher breach heights, which cannot be modelled with current approaches. The requirements for the model can thus be roughly split into three parts:

- The flow of particles suspended in a liquid, to model the turbulent turbidity current, and its interaction with surrounding water.
- The dense sandy soil, where friction forces dominate over hydrodynamic forces, including the effects of pore pressure feedback. To model the slides frequently occurring during breaching, we require a model which can reproduce the transition from static to yielding soil, and the large scale deformations after this transition.
- The interaction of the turbidity current with the dense sandy soil. The pick-up of sediment from the bed, and the sedimentation of particles in the turbidity current to the bed

The starting point in this thesis will be the existing model of van Rhee (2015), which models the flow of sand-water mixtures well, as long as friction between particles plays no roles. Thus this model will be extended to include the frictional regime.

Classical soil mechanical methods use constitutive laws based on stress-strain relationships (Schofield and Wroth, 1968; Zienkiewicz et al., 1977). These methods can reproduce the transition from static two flowing soil well, but are not suitable for simulating large scale deformation During the last decade, techniques such as particle finite element (PFEM) (Oñate et al., 2011) and the material point method (Alonso et al., 2015; Ceccato, 2015; Bandara and Soga, 2015) have been developed to address this problem. These methods are able to also reproduce the large scale deformations. However, combining these models with complex turbulent flows remains a challenge.

This work considers a fluid mechanical formulation based on a stress-strain rate constitutive law based on work published by Lalli and co-workers (Lalli and Di Mascio, 1997; Lalli et al., 2005), who modelled the frictional regime as a non-Newtonian fluid with a yield stress. Cassar et al. (2005) have shown that the model, with some adaptations, also works well for submerged granular flows. Goeree (2018) has shown that this method also works for modeling a submerged granular column collapse, including pore pressure feedback. Because this method is based on stress-strain it is easily combined with the fluid dynamical model.

OpenFOAM (Open-source Field Operations And Manipulations) (Greenshields, n.d.) will be used to create the numerical model. OpenFOAM is an open-source C++ toolbox for the development of CFD (and other continuum mechanical) solvers. OpenFOAM allows users to easily extend the core program with, among others, their own solvers, boundary conditions and turbulence models. The model described in this thesis is an extension of an existing model, settlingFoam. The chapter will start with a description of settlingFoam, after which the extensions of the model are described.

For validation of the model laboratory experiments are carried out. During experiments, pore pressure inside the sand, and the movement of the sand-water interface are tracked. These experiments will be as large as feasible, because it is expected that some processes only occur for larger breach heights. These experiments also allow us to investigate:

- Breaches with slopes above the breach wall, and their effect on the stability of the breaching process.
- The angle of the slope which forms at the toe of the breach, which likely play an important role in the stability of a breaching process.

- The frequency of large slides, and their effect on the breaching process.

Besides validating with these laboratory experiments, the model will also be validated for several subprocesses important for unstable breaching:

- The flow of sand-water mixtures.
- The formation of a dense bed due to settling of sediment.
- The soil mechanical behaviour of the dense bed.
- The erosion of a dense bed by a flow.
- The formation of underpressure in the pores due to dilation.

1.6 Reading guide

This thesis starts by first investigating the breaching process and its subprocesses. In **Chapter 2** a more in depth description of different aspects of the breaching process will be given. First dilatancy, and how it relates to the breaching process. Next, the turbidity current formed during breaching, and how erosion and sedimentation due to this current affects the breaching process, is treated. Then the stability of the breaching is explained. Next, dual mode slope failure is explained. This is a combination of an interfacial process where particles are released from the breach face, and internal shear failure. Finally, the differences and similarities between breaching and liquefaction are discussed.

Next, laboratory experiments are described in **Chapter 3**. Using the knowledge gained in the previous steps a model will be developed. The governing equations, and the reasoning for choices taken, are described in **Chapter 4**. The numerical implementation of the model is described in **Chapter 5**. Next the created numerical model is validated in **Chapters 6 and 7**. **Chapter 6** validates the model using subprocesses important in unstable breaching. Next, in **Chapter 7** the model is validated using the breaching process observed in laboratory experiments. Finally, in **Chapter 8**, the results of previous the chapters are used to give conclusions and recommendations, and to answer the research questions.

Chapter 2

Breaching process description

Breaching is triggered by a slope steeper than the angle of repose, in dilative sand with sufficiently low permeability. This steep slope is called the breach face. Because a slope steeper than the internal friction angle is not stable, it will start shearing. Due to dilatancy induced lower pore pressure, this shearing is greatly reduced, and instead of a shear failure, particles are released at the breach face particle by particle, causing the breach face to slowly retrogress. The particles released form a turbidity current which transport them away from the breach. The turbidity current interacts with the downstream slope via erosion, and through sedimentation of particles from the current (Figure 2.1). A breach can be stable or unstable. A breach is considered unstable when the height of the breach face increases over time.

In this chapter a more in depth description of different aspects of the breaching process will be given. First dilatancy, and how it relates to the breaching process is discussed. Next, the turbidity current formed during breaching, and how erosion and sedimentation due to this current effects the breaching process is treated. Then breach stability is explained. Next, dual mode slope failure, which is a combination of the breaching process with shear failure, is explained. Finally, the differences and similarities between breaching and liquefaction are discussed.

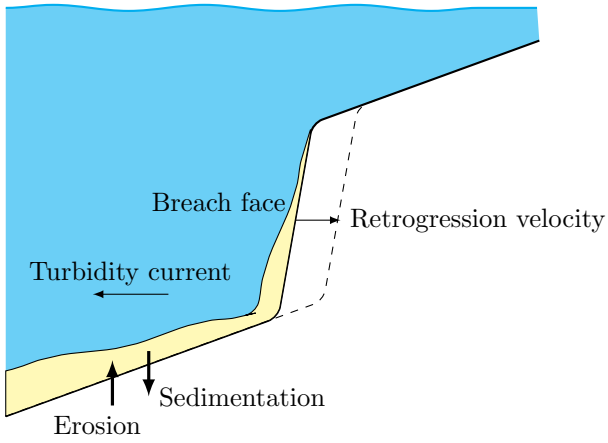

Figure 2.1: Schematization of the breaching process .

2.1 Dilatancy

Dilatancy is a vital phenomena for the breaching process. Without the negative pore pressure induced by dilatancy, breaching does not occur, and instead a simple shear failure would occur. In this section dilatancy, and how it is affected by different soil parameters, is discussed, and afterwards the link between dilatancy and breaching is shown.

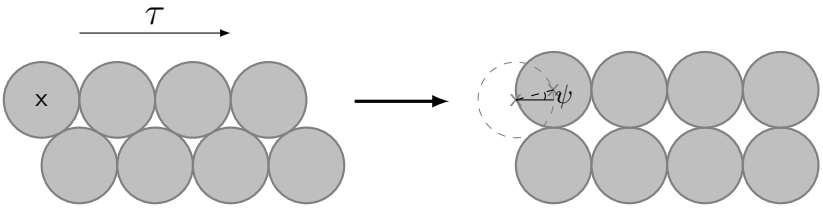

Figure 2.2: Schematization of dilatancy for idealised spherical particles . In order for the top layer to move horizontally, it has to move upwards as well, increasing the pore volume. The average angle, relative to horizontal, of the path of the top-left particle is denoted ψ, which is equal to the dilatancy angle.

Reynolds (1885) was the first to publish on the change of volume of granular materials during deformation. He coined the term dilatancy for increase of

volume during deformation. Take for example the two layers of idealised round particles in Figure 2.2. In order for the top layer to move horizontally, it has to move upwards as well, increasing its pore volume. The same effect occurs in less ideal dense sands. How sensitive sands are to dilatancy (or compaction) is often expressed using the dilatancy angle, ψ (Rowe, 1962). This angle can be interpreted as the angle of the path a particle takes, relative to the shear direction. This angle can be visualised as the contact angle of two layers of idealized particles. For the top layer to move Δx horizontally, it will move $\Delta z \tan \psi$ vertically.

Because particles are not only moved horizontally, but vertically as well, more work is required to shear the particles. Taylor (1948) proposed that the necessary work to move a particle Δx horizontally is

$$\tau \Delta x = p_{\text{eff}} \tan \phi_{\text{c}} \Delta x + p_{\text{eff}} \Delta y, \tag{2.1}$$

where τ is the shear stress , which is equal to half the difference between the maximum and minimum principle stresses,

$$\tau = \frac{1}{2} \left(\sigma_1 - \sigma_3 \right), \tag{2.2}$$

and p_{eff} is the effective pressure between sand particles, equal to the mean of the maximum and minimum effective principle stresses,

$$p_{\text{eff}} = \frac{1}{2} \left(\sigma_1' + \sigma_3' \right), \tag{2.3}$$

where σ_1' is the effective principle stress, which is the principle stress, σ_1, minus the water pressure, p_{c}, and ϕ_{c} is the internal friction angle of the sand. This leads to the following ratio between shear stress and effective pressure:

$$\frac{\tau}{p_{\text{eff}}} = \tan \phi_{\text{c}} + \frac{\Delta y}{\Delta x} = \tan \phi_{\text{c}} + \tan \psi. \tag{2.4}$$

When dilative sand is sheared, initially it compacts slightly through small rearrangements of particles. Afterwards it starts dilating (Figure 2.3b). This dilation is accompanied by an increased ratio between yield stress and effective pressure (Figure 2.3a). This ratio reduces to the internal friction angle, $\tan \phi_{\text{c}}$, as the concentration goes to the equilibrium concentration.

Wan and Guo (1999) express the dilatancy angle as a function of the total mobilized friction angle ($\tan \phi_t = \tan \psi + \tan \phi_{\text{c}}$), and an equivalent friction angle ϕ_f, which reflects the influence of sliding, rolling, and rearrangement of particles.

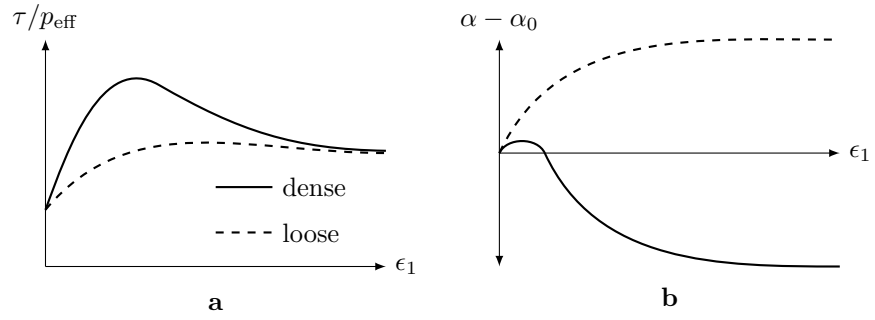

Figure 2.3: a) The ratio of shear stress, τ, and effective stress, p_{eff}, and b) the concentration, α, relative to the initial concentration, α_0, versus the principal strain, ϵ_1, for initially dense and loose sands.

$$\sin\psi = \frac{\sin\phi_t - \sin\phi_f}{1 - \sin\phi_t \sin\phi_f}. \tag{2.5}$$

According to Wan and Guo (1999), both the total mobilized and equivalent friction depend on the current, and critical void ratio. ϕ_f is

$$\sin\phi_f = \left(\frac{e}{e_{\text{cr}}}\right)^{\beta_f} \sin\phi_{\text{c}} \tag{2.6a}$$

$$\sin\phi_t = \frac{\epsilon_s}{a + \epsilon_s} \left(\frac{e}{e_{\text{cr}}}\right)^{-\beta_t} \sin\phi_{\text{c}}, \tag{2.6b}$$

where β_f and β_t are parameters which depend on the type of sand. For different sand types, Wan and Guo (1999) found values between 0.3 and 1.5 for β_f, while for β_t they assume a value of 1.3. ϵ_s is the total shear deformation, and the term $\epsilon_s/(a + \epsilon_s)$ takes the initial compression into account. The void ratio, e, is the total pore volume divided by the total grain volume, and is related to the concentration α_{d} as

$$e = \frac{1 - \alpha_{\text{d}}}{\alpha_{\text{d}}}. \tag{2.7}$$

Ignoring the initial compression, ψ can be defined as

$$\sin\psi = \frac{\left(\left(\frac{e}{e_{\mathrm{cr}}}\right)^{-\beta_t} - \left(\frac{e}{e_{\mathrm{cr}}}\right)^{\beta_f}\right)\sin\phi_{\mathrm{c}}}{1 - \left(\frac{e}{e_{\mathrm{cr}}}\right)^{\beta_f-\beta_t}\sin\phi_{\mathrm{c}}}, \tag{2.8}$$

where ψ is positive for dense sands, where $e < e_{\mathrm{cr}}$, and negative for loose sands, where $e > e_{\mathrm{cr}}$.

The critical void ratio, e_{cr}, is the void ratio where neither dilation or compaction occurs. According to Verdugo and Ishihara (1996), e_{cr} depends on the confining pressure as follows

$$e_{\mathrm{cr}} = e_{\mathrm{cr0}}\exp\left(-\frac{p_{\mathrm{eff}}}{h_{\mathrm{cr}}}\right), \tag{2.9}$$

where e_{cr0} is the critical void ratio without confining pressure, and h_{cr} is a material constant, and is usually in the order of 10 MPa (Been et al., 1991; Verdugo and Ishihara, 1996), which means that for pressures of 100 kPa and lower the critical void ratio changes only about 1%.

Boyer et al. (2011) show that this critical concentration, α_{eq}, depends on the shear rate, $\dot{\gamma}$, relative to the effective granular pressure, p_{eff}. From experiments in a shear cell they retrieve

$$\alpha_{\mathrm{eq}} = \frac{\alpha_{\mathrm{eq;0}}}{1+\sqrt{I_v}}, \tag{2.10}$$

where $\alpha_{\mathrm{eq;0}}$ is the equilibrium concentration for zero shear, and I_v is the viscous number, which is the shear rate made dimensionless

$$I_v = \frac{\mu_{\mathrm{c}}\dot{\gamma}}{p_{\mathrm{eff}}}, \tag{2.11}$$

Here μ_{c} is the dynamic viscosity of water in Pa s, $\dot{\gamma}$ is the second invariant of the deformation tensor, $\underline{\underline{\boldsymbol{\gamma}}}$, and, using the Einstein summation convention, is defined as follows:

$$\dot{\gamma} = \sqrt{0.5\gamma_{ij}\gamma_{ij}}, \tag{2.12}$$

and

$$\underline{\underline{\boldsymbol{\gamma}}} = \gamma_{ij} = \frac{\partial u_i}{\partial x_j} + \frac{\partial u_j}{\partial x_i}, \tag{2.13}$$

where u_i is the particle velocity in the i-direction.

Roux and Radjaï (2002) suggest the linearization for the dilatancy angle around the critical concentration:

$$\psi = C_{\mathrm{dil}} \left(\alpha_d - \alpha_{\mathrm{eq}} \right). \tag{2.14}$$

Pailha and Pouliquen (2009) instead use

$$\tan \psi = C_{\mathrm{dil}} \left(\alpha_d - \alpha_{\mathrm{eq}} \right), \tag{2.15}$$

where C_{dil} is a material constant. For $\alpha_{\mathrm{eq}} = \alpha_{\mathrm{eq};0}$, this constant can be related to Equation (2.8) via

$$C_{\mathrm{dil}} = \frac{\sin\left(\phi_{\mathrm{c}}\right)}{1 - \sin\left(\phi_{\mathrm{c}}\right)} \left(- \left(\beta_f + \beta_t\right) \frac{-1}{\alpha_{\mathrm{eq};0} - \alpha_{\mathrm{eq};0}^2} \right). \tag{2.16}$$

For typical values, C_{dil}, is in the order of 10.

2.1.1 Dilatancy effects in slope stability

In dilative sands, this shearing is accompanied by an increase in pore volume. Because water is almost incompressible, this increase in pore volume is accompanied by an inflow of water through the pore skeleton. This flow is driven by a negative pore pressure, creating a pressure gradient. The velocity of this inflow depends on the gradient of the pore pressure, and the permeability of the sand. For low velocities, the inflow can be calculated with Darcy's law (Darcy, 1856):

$$q_f = -\frac{k}{\rho_c g} \nabla p_e, \tag{2.17}$$

where q_f is the volumetric flux of pore water per unit area in $\mathrm{m\,s^{-1}}$, p_e is the excess pore water pressure in Pa, relative to hydrostatic pressure, and k is the hydraulic permeability in $\mathrm{m\,s^{-1}}$.

van Rhee and Bezuijen (1992) investigated the underpressure gradient required to keep a slope, steeper than the angle of repose, stable. They derived balance equations on two scales. They looked at the momentum balance on micro scale, for a single spherical particle (Figure 2.4b), and at the force balance at the larger scale, for a continuum (Figure 2.4a) They found that the minimum pore pressure gradient, perpendicular to the surface, to keep a slope with angle β stable is:

$$\nabla_{\perp} p_e = -f_s \frac{\rho_{\mathrm{d}} - \rho_{\mathrm{c}}}{\rho_{\mathrm{c}}} \frac{\sin\left(\phi_{\mathrm{c}} - \beta\right)}{\sin \phi_{\mathrm{c}}}, \tag{2.18}$$

Figure 2.4: The force and momentum balance of respectively a) a continuum, and b) a single particle, where F_g is the gravity force, F_i is the force due to inflow of water, F_f is the friction force, and N is the normal reaction force (Redrawn from van Rhee and Bezuijen (1992)).

where ϕ_c is the internal friction angle, ρ_d is density of the particles in $\mathrm{kg\,m^{-3}}$, and f_s is a factor depending on which force balance is used to derive the formula. For the single particle mode, f_s is equal to $\frac{4}{3}$, while with the continuum mode a value of $(1-n)$ is found, where n is the porosity.

Equation (2.18) was compared with laboratory experiments. In these experiments, they applied a pressure gradient over a 0.1 m thick soil sample, and then rotated the until failure. They found that for an inward flow the single particle mode gave the best prediction of stability (i.e. $f_s = \frac{4}{3}$), while for outward flow, the continuum mode gave the best prediction (1.e $f_s = (1-n)$) (See Figure 2.5).

However, there are several uncertainties involved in deriving the necessary force using the single particle mode. The force due to inflow of water, F_i, assumes that the pressure gradient caused by the inflow acts only on half of the particle. It is unknown if this is the case. Furthermore, this mode assumes a fixed position of the contact point between two particles, but it is doubtful that this angle remains constant for every particle. Therefore, the continuum approach is considered more correct. Although it does not take into account the configuration of individual particles, its results can be considered an upper boundary for necessary pore pressure.

2.1.2 Wall velocity

The results can be used to estimate the retrogression velocity of the breach face (Figure 2.1), called the wall velocity.

It is assumed that the dilation rate, which controls the inflow of water, is such that the generated pore pressure is enough to keep the slope just

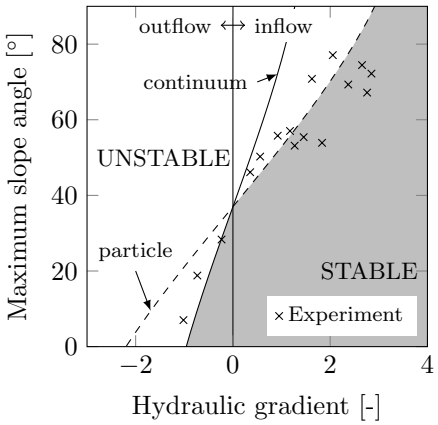

Figure 2.5: Relation between maximum slope angle and hydraulic gradient measured (Redrawn from van Rhee and Bezuijen (1992)

stable. This is a sensible assumption, as at this point there is a force balance, thus there is no extra forcing to induce more shearing and more dilation. Therefore, the pore pressure gradient can be estimated with Equation (2.18). This equation can be combined with Darcy's law (Equation (2.17)) to estimate the inflow of water:

$$q_f = \frac{k}{\rho_c g} f_s \frac{\rho_d - \rho_c}{\rho_c} \frac{\sin(\phi_c - \beta)}{\sin \phi_c}. \tag{2.19}$$

It is assumed that after an increase in porosity from the initial, n_0, to a new porosity, n_1, the sand is released into the turbidity current, due to a decrease in the possible dilation, and an increase in permeability. Then, assuming the soil only expands in the horizontal direction, the change in volume required to erode a cube with sides of Δx_0, soil volume, V_0, and total volume $V_{total,0}$, is

$$V_{\text{soil}} = (1 - n_0)\Delta x_0^3 = (1 - n_1)\Delta x_1 \Delta x_0^2 \tag{2.20}$$

$$\Delta x_1 = \frac{1 - n_0}{1 - n_1} \Delta x_0 \tag{2.21}$$

$$V_{\text{total},0} = \Delta x_0^3 \tag{2.22}$$

$$V_{\text{total},1} = \Delta x_0^2 \Delta x_1 = \Delta x_0^3 \frac{1 - n_0}{1 - n_1} \tag{2.23}$$

$$\Delta V = V_{\text{total},1} - V_{\text{total},0} = \Delta x_0^3 \left(\frac{1 - n_0}{1 - n_1} - 1\right) = \Delta x_0^3 \frac{n_1 - n_0}{1 - n_1}, \tag{2.24}$$

where the subscript 0 indicates the initial state, and 1 the state just before failure, And ΔV is the change in total volume. By combining this with Equation (2.19), the horizontal velocity of the erosion front, v_{wall}, also known as the wall velocity, is found:

$$\Delta V = q_f \Delta x_0^2 \Delta t \tag{2.25}$$

$$\frac{\Delta x_0^3}{\Delta t} \frac{n_1 - n_0}{1 - n_1} = q_f \Delta x_0^2 \tag{2.26}$$

$$\frac{\Delta x_0}{\Delta t} \frac{n_1 - n_0}{1 - n_1} = q_f = \frac{k}{\rho_c \underline{\boldsymbol{g}}} f_s \frac{\rho_d - \rho_c}{\rho_c} \frac{\sin(\phi_c - \beta)}{\sin \phi_c} \tag{2.27}$$

$$v_{\text{wall}} = \frac{1 - n_1}{n_1 - n_0} \frac{k}{\rho_c |\underline{\boldsymbol{g}}|} f_s \frac{\rho_d - \rho_c}{\rho_c} \frac{\sin(\phi_c - \beta)}{\sin \phi_c}, \tag{2.28}$$

where Δt is the time increment, and $\underline{\boldsymbol{g}}$ is the gravitational accelleration.

2.2 Turbidity current

As the erosion front retrogresses backwards, the sand particles are released and flow downstream as turbidity current (Figure 2.1). The interaction of this current, through erosion and sedimentation, with the slope downstream of the breach face, as well as the breach face itself, play an important role in the behaviour of the breaching process.

The characteristics of this flow of sand-water mixtures, depend mostly on the Reynolds number (Mastbergen et al., 1988). The Reynolds Number, *Re*, is the ratio of turbulent shear stresses over viscous shear stresses. The Reynolds number increases as the particle flux increases.

For low fluxes, and thus low *Re*, the turbulent eddies are not strong enough to keep sand particles in suspension. In this case the sand grains are transported by rolling over the bed. The grains come to a stop at a slope angle close to the internal friction angle.

As the flux increases, and thus the Reynolds number, turbulent eddies increase in strength. Mixing by turbulent eddies can balance the downward particle flux by sedimentation. This way sand particles can stay in suspension, and the sand-water mixture is transported downstream as a turbidity current. Turbidity currents are particle-laden flows driven by gravity, in which particles are suspended by turbulent eddies. A Turbidity current can interact with the sand bed over which it flows. Particles from the mixture can sediment onto the bed, or particles can be eroded from the bed by the turbidity current. A turbidity current can also entrain ambient fluid.

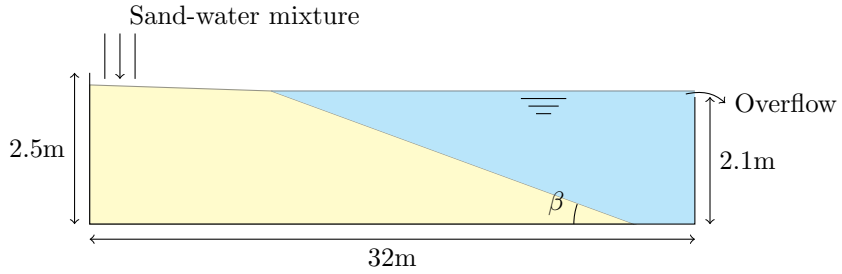

Figure 2.6: The experimental setup used by Mastbergen et al. (1988).

Mastbergen et al. (1988) created a sand fill dam in a 32 m × 2.5 m × 0.5 m flume, and measured the resulting underwater slope, β, during construction of this dam (Figure 6.22). For flows with a low production rate (s <10 kg s^{-1} m^{-1}) grain flows were observed, with intermittent flow slides. Slope angles increased during grain flows, while after a flow slide much milder slopes were observed. Because of this the average slope varied a lot in time. For higher production rates (s >10 kg m^{-1} s^{-1}) turbidity currents were observed. Flow slides occur a lot less for this kind of flow, after some time the slope reaches an equilibrium, β_{eq}, after which the slope barely changes.

Using the Engelund-Hansen formula Mastbergen et al. (1988) derived for the equilibrium slope, β_{eq},

$$\tan \beta_{\mathrm{eq}} = \frac{D_{50}^{0.6}(1-\alpha_{\mathrm{d}})^{1.2}(1+\Delta\alpha_{\mathrm{d}})}{s^{0.4}}, \tag{2.29}$$

where D_{50} is the median grain diameter, c is the sand volume concentration of the turbidity current, and s is the sand production rate.

For concentrations lower than about 0.35 the slope is mostly influenced by the grain diameter, D, and the sand production rate, s, when using this formula. A larger grain diameter leads to a steeper slope, and a larger sand production rate leads to a milder slope. A simpler, empirically derived formula which excludes the influence of concentration is given in van Rhee (2015):

$$\tan \beta_{\mathrm{eq}} = \frac{1623 D_{50}^{0.92}}{s^{0.39}}. \tag{2.30}$$

2.3 Sedimentation

Sand particles inside the turbidity current can settle and be deposited on the bed over which it flows, this is called sedimentation (Figure 2.1). The speed at which sedimentation occurs (and whether sedimentation occurs at all) depend on the vertical velocity of the sand particles in the current. The variety of factors influencing this velocity are discussed in this and the next section.

Using the second law of Newton, the settling velocity of a single particle in a fluid with hydrostatic pressure can be modelled as (Murray, 1970):

$$\rho_{\mathrm{d}} \frac{\mathrm{d}w_{\mathrm{d}}}{\mathrm{d}t} = \frac{F_{\mathrm{D}}}{V_p} + (\rho_{\mathrm{d}} - \rho_{\mathrm{c}}) \, |\underline{\boldsymbol{g}}| - C_m \rho_{\mathrm{c}} \frac{\mathrm{d}w_{\mathrm{d}}}{\mathrm{d}t} + \rho_{\mathrm{c}} \frac{\mathrm{d}w_{\mathrm{c}}}{\mathrm{d}t}, \tag{2.31}$$

where w_{d} and w_{c} are the vertical velocities of the particle and the fluid respectively, C_m is the added mass coefficient, V_p is the volume of the particle, which is

$$V_p = \frac{1}{6} f_{\mathrm{shape}} \pi D^3, \tag{2.32}$$

where f_{shape} is the shape factor, which takes into account the deviation of the particle from the idealized spherical particle. F_{D} is the drag force

$$F_{\mathrm{D}} = C_{\mathrm{D}} \frac{1}{8} \pi D^2 \rho_{\mathrm{c}} w_r |w_r|, \tag{2.33}$$

where C_{D} is the drag coefficient, and w_r is the vertical particle velocity relative to the water velocity, $w_{\mathrm{d}} - w_{\mathrm{c}}$.

In a stagnant fluid ($w_{\mathrm{c}} = 0$) the terminal settling velocity, w_{d}^{∞} (when $\mathrm{d}w_{\mathrm{d}}/\mathrm{d}t = 0$) can be derived using Equation (2.31):

$$w_{\mathrm{d}}^{\infty} = \sqrt{\frac{4\psi g \Delta D}{3 C_{\mathrm{D}}}}. \tag{2.34}$$

For laminar flow ($Re_p^{\infty} < 1$), the drag coefficient, C_{D}, for perfect spheres is known exactly

$$C_{\mathrm{D}} = \frac{24}{Re_p^{\infty}}, \tag{2.35}$$

where the Reynolds particle number, Re_p^{∞}, is

$$Re_p^{\infty} = \frac{w_{\mathrm{d}}^{\infty} D}{\nu}, \tag{2.36}$$

where ν is the kinematic viscosity of the liquid.

As the particle Reynolds number increases, turbulence becomes more important. For Reynolds particle numbers smaller than 1×10^6, the drag coefficient can be estimated with the formula of Turton and Levenspiel (1986) (Figure 2.7):

$$C_{\mathrm{D}} = \frac{24}{Re_p^{\infty}} \left(1 + 0.173(Re_p^{\infty})^{0.657}\right) + \frac{0.413}{1 + 16300(Re_p^{\infty})^{-1.09}}. \tag{2.37}$$

Adjustments for non-spherical particle are available, see e.g. Hölzer and Sommerfeld (2008).

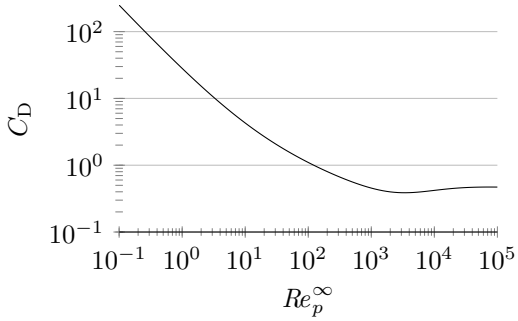

Figure 2.7: The drag constant, C_{D}, as function of the Reynolds particle number, Re_p^{∞}

When more than one particles settles, settling velocity is reduced by interaction between particles, and an upward flux of water to compensate for the downward flux of particles. Currently, the most popular method to account for these effects is the semi-empirical formula of Richardson and Zaki (1954),

$$w_{\mathrm{d}}^{\infty} = (1 - \alpha_{\mathrm{d}})^n w_{\mathrm{d0}}^{\infty}, \tag{2.38}$$

where w_{d0} is the settling velocity for particles at a concentration of 0.

For the exponent, n, Richardson and Zaki (1954) give, when ignoring wall effects,

$$n = \begin{cases} 4.65 & Re_p^{\infty} \leq 0.2 \\ 4.35 Re_p^{\infty -0.03} & 0.2 < Re_p^{\infty} \leq 1 \\ 4.45 Re_p^{\infty -0.1} & 1 < Re_p^{\infty} \leq 500 \\ 2.39 & Re_p^{\infty} > 500 \end{cases} \tag{2.39}$$

Garside and Al-Dibouni (1977) gave an empirical formula based on a large set of data (including that of Richardson and Zaki (1954)), with Re_p ranging

from 0.0011 to 3500:

$$n = \frac{5.1 + 0.27 Re_p^{\infty 0.9}}{1 + 0.1 Re_p^{\infty 0.9}}. \tag{2.40}$$

In their data set they find an average deviation, of the observed fall velocity from the estimated fall velocity, of 9.8%. This uncertainty increases as the concentration of particles increases.

Previous formulae are valid for particles in a quiescent fluid. In the turbulent turbidity current, settling velocities can differ. Due to the non-linear dependence on the relative velocity of the drag force (Equation (2.33)), the average settling velocity is reduced by turbulent fluctuations (Murray, 1970). Turbulence also influences the settling velocity by affecting the drag coefficient (Crowe et al., 2011). Particle settling velocities can also increase in turbulence due to trajectory biasing. This is when particles are swept toward the downflow side of vortices (Mei, 1994). Experiments with particles similar to those encountered during breaching ($D_{50} = 210\,\mu$m and relative density of 2.65) by Kawanisi and Shiozaki (2008), show a reduction in settling velocity up to 40% as turbulent intensity increases.

2.4 Erosion

If the current is strong enough it can move sand particles via a combination of drag and lift forces. Erosion (Figure 2.1) is the net effect of combined settling and pick-up of particles, when the pick-up flux of particles is larger than the flux of settling particles During breaching, the turbidity current can erode particles both downstream of the breach face, as well as from the breach face itself. This section discusses several factors influencing the quantity of erosion.

Shields (1936) was one of the first to experimentally determine the necessary forcing to initiate the motion of sand particles. Based on a limited number of experiments, he presented a graph which shows the dimensionless shear stress, θ, at which motion of sand particles is initiated for varying boundary Reynolds numbers, Re_τ. Where,

$$\theta = \frac{\tau_\mathrm{b}}{(\rho_\mathrm{d} - \rho_\mathrm{c})\, D} \tag{2.41}$$

$$Re_\tau = \frac{u_* D}{\nu_\mathrm{c}}, \tag{2.42}$$

where τ_b is the bed shear stress, ν_c, is the kinematic viscosity of the fluid, and u_* is the friction velocity, which is equal to

$$u_* = \sqrt{\frac{\tau_\mathrm{b}}{\rho_\mathrm{c}}}. \tag{2.43}$$

The critical Shields parameter, θ_cr, denotes the Shields parameter at which initiation of motion of the particles takes place. The definition of initiation of motion is contentious, with different researchers using different definitions. Many researchers use qualitative visual descriptions as negligible, small, or critical transport (Vanoni, 1975), or 'occasional particle movement at some locations', and 'frequent particle movement at all locations' (Delft Hydraulics, 1972). Instead, Graf and Pazis (1977) defined incipient motion by the number of particles entrained per square meter, and found a correspondence with the Shields curve between 100, and 1000, particles entrained per square meter.

The original Shields diagram plotted the critical Shields parameter against the Boundary Reynolds number. Because both depend on the bed shear stress, iteration is needed to determine the critical Shields parameter. The Shields curve has been adapted, among others by van Rijn (1984), who plots the critical Shields number against the Dimensionless grain diameter D_*.

$$D_* = \left[\frac{Re_\tau^2}{\theta}\right]^{1/3} = D_{50}\left[\frac{(\rho_\mathrm{d} - \rho_\mathrm{c})\, g}{\rho_\mathrm{c}\nu^2}\right]^{1/3}. \tag{2.44}$$

The Shields curve can be approximated by the formula of Soulsby and Whitehouse (1997):

$$\theta_\mathrm{cr} = \frac{0.24}{D_*} + 0.055\left(1 - \mathrm{e}^{-0.022D_*}\right). \tag{2.45}$$

Later, Paphitis (2001), combined data from 29 different sources to create an updated shields curve. Besides the average critical Shields parameter, they also provided upper and lower limits.

$$\theta_\mathrm{cr;avg} = \frac{0.273}{1 + 1.2D_*} + 0.046\left(1 - 0.57\mathrm{e}^{-0.02D_*}\right) \tag{2.46}$$

$$\theta_\mathrm{cr;max} = \frac{0.380}{1 + 1.2D_*} + 0.07\left(1 - 0.57\mathrm{e}^{-0.02D_*}\right) \tag{2.47}$$

$$\theta_\mathrm{cr;min} = \frac{0.165}{1 + 1.2D_*} + 0.03\left(1 - 0.57\mathrm{e}^{-0.02D_*}\right). \tag{2.48}$$

The D_* in the data used ranges from 0.1 to 3000. For typical breaching events, the D_* is usually between 1 to 10. The biggest difference with the original curve of Shields (1936) is for small particles, with a $D_* < 1$ (Figure 2.8).

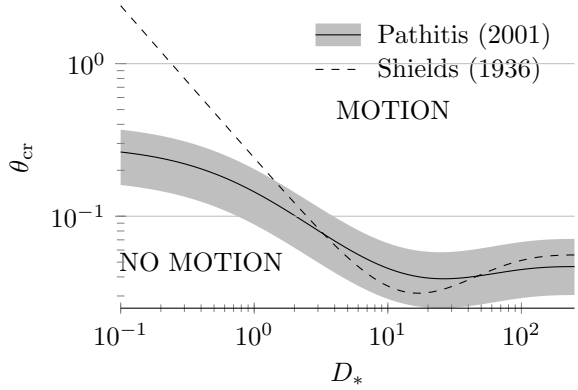

Figure 2.8: The relation between critical Shields parameter and dimensionless grain size as given by Shields (1936) and Paphitis (2001)

Once motion of particles is initiated, transport can occur as bed-load or as suspended load. Bed-load is the transport of particles by sliding or rolling over the bed, while suspended load is the transport of particles suspended in the fluid.

Several researchers presented empirical formulas for the pick-up flux of particles from the bed, into suspension, based on the difference between the critical and actual shields parameter. Based on experiments, with grain sizes ranging from 130 µm and 1500 µm, van Rijn (1984) presented the following empirical formula for the pick-up flux E,

$$E = 0.00033 D_*^{0.3} T^{1.5} \rho_d \sqrt{\Delta g D_{50}}, \tag{2.49}$$

where T is the transport parameter,

$$T = \frac{\theta - \theta_{cr}}{\theta_{cr}}, \tag{2.50}$$

Δ is the relative grain density

$$\frac{\rho_d - \rho_c}{\rho_c}, \tag{2.51}$$

and D_{50} is the median grain diameter.

The pick-up flux, E, is the weight of particles pick-up per square meter of the bed:

$$E = v_e \rho_{\mathrm{d}} \left(1 - n_0\right), \tag{2.52}$$

where v_e is the downward velocity of the bed. Alternative formulae have been developed by Nakagawa and Tsujimoto (1980) and Fernandez Luque and Van Beek (1976).

2.4.1 Retarded Erosion (Dilatancy)

Bisschop et al. (2010) and van Rhee (2010) carried out research on the erosion of granular material at high flow velocities. At high flow velocities standard sediment pick-up formulae (e.g. van Rijn (1984)) overestimate the actual pick-up. According to van Rhee (2010) this is because of under pressures caused by dilatancy. Just as during breaching, soil cannot erode before being loosened enough. The larger the pick-up flux, the quicker the expansion of soil, and thus the larger the inflow of water. From Equation (2.17) it then follows that a larger pick-up leads to a larger negative pore pressure, while for a small pick-up flux this effect is negligible.

van Rhee (2010) adds a shear force, F_s, perpendicular to the soil, generated by water flow to the force balance of Figure 2.4a. The force balance parallel to the soil at equilibrium is then

$$F_s + F_g \sin\beta = F_f = \left(F_g \cos\beta + F_i\right) \tan\phi_{\mathrm{c}}, \tag{2.53}$$

or

$$\frac{F_s}{F_g} = \tan\phi \left(\frac{\sin\left(\phi - \beta\right)}{\sin\phi} + \frac{F_i}{F_g} \right). \tag{2.54}$$

The left hand side is proportional to the dimensionless shear stress, θ, while the right hand side is proportional to dimensionless shear stress necessary for incipient motion, θ_{cr}. For a flat bed with no inflow of water, the right hand side is equal to $\tan\phi_{\mathrm{c}}$. With a slope or inflow of water, this term is multiplied with a factor $(\frac{\sin(\phi_{\mathrm{c}}-\beta)}{\sin\phi_{\mathrm{c}}} + \frac{F_i}{F_g})$. van Rhee (2010) argues that, therefore, the critical shields value can also be multiplied by this factor:

$$\theta^*_{\mathrm{cr}} = \theta_{\mathrm{cr}} \left(\frac{\sin\left(\phi_{\mathrm{c}} - \beta\right)}{\sin\phi_{\mathrm{c}}} + \frac{F_i}{F_g} \right), \tag{2.55}$$

where θ^*_{cr} is the adapted critical shields parameter.

When the excess pore pressure gradient is known, the ratio between the gravity and inflow force can be calculated with

$$\frac{F_i}{F_g} = \frac{\nabla p_e \cdot \underline{\boldsymbol{n}}}{(1-n_0)(\rho_\mathrm{d}-\rho_\mathrm{c})|\underline{\boldsymbol{g}}|}, \tag{2.56}$$

where $\underline{\boldsymbol{n}}$ is the unit vector perpendicular to the bed. The pore pressure gradient is not always known a priori. Assuming that soil has to dilate from the initial porosity, n_0, to a porosity of n_1, before it can be lifted from the bed, the necessary inflow of water can be determined, and via Darcy's equation also the pore pressure gradient.

$$q_f = \frac{n_1-n_0}{1-n_1}v_e = \frac{k}{\rho_\mathrm{c}|\underline{\boldsymbol{g}}|}\nabla p_e \cdot \underline{\boldsymbol{n}}. \tag{2.57}$$

The relative force due to inflow of water is

$$\frac{F_i}{F_g} = \frac{n_1-n_0}{1-n_1}\frac{v_e}{k(1-n_0)\Delta}. \tag{2.58}$$

van Rhee (2010) adapts the pickup formula of van Rijn (1984) (Equation (2.49)), to include these effects. van Rhee (2010) replaces the transport stage parameter, T, with T_*, using the adapted critical Shields parameter, θ^*_{cr}, defined in Equation (2.55)

$$E = 0.00033 D_*^{0.3} T_*^{1.5} \rho_\mathrm{d}\sqrt{\Delta g D_{50}}, \tag{2.59}$$

where

$$T_* = \frac{\theta-\theta^*_{\mathrm{cr}}}{\theta^*_{\mathrm{cr}}}. \tag{2.60}$$

Combining equations Equations (2.52), (2.55), (2.58) and (2.59) gives

$$v_e = 0.00033 D_*^{0.3}\left[\frac{\theta}{\theta_{cr}}\left(\frac{\sin(\phi_\mathrm{c}-\beta)}{\sin\phi_\mathrm{c}}+\frac{v_e}{(1-n_0)k\Delta}\frac{n_1-n_0}{1-n_1}\right)^{-1}-1\right]\frac{\sqrt{\Delta g D_{50}}}{1-n_0}. \tag{2.61}$$

This formula cannot be solved analytically, but has to be solved iteratively. If $\theta < \theta^*_{cr}$ for $v_e = 0$ there is no erosion. If the slope, β, is steeper than the internal friction angle, ϕ_c, a negative θ^*_{cr} is calculated, so there must be an erosion velocity to make sure $\theta^*_{cr} > 0$.

In the case of breaching the slope fails without an external force acting on it. This means $\theta^*_{cr} = 0$. Applying this in Equation (2.55) gives the following formula for the erosion velocity.

$$v_e = (1 - n_0)\, k\Delta \frac{1 - n_1}{n_1 - n_0} \frac{\sin(\phi_c - \beta)}{\sin \phi_c}, \tag{2.62}$$

which is equal to the wall velocity formula derived with the continuum approach (Equation (2.28)).

For high erosion velocities where $v_e/k >> \sin(\phi_c - \beta)$, Bisschop et al. (2010) give the following formula which can be solved directly

$$v_e^5 = \left(0.00033 D_*^{0.3} \frac{\sqrt{\Delta g D_{50}}}{1 - n_0}\right)^2 T^3 \left(k\Delta (1 - n_0) \frac{1 - n_1}{n_1 - n_0}\right)^3. \tag{2.63}$$

2.4.2 Restricted erosion (concentration)

During experiments with highly concentrated sand-water mixtures over erodible beds Winterwerp et al. (1992) found that erosion rate was limited by the sand concentration in the mixture flowing over the bed. They give a maximum possible pick-up flux based on the concentration near the bed, c_b,

$$E_{\max} = 0.033 \frac{1 - n_0 - c_b}{c_b}. \tag{2.64}$$

Rhee and Talmon (2010) also investigated the effect of high near bed sand concentrations on erosion and sedimentation of the bed. They found an effect on the net sediment pick-up rate. They assume that sediment pick-up is mostly done by turbulent eddies. These turbulent eddies pickup particles from the bed, where the concentration is $(1-n_0)$. The volume of the picked up sediment is replaced by the sand-water mixture near the bed, with a concentration of c_b. The effect is taken into account by Rhee and Talmon (2010) by applying a reduction factor, E_h, to the pick-up flux.

$$E_h = \frac{(1 - n_0) - c_b}{1 - n_0} E. \tag{2.65}$$

This formula matches well with the data of Van Rhee (2002).

Bisschop (2018) proposes another formula to determine the reduction factor.

$$E_h = E \left(\frac{n_0 - c_b}{n_0}\right)_h^n, \tag{2.66}$$

where n_h is an empirical factor. This formula matches well with the data of Winterwerp et al. (1992), for $n_h = 1.38$.

2.5 Breach stability

The stability of a breach (Figure 1.2), whether the height of the breach face decreases (stable) or increases (unstable), is important. When breaches become unstable they can go on for a long time, eroding large quantities of sand. van Rhee (2015) proposes a stability limit for breaches, based on the slopes on top (β_{top} in Figure 2.9) and at the toe of the breach face (β_{toe} in Figure 2.9). He assumed that the change in wall height is controlled by the difference between these two slopes. When β_{toe} is milder than β_{top}, an increase of the wall height, and thus an unstable breach, is expected, and vice versa.

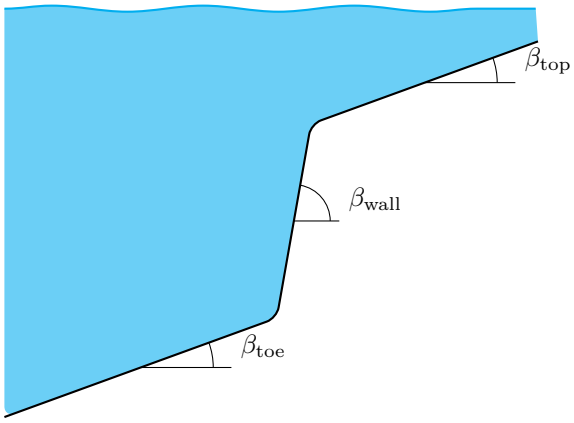

Figure 2.9: Definitions of relevant angles .

β_{top} is determined by the pre-existing geometry, while β_{toe} will depend mostly on the interaction between the formed turbidity current and the existing downstream slope. To estimate β_{toe}, van Rhee (2015) uses a simplified version of a formula empirically derived by Mastbergen et al. (1988) (Equation (2.30). In this equation, β_{toe} depends on de grain size, and the sand production rate. During breaching, the sand production rate is equal to the wall velocity, v_{wall}, multiplied by the wall height, H_{wall}, density ρ_d, and concentration, $(1 - n_0)$.

$$s = v_{\text{wall}} H_{\text{wall}} \rho_d \, (1 - n_0) \tag{2.67}$$

van Rhee (2015) then combines this with Equations (2.28) and (2.30), giving:

$$\tan\beta_{\text{eq}} = 1623D^{0.92}\left(H_{\text{wall}}\frac{k\rho_d}{\Delta n}\frac{\rho_d-\rho_c}{\rho_c}\left(1-n_0\right)^2\cot\phi_{\text{c}}\right)^{-0.39} \tag{2.68}$$

where β_{eq} is the equilibrium slope angle. van Rhee (2015) assumes that β_{top} is equal to α_{eq}. Thus a breach will be unstable if β_{eq} is milder than β_{top}. A critical wall height, above which the breach will be unstable can be determined:

$$H_{\text{wall}} > \frac{17\times10^7 D^{2.36}\left(n_1-n_0\right)\rho_{\text{c}}|\underline{\boldsymbol{g}}|\rho_{\text{c}}\sin\phi_{\text{c}}}{\left(1-n_1\right)kf_s\left(\rho_{\text{d}}-\rho_{\text{c}}\right)\sin\left(\phi_{\text{c}}-\beta\right)\rho_d\left(1-n_0\right)\tan\left(\beta_{\text{top}}\right)^{2.56}} \tag{2.69}$$

Perhaps it is more informative to look at the expected change in wall height, instead of just stable or unstable. If the angle at the toe, β_{toe}, is equal to β_{eq}, and the bottom of the breach wall moves along a line with the same angle as β_{toe}, the change in wall height is:

$$\frac{\mathrm{d}H_{\text{wall}}}{\mathrm{d}x} = \tan\beta_{\text{top}} - \tan\beta_{\text{eq}} \tag{2.70}$$

2.6 Dual mode slope failure

van Rhee and Bezuijen (1998) carried out larger scale experiments, with heights up to 2.2 m. They found that Equation (2.28) was not valid at these larger scales. They noted two reasons: first, the formation of a large turbidity current at the lower part of the breach face, increasing the erosion rate. Second, besides pure breaching, where particles are released one by one at the breach face, lumps of sand failing instead of single sand particles at the breach face are also observed (Figure 2.10). You et al. (2014) call this combination of pure breaching and sliding wedges dual mode slope failure, which they differentiates from pure breaching where no slides occur. In their experiments they observe a difference in erosion speed for pure breaching and sliding wedges. For pure breaching the breach wall retrogresses at $2.5\,\text{mm}\,\text{s}^{-1}$, while during slides is retrogresses at $21\,\text{mm}\,\text{s}^{-1}$. The slides are accompanied by a drop in excess pore pressure. The size of the drop is correlated to the size of the slide.

You et al. (2014) argue that these slides occur when the negative pore pressure generated inside the soil is insufficient to avoid shear failure. If the steady state pore pressure, at constant height and wall velocity, cannot keep the breach stable, slides are expected. These slides decrease the excess pore pressure in the soil, after which they start increasing toward the steady state

until the next slide. According to them the susceptibility to slides depends on the internal friction angle, ϕ_c, and the dilation potential. They define the dilation potential, β_{dil}, as

$$\beta_{dil} = 0.5 + \frac{m_q}{2m_u}, \tag{2.71}$$

where m_u, controls the change in volume, e, due to elastic compression.m_q controls the change in volume due to dilation due to shear.

$$e = e_{dil} + e_{el} = m_u \Delta p' + m_q \Delta q, \tag{2.72}$$

where $\Delta p'$ is the change in mean effective stress, and Δq the change in differential stress.

2.7 Breaching vs. Liquefaction

Dilatancy is most likely to occur in densely packed sand. For loosely packed sand a reduction of the pore volume, called contraction, is more likely. This contraction can cause another type of failure, liquefaction, where due to an increase in pore pressure, the internal friction between particles disappears, and the soil flows as a liquid.

Opposed to breaching failures, which can take several hours, liquefaction is a quick process, usually lasting only seconds. The bathymetry after a liquefaction failure is very similar to that of a breach failure. This can cause the effects of breaching failures to be attributed to a liquefaction failure. For example, for years, bank failures in the Mississippi where attributed to liquefaction, but soil tests revealed that breaching failures where more likely Torrey III et al. (1988) and Padfield (1978).

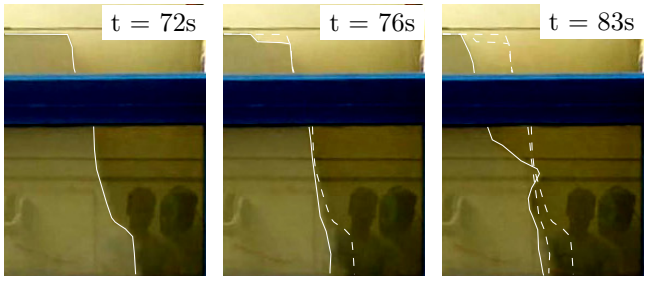

Figure 2.10: A typical sliding wedge observed during breaching. **Left:** The initial profile at t = 72s. **Middle:** Just after the start of the slide. **Right:** The slide has moved down the breach face.

Chapter 3

Laboratory experiments

In this chapter laboratory experiments are described. The main goal of these experiments is to collect data for validation of the numerical model. However, these experiments also allow us to investigate:

- Breaches with slopes above the breach wall. Previous studies start with a flat surface on top of the breach. It is expected that this allows transition from stable to unstable breaching, which until now has only been done in numerical experiments (van Rhee, 2015). It is expected that this transition can be predicted with Equation (2.69).

- The angle of the slope which forms at the toe of the breach. Previous studies either used a suction tube, thus not allowing a slope to develop, or did not document the evolution of this slope. It is expected that angles can be predicted using Equation (2.30), which is often used to predict this angle.

- The frequency of large slides, and their effect on the breaching process. So far the sliding frequency has only been investigated by You et al. (2014). They looked at slides only as a function of sand type, and didn't investigate the effects of these slides. The expectation is that these slides will increase in frequency as breach heights increase, as breach walls become steeper, and as sand becomes more permeable. It is expected that as the number of slides increase, that the wall velocity increases as well.

3.1 Method

3.1.1 Experimental setup

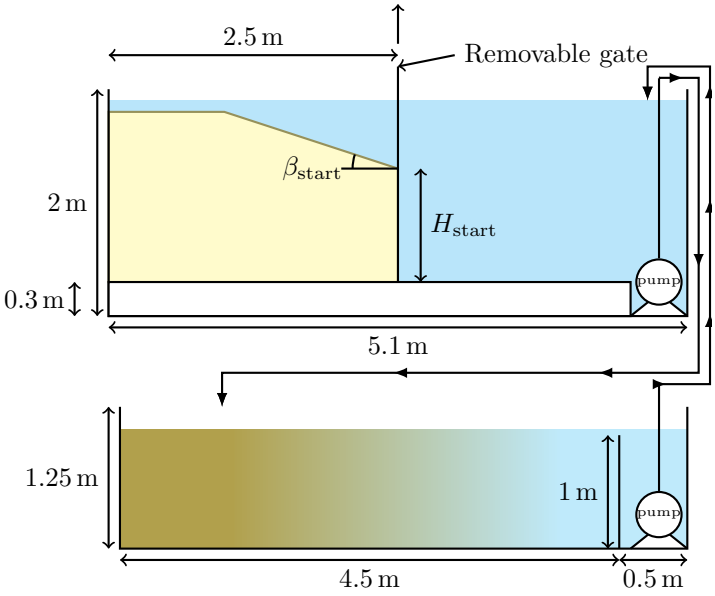

Figure 3.1: The laboratory setup.

The experimental setup consist of a tank with a height of 2 meters, a length of 5.1 meters and a width of 0.5 meters (Figure 3.1). The tank has glass panels on one side (Figure 3.2). The tank is divided into two parts, with lengths of 2.55 meters, by a impermeable removable gate, which can be lifted vertically. A false bottom, with a height of 0.3 meters and a length of 4.8 meters, is placed at the bottom of the tank. This false bottom creates a 0.3 meter long pump sump at one end of the tank.

To reduce the reflection of the turbidity current at the end of the tank, a centrifugal pump is placed inside the pump sump. This pump pumps the sand water mixture from the pump sump to a basin which is 4.5 m long, 1.25 m wide, and 1.25 m high. On the opposite site of the tank a second pump is located behind a 1 m high divider, which pumps clean water back into the tank, to maintain a constant water level.

The whole tank is filled with water. Sand is placed on one side of the

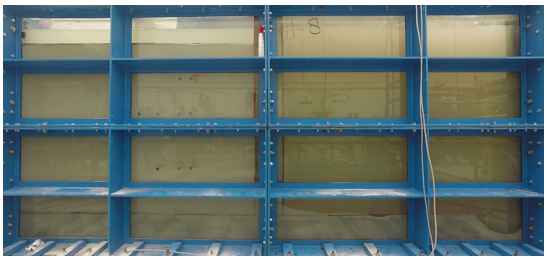

Figure 3.2: Glass panels at one side of the experimental setup, before the start of experiment 8. The view is partially obstructed by metal beams.

removable gate. The sand is placed inside the tank layer by layer, and layers are compacted by using a vibrating needle. The sand body is built up with heights, H_{start}, up to 1.47 m and angles on top of the wall, β_{start}, up to 30° (Table 3.1).

3.1.2 Sand properties

During the experiment two types of sand are used, GEBA and D9 (Table 3.2). The initial porosity, n_0, of each sand type was estimated by taking samples before the start of the experiments for two experiments with GEBA, and two experiments with D9 sand. The median and 15th percentile grain size, D_{50} and D_{15}, are determined using sieves. The internal friction angle, ϕ_c, was determined using a direct shear test. The permeabilities of the sand types are determined with a falling head test. For D9 this was done with a porosity equal to n_0 ('as indicated in Table 3.2), while for GEBA this was done at a lower porosity. Instead, for GEBA sand, the permeability at n_0, k_0, is estimated using the formula of Kozeny-Carman as follows:

$$k_0 = \left(\frac{n_{\text{test}}}{n_0}\right)^3 \left(\frac{1-n_0}{1-n_{\text{test}}}\right)^2 k_{\text{test}}, \tag{3.1}$$

where k_{test} is the permeability measured during the falling head test, with a prosity of n_{test}.

3.1.3 Experimental procedure

Once the sand is in place, and the pumps are started, experiments are started by raising the gate. The whole experiment is filmed from the side with a GoPro

Table 3.1: List of experiments

	H_{start} (m)	β_{start} (°)	sand type
1	0.66	0	GEBA
2	0.66	0	GEBA
3	0.66	0	GEBA
4	1.17	0	GEBA
5	1.17	0	GEBA
6	1.17	0	GEBA
7	0.8	20	GEBA
8	1.47	0	GEBA
9	0.8	30	GEBA
10	1.47	0	GEBA
11	0.66	30	GEBA
12	0.66	20	GEBA
13	0.66	0	D9
14	1.17	0	D9
15	0.8	30	D9
16	1.47	0	D9

Table 3.2: 50th and 15th percentile grain size, D_{50}, D_{15}, initial porosity, n_0, initial permeability, k_0, and internal friction angle, ϕ_c, of the GEBA and D9 sand types.

	D_{50} (µm)	D_{15} (µm)	n_0	k_0 ($\mathrm{m\,s^{-1}}$)	ϕ_c (°)
GEBA	120	80	0.415	9.5×10^{-5}	35.8
D9	330	225	0.430	2.2×10^{-4}	40.1

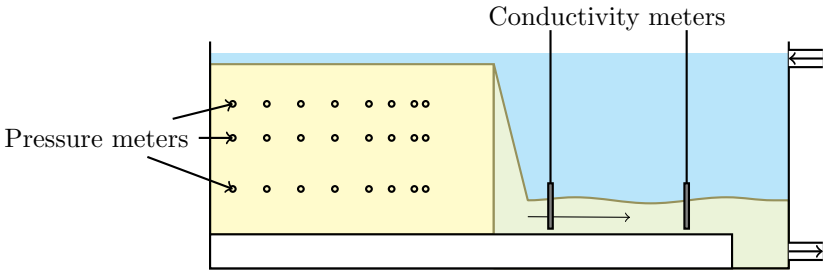

Figure 3.3: Locations of measurement devices used during the experiments.

Hero 3 camera. During the experiments the pore pressure inside the sand body is measured using six to nine differential pressure meters. For these pressure meters, connections are possible on the side of the tank in a three by seven array (Figure 3.3). The connections used differ per experiment. Furthermore, two arrays of conducitivity meters are placed inside the tank, on the side of the gate without sand. Both arrays consist of 10 sensors spread over 0.4 meters. These sensors can measure the conductivity of the sand-water mixture, which can be translated into sand concentration.

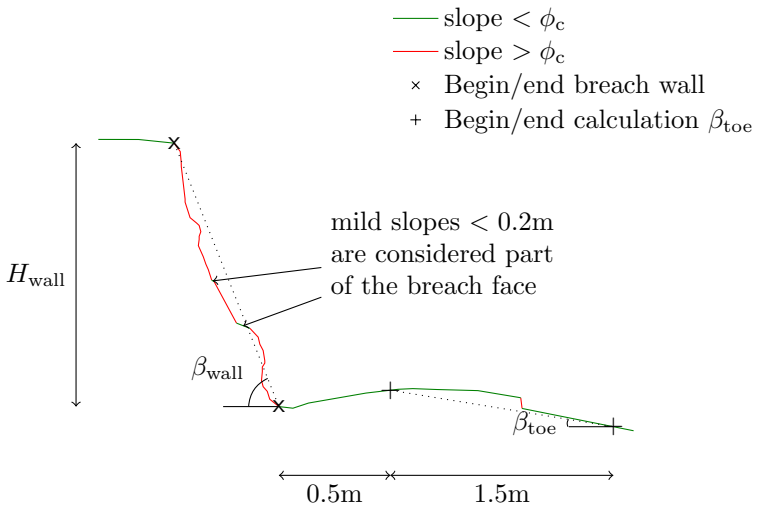

Figure 3.4: Definitions used for the wall height, wall angle and toe angle.

3.1.4 Data analysis

After the experiments, profiles are extracted from the recorded videos (Figure 3.6. From these profiles wall velocity, wall height, wall angle and the slope at the toe are retrieved. This allows for easier analysis and comparison between experiments.

The breach wall is defined as the portion of the profile where the angle is steeper than the internal friction angle. The steep wall can contain small parts where the slope angle is milder than the internal friction angle. These are considered part of the breach wall if they are less than 0.2 m in length. The wall height, H_{wall}, is the vertical distance between the start and end points

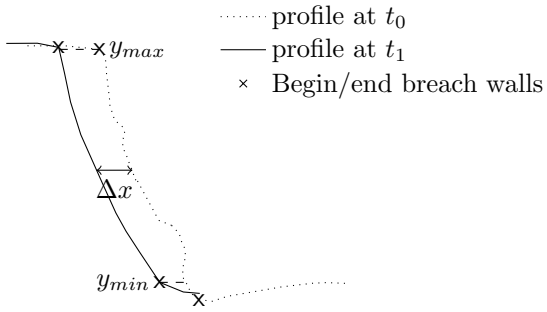

Figure 3.5: Definitions used in determining the wall velocity.

of the breach wall. The wall angle is approximated by the angle of the line between the start and end points of the breach wall (Figure 3.4). The average angle at the toe of the wall is taken between 0.5 and 2 metres from the toe. The toe angle is not determined right after the toe, because often a erosion hole is located in front of the breach face. The toe angle is approximated by using a straight line between the two points at the start and the end of this domain (Figure 3.4). Sometimes, when the turbidity current is large, the transition from turbidity current to still bed cannot be observed. In these cases the toe angle is not determined.

The wall velocity is defined as the average horizontal distance traveled, per unit of time, over the height of the breach wall.

$$v_{\text{wall}} = \frac{\int_{y_{toe}}^{y_{top}} \Delta x(y) \mathrm{d}y}{(y_{top} - y_{toe})\,(t_1 - t_0)}, \tag{3.2}$$

where y_{top}, is the lowest of the two tops of the two profiles, while y_{toe} is the highest of the two toes of the two profiles (Figure 3.5). $\Delta x(y)$ is the horizontal distance between the two profiles at height y. The size of slides is estimated using screenshots before and after a sliding event. Because breaching can continue during slides, the slide volume will be overestimated as it also includes erosion due to normal breaching.

3.2 Results

3.2.1 General observations

Here we discuss the general behavior of a breaching experiment. Raising of the sliding gate is initiated at $t = 0\,\mathrm{s}$, and, for experiment 8, finishes between $t = 10\,\mathrm{s}$ to $17\,\mathrm{s}$, depending on the initial breach height. When raising the gate the underpressure measured inside the sand quickly increases (Figure 3.8c). Afterwards it slowly decreases until the breaching front has passed the pressure meter, after which it measures the hydrostatic pressure. When slides occur nearby a pressure meter a small drop in underpressure is measured.

After raising the gate, the wall velocity reaches it's maximum value (Figure 3.8a), and afterwards continuously decreases, likely due to the simultaneous decrease in wall angle, which starts at 90° and becomes milder over time (Figure 3.8b) . The wall height can initially become steeper than 90 degrees for some experiments. This is because the bottom part of the wall starts eroding while at the top the sand is still held back by the gate. Once the gate is lifted, the wall angle becomes milder again. At the start of the experiments several slides occur, but during the later stages of the experiments these slides are no longer observed (Figure 3.8b).

During experiment 8 ($H_{\mathrm{start}} = 1.47\,\mathrm{m}$, $\beta_{\mathrm{start}} = 0°$, GEBA), after about $750\,\mathrm{s}$ a disturbance is caused by a large slide of the freshly deposited sand at the toe of the breach (Figure 3.7). After the slide, the slope at the toe of the breach is steeper, while further downstream it became milder. Just before the slide a spike in pore pressure is measured inside the soil, the large slide is therefore likely caused by liquefaction. Such large slides do not occur regularly, but similar slides were observed at the end of experiments 5 ($H_{\mathrm{start}} = 1.17\,\mathrm{m}$, $\beta_{\mathrm{start}} = 0°$, GEBA), and 9 ($H_{\mathrm{start}} = 0.80\,\mathrm{m}$, $\beta_{\mathrm{start}} = 30°$, GEBA).

3.2.2 Effect of sand type

Results of a similar experiment, with the coarser and more permeable D9 sand (Experiment 16), show an increase of the maximum wall velocity by a factor 3 (Figure 3.8a). This increase is likely caused by the higher permeability of D9 sand, which plays a big role in Equation (2.28). Due to the increased wall velocity, the total time of the experiment is a factor 8 shorter. This decrease is partially explained by the increased wall velocity. However, the angle of the deposition at the toe of the breach is also steeper than during the same experiment with GEBA (Figure 3.8f), likely due to the larger grain size. Due to the steeper slope, the reduction of the wall height is quicker.

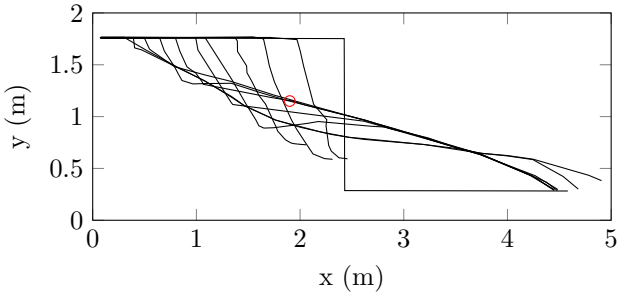

Figure 3.6: Profiles plotted every 90 seconds, for experiment 8. Linear interpolation is used for parts which could not be observed. The red circle shows the location for pore pressure measurements in Figure 3.8

Figure 3.7: A Liquefaction failure observed during experiment 8.

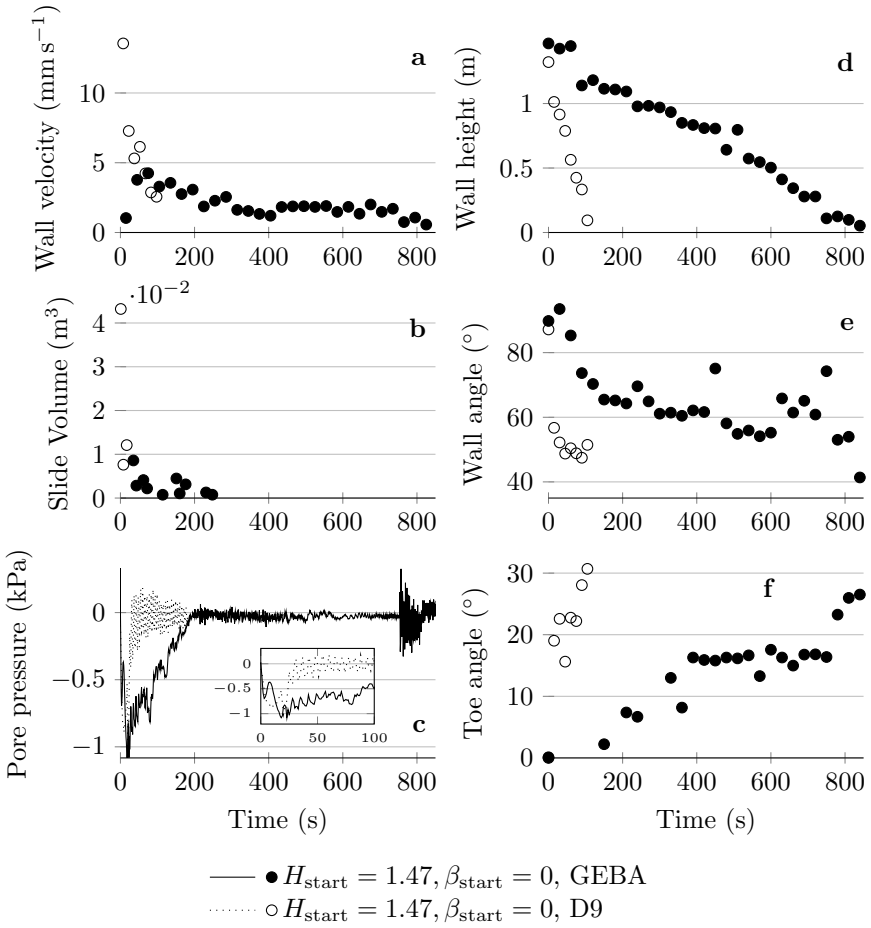

Figure 3.8: For experiment 8 ($H_{\text{start}} = 1.47\,\text{m}$, $\beta_{\text{start}} = 0°$, GEBA) and 16 ($H_{\text{start}} = 1.47\,\text{m}$, $\beta_{\text{start}} = 0°$, D9) a) wall velocity, b) size of slides during experiment, c) underpressures at $x = 1.9, y = 0.7$, d) Wall height, e) wall angle averaged over the height of the wall, and f) Angle of the slope at the toe of the wall.

Interestingly, the initial drop in pore pressure when the gate is raised is almost equal to the drop during experiment 8 (Figure 3.8c). This observation goes against predictions by You et al. (2012), that the maximum pore pressure will increase as permeability decreases. Instead, the maximum pore pressure seems determined by the geometry. This is likely because at a certain pore pressure the yield stress surpasses the shear stress. Then no further shear, and thus shear dilation is expected, and there is no source for decreasing pore pressure. You et al. (2012) do not take this effect into account.

3.2.3 Stable vs unstable breaching

A transition from stable to unstable breaching is found between experiments 11 and 12. These experiments have the same sand type and starting height ($H_{\text{start}} = 0.66$, GEBA) but differing slopes on top of the breach ($\beta_{\text{start}} = 30$ & $\beta_{\text{start}} = 20$ respectively). Both experiments show an initial reduction of the wall height in the first 60 seconds (Figure 3.9d). However, in the following 180 seconds, experiment 11 shows an increase in wall height, while experiment 12 shows a decreasing wall height. During this time other variables, like the wall velocity, wall angle, pore pressure, and toe angle are similar for both experiments. The slides observed during experiment 11 are larger than those observed during experiment 12. After 300 seconds the wall height starts to decrease for experiment 11, because the slope at the top of the breach wall changes from 30 to 0 degrees. A transistion from stable to unstable breaching is also observed for experiments 7 and 9 (GEBA, $H_{\text{start}} = 0.8$, $\beta_{\text{start}} = 20$ & 30). Experiment 15, which uses a slope on top of the breach of 30 degrees as well, did not show unstable behavior. This is likely due to the use of D9 sand. Due to its larger grain diameter, steeper slopes are formed at the toe of the breach (as seen in Figure 3.8f), increasing the reduction of wall height.

3.2.4 Reproducibility

When interpreting data, it is important to take the variance between equivalent experiments into account. Experiments 1, 2 and 3 (GEBA, $H_{\text{start}} = 0.66\,\text{m}$, $\beta_{\text{start}} = 0°$) have the same initial conditions, as do experiments 8 and 10 (GEBA, $H_{\text{start}} = 1.47\,\text{m}$, $\beta_{\text{start}} = 0°$). These are used to give an indication of the reproducibility of the experiments. While these experiments are not sufficient to accurately describe the variance, they give a good first impression.

The largest variation is found in the slides. Not only the individual slides show large differences in size (See e.g. Figure 3.9b), but also the total volume of the slides varies more than 100% between experiments (Table 3.3). On

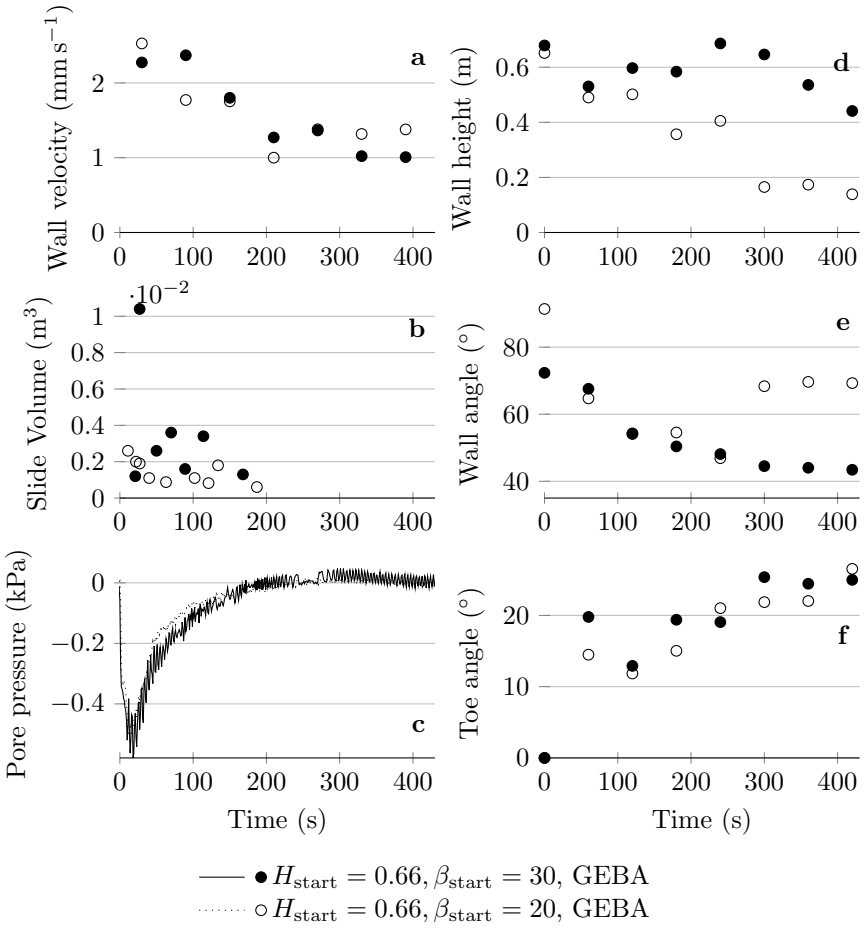

Figure 3.9: For experiment 11 ($H_{\text{start}} = 0.66\,\text{m}$, $\beta_{\text{start}} = 30°$, GEBA) and 12 ($H_{\text{start}} = 0.66\,\text{m}$, $\beta_{\text{start}} = 20°$, D9) a) Wall velocity, b) size of slides during experiment, and c) underpressures at $x = 1.9, y = 0.7$, d) Wall height, e) wall angle averaged over the height of the wall, and f) Angle of the slope at the toe of the wall.

Table 3.3: Mean and maximum differences for variables during compareable experiments.

Experiments	1, 2 & 3	8 & 10
Range total slide volume (m^3)	0.004–0.01	0.029–0.045
Range total horizontal distance (m)	0.53-0.58	2.09-1.93
Mean wall height (m)	0.31	0.88
Mean wall height difference (m)	0.04	0.09
Max. wall height difference (m)	0.20	0.22
Mean wall velocity ($mm\,s^{-1}$)	2.0	2.0
Mean wall velocity difference ($mm\,s^{-1}$)	0.6	0.4
Max. wall velocity difference ($mm\,s^{-1}$)	1.7	1.3
Mean wall angle difference (°)	6.5	7.4
Max. wall angle difference (°)	18.6	19.2
Mean toe angle difference (°)	4.0	2.9
Max. toe angle difference (°)	11.1	4.6

the other hand, the total distance traveled by the breach (Measured by the position of the top of the breach wall), are very close to each other. The mean difference of wall height, wall angle, and toe angle are relatively small, while the mean difference is wall velocity is about 25% of the mean wall velocity (Table 3.3).

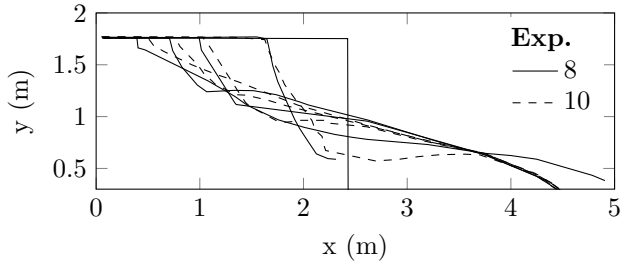

Figure 3.10: Profiles plotted at 0, 180, 410, 600 and 810 seconds for experiments 8 and 10.

The profiles of experiment 8 and 10 (Figure 3.10) look similar with some small differences. The breach face is less steep during experiment 10. The breach moves slightly faster in experiment 8, this might be related to the

difference in wall angle, as Equation (2.28) predict a larger wall velocity for steeper breach faces. The biggest difference is caused by the large liquefaction slide which occurs near the end of experiment 8. No such slide is observed during experiment 10. As a result of this slide the final profiles of both experiments are quite different, and the final distance travelled by the breach face is bigger for experiment 8.

3.2.5 Analysis of slide contribution

During the experiments numerous large slides occur. The largest slide observed is $0.0432\,\mathrm{m}^3$. The largest slide in the less permeable GEBA sand is $0.022\,\mathrm{m}^3$. The size of the slides correlates with the height of the breach face, with bigger slides occurring with higher breach faces. More interesting than total size of the slides, is their contribution to the erosion of the breach face, relative to the total erosion by a combination of slides and pure breaching.

The slide contribution, p_{slide}, during a time interval T is

$$p_{\mathrm{slide}} = \frac{\int_T v_{\mathrm{wall}} H_{\mathrm{wall}} B \mathrm{d}t}{\sum V_{\mathrm{slide}}}, \tag{3.3}$$

where B is the width of the breach wall, and V_{slide} is the volume of a slide.

For GEBA Weiss experiments, the contribution of slides to the total erosion, averaged over different wall heights, shows a larger contribution at larger wall heights, with a contribution of 21 % when the wall height is between 1.3 m and 1.5 m (Figure 3.11a). However, splitting the data by starting heights (Figure 3.11b) shows a large variation in contribution for the same height range. It shows that, instead, the highest contribution to the erosion occurs with a wall height closest to the starting height.

The wall angle is a better predictor for slide contribution (Figure 3.12). The contribution rises from 0% below a wall angle of 50°, up to 16% between 80° and 90°. Splitting over different starting heights, shows less variation than with wall heights. However, it should be noted that all experiments have the same starting wall angle of 90°. Interestingly, in a given bin, the experiments with the largest starting height, never have the largest slide contribution.

The type of sand used has a large impact on slides. Experiments using the more permeable D9 show a significantly higher slide contribution. For wall angles between 80° and 90°, the slide contribution is 81%, meaning almost all erosion is due to slides. The contribution quickly drops as wall angle decreases. For angles between 80° and 70°, the contribution dropped to 18%. For angles below 50°, the contribution drops to zero for D9 as well.

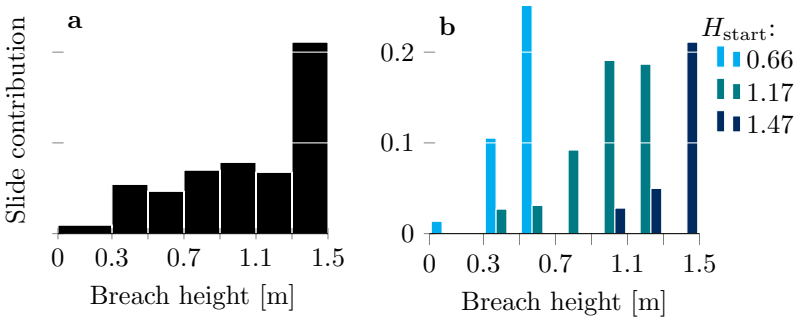

Figure 3.11: Contribution of the sliding wedges to the total erosion volume of the breach face, averaged over different ranges of wall height, for a) all experiments using Geba Weiss, and b) divided by different starting heights.

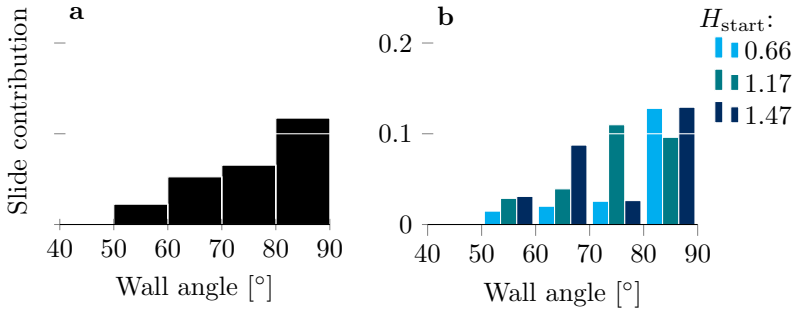

Figure 3.12: Contribution of the sliding wedges to the total erosion volume of the breach face, averaged over different ranges of wall angle, for a) all experiments using Geba Weiss, and b) divided by different starting heights.

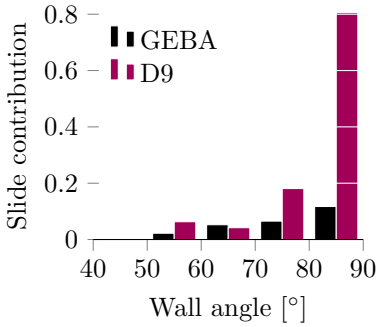

Figure 3.13: Contribution of the slidies to the total erosion volume of the breach wall, averaged over different wall angle ranges, for GEBA and D9 sand.

3.2.6 Analysis of wall velocity

Observed wall velocities compare well to predicted wall velocities (Figure 3.14), with a standard deviation of $1.5\,\mathrm{mm\,s^{-1}}$, and an r^2 value of 0.88. A positive correlation between wall height and the ratio of measured and theoretical velocities (calculated with Equation (2.28)) was found (Figure 3.15, $p = 0.005$). The variation in the results is only partly explained by effects of the wall height, with an r^2 value of 0.24.

A correlation between the slide contribution and the wall velocity was expected, as during slides large volumes of sand are eroded quicker than during breaching. Thus it was expected that, when the contribution by slides increases, the measured velocity would be higher than the theoretical. Instead, a slightly negative correlation was found, with velocities less than the theoretical velocity when slide contribution is the largest (Figure 3.16, $p = 0.004$, $r^2 = 0.41$).

3.2.7 Analysis of breach stability

The stability criterion, Equation (2.70), assumes that 1) the slope angle at the toe of the breach can be predicted using the simplified formula of Mastbergen et al. (1988) proposed by van Rhee (2015) (Equation (2.30)), and that 2) the change in breach height can be predicted based on this slope angle. In this section we test both assumptions based on the experimental results.

Observed toe angles are mostly lower than predicted angles (Figure 3.17). For low sand flux, s, Equation (2.30) predicts unrealistic values, steeper than

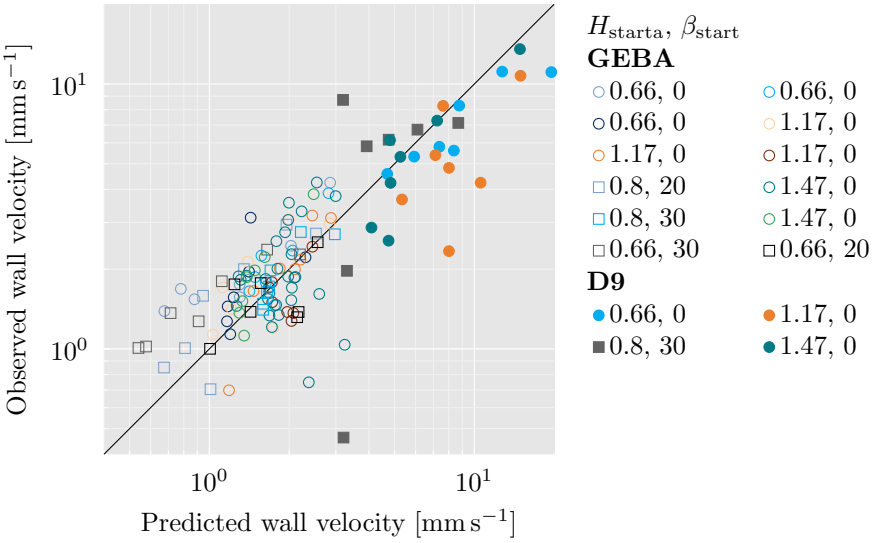

Figure 3.14: The total measured wall velocity (including slides) compared to Equation (2.28).

the angle of repose. If we ignore angles steeper than the angle of repose, the observed angle is on average, 7.1° degrees milder than predicted, with a standard deviation of 4.6°. This average difference is constant over the whole range of predicted values.

It is possible that time factors play a role here, as the equilibrium angle predicted by Equation (2.30) is not reached instantly. It is possible that the observed slope angles are not the equilibrium angles. If this is the case, we would expect the slope angle to change less when it is close to the predicted angle (assuming the predicted angle is close to the actual equilibrium angle). This is not the case however (Figure 3.18), instead we sea that the difference between actual and predicted angle shows little correlation with the change of slope angle.

There is a clear correlation between the relative angle at the toe, and the change in wall height over distance (Figure 3.19, $p = 1.6 \times 10^{-15}$), although with a rather large spread ($r^2 = -0.58$). There is a stronger decrease in wall height than predicted by Equation (2.70), and the change from stable to unstable does not occur at a relative angle of 0°. If we apply a linear regression to all the data points, we find a transition from stable to unstable

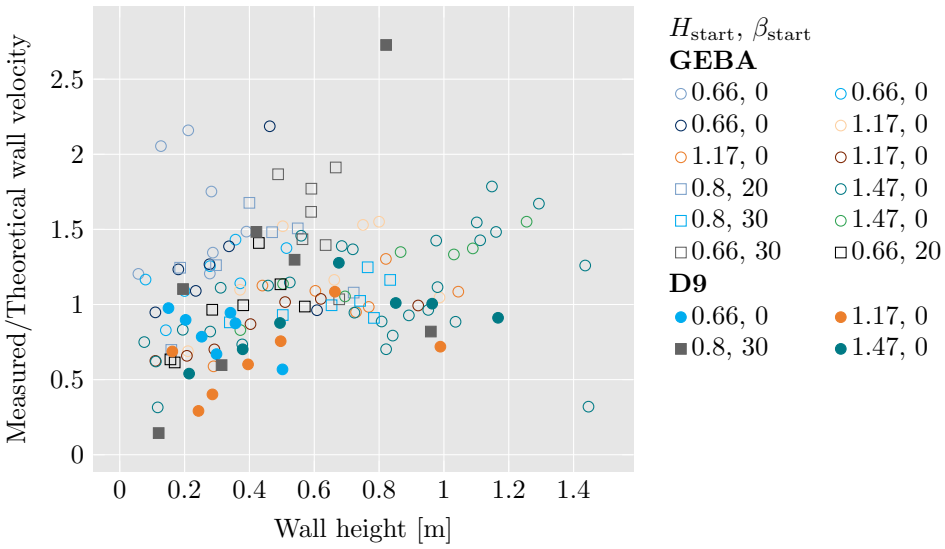

Figure 3.15: The ratio between measured and theoretical (Equation (2.28)) wall velocity as a function of wall height.

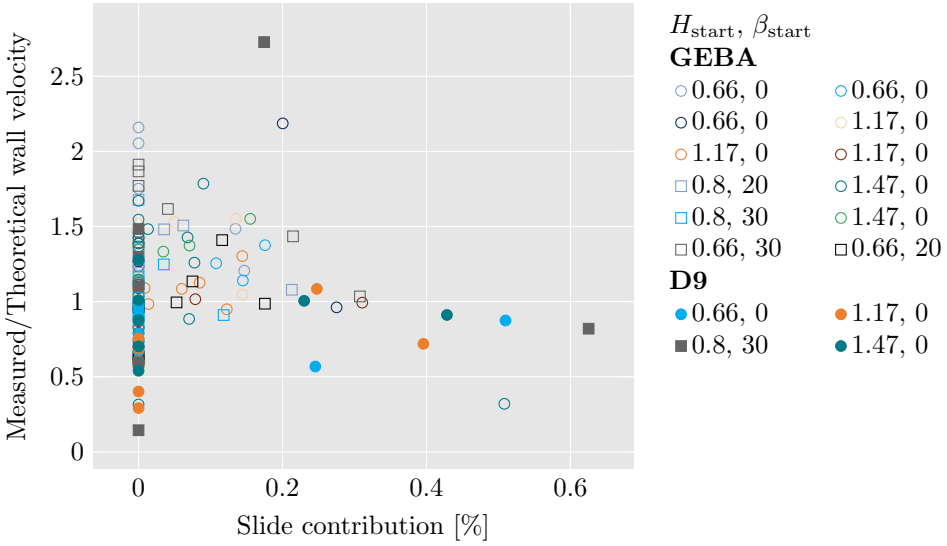

Figure 3.16: The ratio between measured and theoretical (Equation (2.28)) wall velocity as a function of slide contribution.

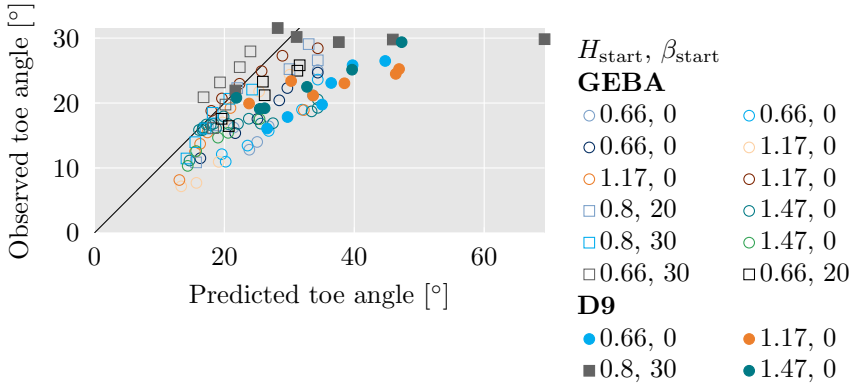

Figure 3.17: Measured slope angle at the toe theory plotted against Equation (2.30).

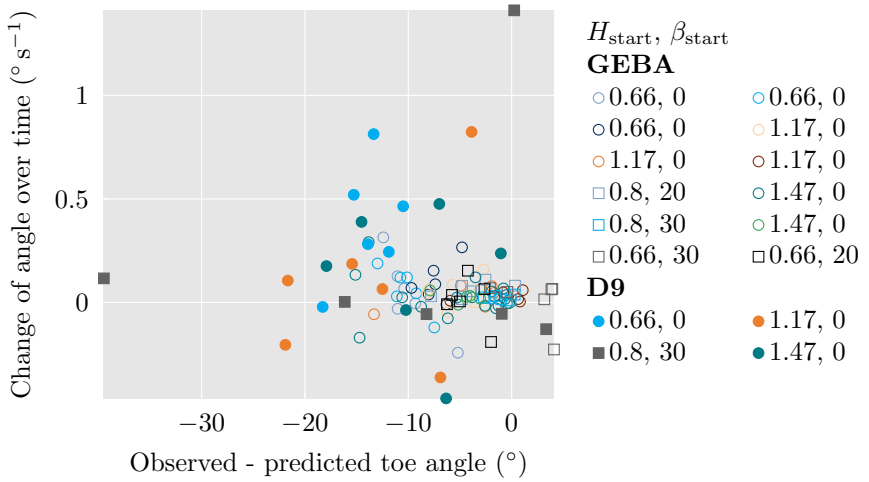

Figure 3.18: The difference between the predicted (Equation (2.30)) and measured toe angle, plotted against the change in toe angle over time.

at $\tan\beta_{toe} - \tan\beta_{top} < -0.34$, which corresponds to a difference of about 19°. However, visual inspection of the data points shows that most data points with $\tan\beta_{toe} - \tan\beta_{top} < -0.2$, show an increasing wall height, and are thus unstable. This corresponds to a angle difference of about 11°.

The angle at the toe of the breach wall can be estimated using the sand properties and the flux, which can be estimated using sand properties, wall height and wall angle. Thus, an estimation of the stability of a breach can be given using the current wall height and wall angle.

3.3 Concluding remarks

With the current experimental setup it was possible to initiate both stable and unstable breaches. While unstable breaching was observed in two of our experiments, the amount of data points during unstable breaching is limited. It is therefore recommended to carry out additional experiments in the unstable breaching regime.

Measured wall velocities correspond well with velocities predicted by Equation (2.28). A positive correlation between wall velocity and wall height is found, where Equation (2.28) underpredicts the wall velocity for higher wall

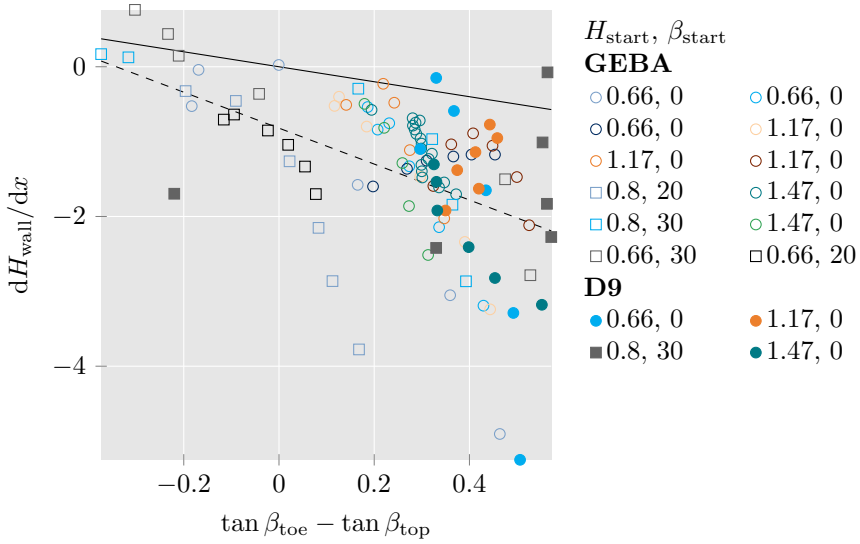

Figure 3.19: The change in wall height plotted against the tangent of the slope at the toe minus the tangent of the slope on top of the breach. The solid line is the value predicted by (Equation (2.70)). The dashed line is the result of a linear regression, and is equal to $-0.82 - 2.4(\tan\beta_{\mathrm{toe}} - \tan\beta_{\mathrm{top}})$

heights. The wall height only accounts for 21 percent of the variance of the wall velocity.

In these experiments the volume of particles released from the breach face via slides, relative to the volume of particles released one by one at the breach face, is largest when the breach height is largest. However, splitting the results by different starting heights, shows that this is because the highest wall heights are found at the start of experiments, and most slides occur near the start of the experiment, irrespective of the breach height (Figure 3.11b). Slides also occur more often when the breach wall is steeper. Because all experiments start with the same wall angle, it is unclear whether this is because the steepest wall angles coincide with the start of the experiment. Contrary to expectations, the wall velocity does not increase as the volume of slides increases (Figure 3.16).

The slopes measured at the toe of the breach correspond well with those predicted by Equation (2.30), but are on average 7.1° milder than predicted. The slope angle formed at the toe of the breach wall correlates with the change in wall height, but a large spread in results is observed (Figure 3.19). Thus predictions of breach stability can be made using Equations (2.28) and (2.30), but with large uncertainty, it is therefore worthwhile to further investigate the breaching process.

Chapter 4

Model Equations

This chapter contains the governing equations underlying the numerical model. It introduces the fluid mechanical equations, followed by the rheology of the soil, and finally a mathematical description of the pore-pressure feedback.

4.1 Model requirements

The goal of the numerical model is the modelling of large three-dimensional breaches. Available models used for breaching do not include movement of the dense soil. They assume the soil the be completely static, with only particles leaving the soil at the soil-water interface at a steady rate. However, large slides during breaching are expected to have a large impact for higher breach heights, which cannot be modelled with current approaches. The requirements for the model can thus be roughly split into three parts:

- The flow of particles suspended in a liquid, to model the turbulent turbidity current, and its interaction with surrounding water.
- The dense sandy soil, where friction forces dominate over hydrodynamic forces, including the effects of pore pressure feedback. To model the slides frequently occurring during breaching, we require a model which can reproduce the transition from static of yielding soil, and the large scale deformations after this transition.
- The interaction of the turbidity current with the dense sandy soil. The pick-up of sediment from the bed, and the sedimentation of particles in the turbidity current to the bed

4.2 Governing equations for dilute suspensions

Two main approaches exist for modelling of dispersed solid particles in a liquid: First, the Lagrangian approach, where individual particles, or groups of particles, are tracked (e.g. Patankar and Joseph, 2001; Nabi et al., 2013). Particle positions are updated based on the forces acting on it. Second, the Eulerian approach, where particle characteristics are averaged over time, volume or ensembles, leading to a fluid-like description of the particles (e.g. de Wit, 2010; van Rhee, 2002). Instead of particles, the concentration of particles is tracked, and is updated by solving and advection diffusion equation.

The Lagrangian method allows for more detailed modelling of the dispersed particle phase, with individual particle tracks. Forces due to particle-particle interactions follow directly from the simulation, while in the Eulerian framework a closure relation is necessary to model diffusion due to particle-particle interactions Particle reflection at the boundary can also easily be applied in a Lagrangian framework. The Lagrangian method also deals better when particles undergo large accelerations (Durst et al., 1984). However, as the number of particles increases, so does the computational effort required. This thesis deals with large scale simulations with large amounts of particles. Individual particle tracks, and interaction with the boundary are unimportant, and large accelerations are not expected. Therefore, the benefits do not justify the increased computing power, and the Eulerian method is chosen.

4.2.1 Navier-Stokes

Fluid flow is described by the Navier-Stokes equations, which includes a mass and a momentum balance. The mass balance is described by

$$\frac{\partial \rho}{\partial t} + \nabla \cdot \rho \underline{\boldsymbol{u}} = 0, \tag{4.1}$$

where: ρ is the density, t is time, and $\underline{\boldsymbol{u}}$ is the velocity.

While the momentum balance is given by

$$\rho \frac{\mathrm{D}\underline{\boldsymbol{u}}}{\mathrm{D}t} = \rho \underline{\boldsymbol{g}} - \nabla p + \nabla \cdot \underline{\boldsymbol{\tau}}, \tag{4.2}$$

where $\frac{\mathrm{D}}{\mathrm{D}t}$ is the material derivative

$$\frac{\mathrm{D}}{\mathrm{D}t} = \frac{\partial}{\partial t} + u \cdot \nabla, \tag{4.3}$$

g is the gravitational acceleration, p is the pressure, and $\underline{\boldsymbol{\tau}}$ is the deviatoric stress tensor, equal to total stress minus the pressure, which are handled separately. The divergence of this term takes the following form,

$$\nabla\cdot\underline{\boldsymbol{\tau}} = \nabla\cdot\mu_c\left[\left(\nabla\underline{\boldsymbol{u}} + (\nabla\underline{\boldsymbol{u}})^T\right) - \frac{2}{3}\underline{\underline{\boldsymbol{I}}}\,\nabla\cdot\underline{\boldsymbol{u}}\right], \tag{4.4}$$

where μ_c is the dynamic viscosity, and $\underline{\underline{\boldsymbol{I}}}$ is the identity tensor.

4.2.2 Two-fluid Approach

To arrive at separate balance equations for different phases Equations (4.1) and (4.2) are multiplied by a phase indicator, χ^k:

$$\chi^k(x,y,z,t) = \begin{cases} 1 & \text{if point } (x,y,z) \text{ is in the } k\text{th phase at time } t, \\ 0 & \text{otherwise.} \end{cases} \tag{4.5}$$

The different phases, the dispersed solid particles and fluid, are assumed to be separated by an infinitesimally small interface. The time or space average of χ_k is α_k.

For practical purposes these formulas need to be averaged over time, space, or ensembles. Here time averaging is used. For single phase flow Reynolds averaging is usually applied. In Reynolds averaging variables are decomposed into an average and a fluctuating part:

$$\psi = \overline{\psi} + \psi', \tag{4.6}$$

where

$$\overline{\psi} = \frac{1}{T}\int_T \psi\,\mathrm{d}t\,. \tag{4.7}$$

For multiphase flows often Favre averaging is applied instead of the simpler Reynolds averaging. For multi-phase flow this leads to simpler equations. Velocities are decomposed in a mass weighted average and a fluctuating component:

$$\psi = \widehat{\psi} + \psi'', \tag{4.8}$$

where

$$\widehat{\psi} = \frac{\overline{\rho\psi}}{\overline{\rho}}. \tag{4.9}$$

Other variables are decomposed in a phase weigthed average and a fluctuating component:

$$\psi = \overline{\overline{\psi}} + \psi''', \tag{4.10}$$

where

$$\overline{\overline{\psi_k}} = \frac{\overline{\chi_k \psi_k}}{\overline{\chi_k}} = \frac{\overline{\chi_k \psi_k}}{\alpha_k}. \tag{4.11}$$

Applying these averages, Ishii and Hibiki (2011) give:

$$\frac{\partial \alpha_k \overline{\overline{\rho_k}}}{\partial t} + \nabla \cdot \left(\alpha_k \overline{\overline{\rho_k}} \widehat{\underline{\boldsymbol{u}}_k} \right) = \Gamma_k, \tag{4.12}$$

and

$$\begin{aligned} \frac{\partial \alpha_k \overline{\overline{\rho_k}} \widehat{\underline{\boldsymbol{u}}}_k}{\partial t} + \nabla \cdot \left(\alpha_k \overline{\overline{\rho_k}} \widehat{\underline{\boldsymbol{u}}}_k \widehat{\underline{\boldsymbol{u}}}_k \right) = \\ -\nabla \left(\alpha_k \overline{\overline{p_k}} \right) + \nabla \cdot \left[\alpha_k \left(\underline{\boldsymbol{\tau}}_k + \underline{\boldsymbol{\tau}}_k^{Re} \right) \right] + \alpha_k \overline{\overline{\rho_k}} \widehat{\underline{\boldsymbol{g}}}_k + \underline{\boldsymbol{M}}_k, \end{aligned} \tag{4.13}$$

where the subscript, k, indicates the phase. Γ_k is the mass generation at the interface, for phase k. For solid particles in a fluid this variable is 0. $\underline{\boldsymbol{M}}_k$ is the average interfacial momentum source for phase k, the main contribution is the drag force. p_k is the normal pressure in phase k. Ishii and Hibiki (2011) assumed that the pressure is the same in the continuous, and the dispersed phase. This assumption is correct for liquid droplets dispersed in liquid, but not for interacting particles dispersed in liquid, or particles in constant contact. Then the particle pressure consists of a combination of the continuous phase pressure, p_c, and a pressure due to particle interactions or contact (Wachem et al., 2004):

$$\nabla \left(\alpha_\mathrm{d} p_\mathrm{d} \right) = \nabla \left(\alpha_\mathrm{d} p_\mathrm{c} + p_\mathrm{eff} \right) \tag{4.14}$$

Averaging introduced an extra term, $\nabla \cdot \underline{\boldsymbol{\tau}}^{Re}$, which represent the effect of the turbulent fluctuations of the velocity on the mean motion.

To solve the equations, the average stress terms, $\underline{\boldsymbol{\tau}}_k$, the turbulent stress terms, $\underline{\boldsymbol{\tau}}_k^{Re}$, the interaction forces between phases, $\underline{\boldsymbol{M}}_k$, and the particle pressure, p_{eff}, require closure.

4.2.3 Mixture model

If the response of particles to changes in flow velocity are quick relative to the timescale of velocity variations the equations can be simplified by using the local equilibrium assumption with minimal errors (Johansen et al., 1990). In the local equilibrium assumption it is assumed that there is no acceleration of the particles relative to the mean flow. If this assumption is true, then the determination of the difference in velocity between the dispersed phase, and the continuous phase is straightforward. The particle response time relative to the timescale of the velocity variations can be expressed with the Stokes number, St:

$$St = \frac{t_p}{t_f}, \tag{4.15}$$

where t_f is the timescale of the velocity variations, and t_p is the relaxation time of a particle accelerating to terminal fall velocity. For small Reynolds particle numbers, for spherical particles this can be calculated using stokes drag as (Clift et al., 2005):

$$t_p = \frac{\rho_{\text{d}} D^2}{18 \mu_c}. \tag{4.16}$$

For Reynolds particle numbers above 1×10^3, the drag coefficient can be estimated as constant around 0.44. The relaxation time is then

$$t_p = \frac{2 \rho_{\text{d}} D}{3 C_D \rho_{\text{c}} w_{\text{d}}}. \tag{4.17}$$

The breaching process occurs in fine sands, with diameters up to 300 µm. This translates to a relaxation time around 4 ms. Based on simulations, it is assumed that the characteristic time scale for the fluid, t_f, does not drop below 0.1 s, and thus the Stokes number is at most 0.04.

Because during the breaching process Stokes number are generally low, the local equilibrium can be used without much error. With this assumption closure for the often complicated interaction forces between phases, $\underline{\boldsymbol{M}}_k$, is no

longer necessary. This term is removed from the governing equations in the mixture model. In the mixture model the balance equations for the different phases are summed to produce balance equations for the mixture. The number of equations to be solved can be reduced by applying the mixture model, reducing the required computational effort. Another benefit is that closure of the particle pressure, p_{eff}, is no longer required. Here the mixture approach of Manninen et al. (1996) is followed.

The continuity equation (Equation (4.12)) is summed over all phases, which in this application are only the continuous and dispersed phases. This summation results in

$$\frac{\partial}{\partial t}\sum_{k=1}^{\text{phases}}(\alpha_k\rho_k)+\nabla\cdot\sum_{k=1}^{\text{phases}}(\alpha_k\rho_k\underline{\boldsymbol{u}}_k)=\sum_{k=1}^{\text{phases}}\Gamma_k, \tag{4.18}$$

where $k = 1$ is the continous phases, and $k \geq 2$ are the dispersed phases. Because of mass conservation, the right hand side of Equation (4.18), is equal to zero. Equation (4.18) can be rewritten as

$$\frac{\partial\rho_m}{\partial t}+\nabla\cdot(\rho_m\underline{\boldsymbol{u}}_m)=0, \tag{4.19}$$

where ρ_m is the mixture density, and $\underline{\boldsymbol{u}}_m$ is the velocity of the centre of mass of the mixture. These are defined as

$$\rho_m=\sum_{k=1}^{\text{phases}}\alpha_k\rho_k \tag{4.20a}$$

$$\underline{\boldsymbol{u}}_m=\frac{1}{\rho_m}\sum_{k=1}^{\text{phases}}\alpha_k\rho_k\underline{\boldsymbol{u}}_k \tag{4.20b}$$

The momentum equations (Equation (4.13)) are summed as well. This leads to the following equation

$$\frac{\partial}{\partial t}\rho_m\underline{\boldsymbol{u}}_m+\nabla\cdot(\rho_m\underline{\boldsymbol{u}}_m\underline{\boldsymbol{u}}_m)=-\nabla p_m+\nabla\cdot\left(\underline{\boldsymbol{\tau}}_m+\underline{\boldsymbol{\tau}}_m^{Re}+\underline{\boldsymbol{\tau}}_m^{\mathrm{D}}\right)-\rho_m g+\underline{\boldsymbol{M}}_m, \tag{4.21}$$

where $\underline{\boldsymbol{M}}_m$ is the influence of the surface tension force on the mixture, which is equal to zero for solid particles. p_m is the mixture pressure, and is equal to

the sum of the pressures of each phase, $\underline{\boldsymbol{\tau}}_m$ is the mixture shear stress, and its divergence is

$$\nabla\cdot\underline{\boldsymbol{\tau}}_{\mathrm{m}} = \nabla\cdot\mu_{\mathrm{m}}\left[\left(\nabla\underline{\boldsymbol{u}} + (\nabla\underline{\boldsymbol{u}})^T\right) - \frac{2}{3}\underline{\underline{\boldsymbol{I}}}\,\nabla\cdot\underline{\boldsymbol{u}}_{\mathrm{m}}\right], \tag{4.22}$$

where μ_m is the mixture viscosity, which according to Vand (1948) can be estimated with

$$\mu_m = \mu_c\left(1 + 2.5\alpha_{\mathrm{d}} + 7.349\alpha_{\mathrm{d}}^2\right). \tag{4.23}$$

For low particle concentrations, the last term becomes negligible and the theoretical formula of Einstein (1906) is found. The term $\underline{\boldsymbol{\tau}}_m^{\mathrm{D}}$ represents the diffusion stress due to the differences between phase velocity and mixture velocity.

$$\underline{\boldsymbol{\tau}}_m^{\mathrm{D}} = -\sum_{k=1}^{\text{phases}} \alpha_k\rho_k\left(\underline{\boldsymbol{u}}_k - \underline{\boldsymbol{u}}_{\mathrm{m}}\right)\left(\underline{\boldsymbol{u}}_k - \underline{\boldsymbol{u}}_{\mathrm{m}}\right). \tag{4.24}$$

Often the mixture model equations are rewritten to contain the drift flux velocity (Hence the name drift flux model) (e.g. Ishii and Hibiki, 2011; Manninen et al., 1996; Brennan, 2001). The drift flux velocity is the difference between the velocity of a phase and the volumetric flux of the mixture. The volumetric flux, $\underline{\boldsymbol{j}}$, is the velocity of the volume centre (opposed to the mixture velocity, which is the velocity of the mass centre). It is defined as follows,

$$\underline{\boldsymbol{j}} = \sum_{k=1}^{\text{phases}} \alpha_k\underline{\boldsymbol{u}}_k. \tag{4.25}$$

The drift flux is defined as

$$\underline{\boldsymbol{v}}_{kj} = \underline{\boldsymbol{u}}_k - \underline{\boldsymbol{j}}. \tag{4.26}$$

$\underline{\underline{\boldsymbol{\tau}}}_{\mathrm{m}}^{\mathrm{D}}$ then becomes

$$\underline{\boldsymbol{\tau}}_{\mathrm{m}}^{\mathrm{D}} = \frac{\alpha_{\mathrm{d}}}{\alpha_{\mathrm{c}}}\frac{\rho_{\mathrm{c}}\rho_{\mathrm{d}}}{\rho_{\mathrm{m}}}\underline{\boldsymbol{v}}_{dj}\underline{\boldsymbol{v}}_{dj}. \tag{4.27}$$

Where $\underline{\boldsymbol{v}}_{dj}$ is the drift-flux of the dispersed phase relative to the volumetric flux. Finally the continuity equations of the dispersed phase, d, is rewritten using the mixture velocity, $\underline{\boldsymbol{u}}_{\mathrm{m}}$, and the drift flux velocity, $\underline{\boldsymbol{v}}_{dj}$:

$$\frac{\partial}{\partial t}\left(\alpha_{\mathrm{d}}\rho_{\mathrm{d}}\right) + \nabla\cdot\left(\alpha_{\mathrm{d}}\rho_{\mathrm{d}}\underline{\boldsymbol{u}}_{\mathrm{m}}\right) = -\nabla\cdot\left(\alpha_{\mathrm{d}}\frac{\rho_{\mathrm{c}}\rho_{\mathrm{d}}}{\rho_{\mathrm{m}}}\underline{\boldsymbol{v}}_{dj}\right). \tag{4.28}$$

The drift-flux, $\underline{\boldsymbol{v}}_{dj}$, can be separated into several components:

- The drift-flux due to settling of the heavier dispersed particles, $\underline{\boldsymbol{v}}_{dj}^{\mathrm{settle}}$.
- The drift-flux due to turbulent diffusion, $\underline{\boldsymbol{v}}_{dj}^{\mathrm{diff}}$.
- The drift-flux due to pick-up of sediment at the soil-mixture interface, $\underline{\boldsymbol{v}}_{dj}^{\mathrm{ero}}$.
- The drift-flux due to the flow of the continuous phase through the pores of the dispersed phase, $\underline{\boldsymbol{v}}_{dj}^{\mathrm{Darcy}}$.

In settlingFOAM, only the flux due to settling and turbulent diffusion is taken into account.

Because of the equilibrium assumption the terminal settling velocity can be used to compute $\underline{\boldsymbol{v}}_{dj}^{\mathrm{settle}}$. In essence this is the same as assuming a constant interaction force, M_p, and no acceleration of the particles relative to the continuous phase. The effect of the concentration on the drift flux is computed with the formula of Richardson and Zaki (1954) as described in Section 2.3:

$$\underline{\boldsymbol{v}}_{dj}^{\mathrm{settle}} = \underline{\boldsymbol{v}}_{dj0}^{\mathrm{settle}}(1-\alpha_d)^n, \tag{4.29}$$

where n is the Richardson-Zaki coefficient, and $\underline{\boldsymbol{v}}_{dj0}^{\mathrm{settle}}$ is the drift flux at a concentration of zero, which has to be prescribed by the user.

The diffision component of the drift-flux is

$$\underline{\boldsymbol{v}}_{dj}^{\mathrm{diff}} = \rho_{\mathrm{m}}\frac{\beta\mu_t}{\rho_{\mathrm{c}}\alpha_{\mathrm{d}}}\nabla\frac{\alpha_{\mathrm{d}}}{\rho_{\mathrm{m}}}, \tag{4.30}$$

where β is the turbulent Prandtl/Schmidt number, which controls the diffusion of particles relative to the diffusion of the liquid, and μ_t is the turbulent viscosity.

$\underline{\boldsymbol{v}}_{dj}^{\mathrm{Darcy}}$, and $\underline{\boldsymbol{v}}_{dj}^{\mathrm{ero}}$ will be defined in Chapter 5

4.2.4 Turbulence modelling

Favre averaging leads to an turbulent shear stress term, $\underline{\underline{\boldsymbol{\tau}}}^{Re}$ in the momentum equation (Equation (4.13)). This term contains the effects of the velocity fluctuations and, using the Einstein notation, is defined as:

$$\tau_{ij}^{Re} = \rho\overline{u_i' u_j'}. \tag{4.31}$$

This term is usually taken into account by applying the eddy viscosity concept of as proposed by Boussinesq in 1877. Boussinesq proposed that the turbulent stresses can be related to mean velocity gradients with an eddy viscosity, μ_t, as follows

$$\underline{\underline{\boldsymbol{\tau}}}^{Re} = \mu_t \left(\nabla \underline{\boldsymbol{u}}_{\mathrm{m}} + (\nabla \underline{\boldsymbol{u}}_{\mathrm{m}})^T - \frac{2}{3}\underline{\underline{\boldsymbol{I}}} \nabla \cdot \underline{\boldsymbol{u}}_{\mathrm{m}} \right). \tag{4.32}$$

Note the similarity with the viscous shear stresses (Equation (4.4)).

Closure for μ_t is required. The simplest method is a simple closure relation, Prandtl (1949) suggested the turbulent viscosity could be estimated by multiplying a characteristic mixing length, l_{m}, with a velocity scale, $l_{\mathrm{m}}|\nabla \underline{\boldsymbol{u}}|$.

$$\mu_t = \rho l_{\mathrm{m}}^2 |\nabla \underline{\boldsymbol{u}}_{\mathrm{m}}|, \tag{4.33}$$

where l_{m} needs to be calculated with a closure relation. The velocity scale is better estimated using the turbulent kinetic energy, k_{t}.

$$k_{\mathrm{t}} = \frac{1}{2}\left(\overline{u_x'}^2 + \overline{u_y'}^2 + \overline{u_z'}^2 \right). \tag{4.34}$$

k_{t} is usually determined using a balance equation.

For better determination of the length scale, often a second variable, using another balance equation, is used. The most common variable is the turbulent dissipation, ε, which is the rate at which turbulent kinetic energy is converted into thermal energy in $\mathrm{m^2\,s^{-3}}$.

More detailed descriptions of the flow field can be obtained by Large Eddy Simulation (LES) (Fox, 2012) or Direct Numerical Simulation (DNS) (Moin and Mahesh, 1998). In LES the larger turbulent eddies are solved directly, while only the smaller scales of the turbulence modelled by the turbulence model (Equation (4.32)). LES requires a finer grid, and thus more computing power. In DNS all turbulent scales are modelled directly, and no turbulence model is required. The necessary grid resolution for this is impractical for practical cases.

Buoyant k-ε model

The buoyant k-ε model is used to determine the turbulent viscosity. The buoyant k-ε is similar to the standard k-ε model (Launder and Spalding, 1983), with an added buoyancy term to account for the effect of a density gradient on the turbulence (Brennan, 2001). In the k-ε model, two transport equations for the turbulent kinetic energy, k_t, and dissipation of turbulent energy, ε are solved.

The k-equation is

$$\frac{\partial \rho k_\mathrm{t}}{\partial t} + \nabla\cdot \rho k_\mathrm{t} \underline{\boldsymbol{u}}_\mathrm{m} = \nabla\cdot \frac{\mu_t}{\sigma_k}\nabla k_\mathrm{t} + P - P_b - \rho\varepsilon, \tag{4.35}$$

and the ε-equation is

$$\frac{\partial \rho\varepsilon}{\partial t} + \nabla\cdot \rho\varepsilon \underline{\boldsymbol{u}} = \nabla\cdot \frac{\mu_t}{\sigma_\varepsilon}\nabla\varepsilon + C_{1\varepsilon}\frac{\varepsilon}{k}P - (1 - C_{3\varepsilon})\frac{\varepsilon}{k}P_b - C_{2\varepsilon}\rho\frac{\varepsilon^2}{k}, \tag{4.36}$$

where σ_k and σ_ε are the turbulent Prandtl numbers for k_t, and ε, $C_{1\varepsilon}$, $C_{2\varepsilon}$, and $C_{3\varepsilon}$ are coefficients to be set by the user, P is the turbulent production term and is equal to

$$P = \mu_t \left(\frac{\partial u_i}{\partial x_j} + \frac{\partial u_j}{\partial x_i} \right) \frac{\partial u_i}{\partial x_j}. \tag{4.37}$$

For stably stratified flows ($g \cdot \nabla\rho_\mathrm{m} > 0$), vortices move the denser mixture upward, and the lighter mixture downward. This movement is counteracted by gravity forces, causing a suppression of turbulent fluctuations. For unstably stratified flows ($g \cdot \nabla\rho_\mathrm{m}$) the turbulent fluctuations are instead enhanced. This effect is taken into account via the buoyant production term, P_b.

$$P_b = \frac{C_\mu k_\mathrm{t}}{\varepsilon} \left(g \cdot \nabla\rho \right), \tag{4.38}$$

where C_μ is another coefficient to be supplied by the user. Finally, the turbulent viscosity is calculated as

$$\mu_t = C_\mu \frac{k_\mathrm{t}^2}{\varepsilon}. \tag{4.39}$$

The divergence of the turbulent and normal shear stresses can now be modelled as

$$\nabla\cdot\left(\underline{\boldsymbol{\tau}}_m+\underline{\boldsymbol{\tau}}_{\mathrm{m}}^{Re}\right)=\nabla\cdot\left(\mu_{\mathrm{eff}}\left[\left(\nabla\underline{\boldsymbol{u}}_m+(\nabla\underline{\boldsymbol{u}}_{\mathrm{m}})^T\right)-\frac{2}{3}\underline{\underline{\boldsymbol{I}}}\nabla\cdot\underline{\boldsymbol{u}}_{\mathrm{m}}\right]\right), \tag{4.40}$$

where

$$\mu_{\mathrm{eff}}=\mu_m+\mu_t. \tag{4.41}$$

Values for σ_ε, σ_k, $C_{1\varepsilon}$, $C_{2\varepsilon}$, $C_{3\varepsilon}$, and C_μ need to be supplied. These values are empirically determined. C_μ was found to be 0.09 in the logarithmic region of the boundary layer (Klebanoff, 1955), and can drop to 0.05 in homogeneous shear flows (Tavoularis and Corrsin, 1981), Launder and Spalding (1974) recommend a value of 0.09 (except when dealing with axisymetric jets). $C_{2\varepsilon}$ controls the decay of isotropic turbulence, and was found to be 1.92 experimentally (Comte-Bellot and Corrsin, 1966). Poroseva and Bezard (2001) found that the correct values of $C_{1\varepsilon}$, and the ratio $\sigma_\varepsilon/\sigma_k$ depend on the type of turbulent flow. They found $C_{1\varepsilon}$ ranging from 1.3 for round jets, up to 1.8 for wakes, where the standard value is usually 1.44 (e.g. Launder and Spalding, 1974). The ratio $\sigma_\varepsilon/\sigma_k$ ranged from 1.2 for wakes, up to 1.5 for round jets. The standard values usually used are $\sigma_\varepsilon=1.3$ and $\sigma_k=1$, resulting in a ratio of 1.3 (e.g. Launder and Spalding, 1974). $C_{3\varepsilon}$ should be 0.8 for horizontal buoyant shear layers, and 0 for vertical buoyant shear layers (Maele and Merci, 2006). This can be achieved by replacing $C_{3\varepsilon}$ with

$$C_{3\varepsilon}=0.8\tanh\frac{|u_y|}{\sqrt{u_x^2+u_z^2}}. \tag{4.42}$$

4.2.5 Law of the Wall

Kármán (1930) observed that attached turbulent flows near a wall can be described with the so-called law of the wall. The law of the wall states that the flow profile close to the wall is given by

$$\frac{u}{u_*}=\frac{1}{\kappa}\ln\left(Ey^+\right), \tag{4.43}$$

where

$$y^+ = \frac{y u_*}{\nu_c} \tag{4.44}$$

$$u_* = \sqrt{\frac{\tau_b}{\rho_c}}, \tag{4.45}$$

κ is the von Kármán constant, which varies in different experiments between 0.42 and 0.35 (George, 2007), and E is a function of the wall roughness, and is roughly 9.0 for a smooth wall, and u is the mean streamwise velocity.

Equation (4.43) is valid for values of $y^+ \geq 30$. The region $y^+ \leq 5$ is the viscous sublayer, here the velocity obeys

$$\frac{u}{u_*} = y^+. \tag{4.46}$$

Between $y^+ = 5$ and $y^+ = 30$ is a buffer zone, where the streamwise velocity profile follows neither the law of the wall, nor the equation for the viscous sublayer (Figure 4.1).

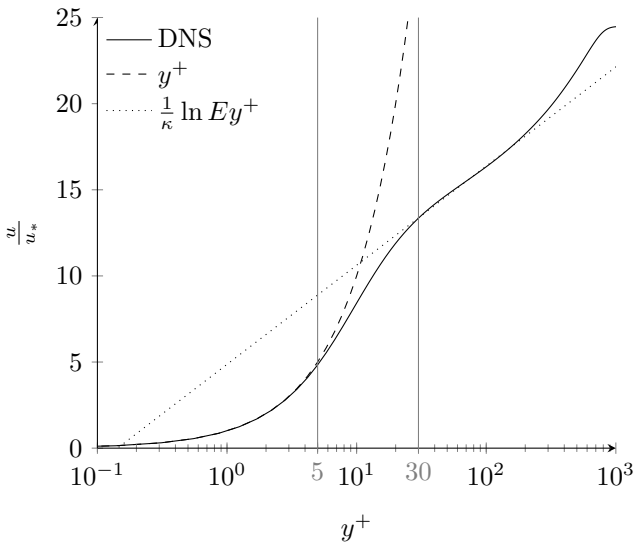

Figure 4.1: Mean streamwise velocity profile along a wall, obtained from DNS measurements by Schlatter and Örlü (2010) ($Re_\tau = 830$), plotted with the law of the wall (Equation (4.43), and Equation (4.46).

4.3 Governing equations for dense suspensions

As particle concentration increases, interaction between particles increases. First, this interaction occurs as collisions between particles. This is called the collisional regime. When the effects of collisions are averaged over time, it can be seen as a dispersive particle pressure. This dispersive pressure scales with the square of the shear rate, $\dot{\gamma}$ (Bagnold, 1954). This pressure disperses the particles (hence its name), and increases the resistance to shearing (Bagnold, 1954).

As concentration increases further ($\alpha_d \gtrsim 0.5$), there will be sustained contact between particles. This is the frictional regime (Figure 4.2), where friction forces between particles dominate the flow.

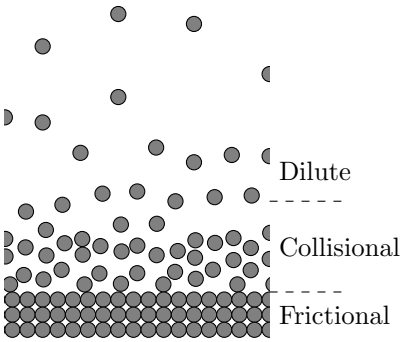

Figure 4.2: An overview of the different particle regimes found during granular flow.

van Rhee (2002) applies the equations of the previous section for flows with concentrations up to 30%, well into the collissional regime. The model results compare well to experiments, it is therefore decided to ignore extra collisional effects. However, a model for the frictional regime is required which is able to:

- Reproduce transition from static to yielding soil, and vice versa,
- Reproduce the right yield surface, and
- Handle large scale deformation.

Classical soil mechanical methods use constitutive laws based on stress-strain relationships (Schofield and Wroth, 1968; Zienkiewicz et al., 1977). These methods can reproduce the transition from static two flowing soil well,

but are not suitable for simulating large scale deformation During the last decade, techniques such as particle finite element (PFEM) (Oñate et al., 2011) and the material point method (Alonso et al., 2015; Ceccato, 2015; Bandara and Soga, 2015) have been developed to address this problem. These methods are able to also reproduce the large scale deformations. However, combining these models with complex turbulent flows remains a challenge.

This work considers a fluid mechanical formulation based on a stress-strain rate constitutive law based on work published by Lalli and co-workers (Lalli and Di Mascio, 1997; Lalli et al., 2005). Jop et al. (2006) extended this method by employing a friction law developed by GDR MiDi (2004), and found good agreement between their results and measurements of granular flows down inclined planes. Cassar et al. (2005) have shown that the model, with some adaptations, also works well for submerged granular flows. Because this method is based on stress-strain it is easily combined with our fluid dynamical model.

4.3.1 Mohr-Coulomb

To incorporate frictional effects in the mixture model, the dense mixture is modelled as a Bingham fluid, as first proposed by Lalli and Di Mascio (1997). This rheology is applied in computational cells where the concentration α is higher than a given threshold value, α_{fric}, to be chosen by the user. In the Bingham rheology the shear stress tensor, $\underline{\underline{\boldsymbol{\tau}}}$, is defined such that:

$$\begin{aligned} \dot{\gamma} &= 0 && \text{if } \tau \leq \tau_y \\ \underline{\underline{\boldsymbol{\tau}}} &= \left(\tfrac{\tau_y}{\dot{\gamma}} + \mu_c\right) \underline{\underline{\boldsymbol{\gamma}}} && \text{if } \tau > \tau_y. \end{aligned} \tag{4.47}$$

Here μ_c is the dynamic viscosity of water in Pa s, $\dot{\gamma}$ is the second invariant of the deformation tensor, $\underline{\underline{\boldsymbol{\gamma}}}$, and, using the Einstein summation convention, is defined as follows:

$$\dot{\gamma} = \sqrt{0.5 \gamma_{ij} \gamma_{ij}}, \tag{4.48}$$

and

$$\underline{\underline{\boldsymbol{\gamma}}} = \gamma_{ij} = \frac{\partial u_i}{\partial x_j} + \frac{\partial u_j}{\partial x_i}. \tag{4.49}$$

When the shear stress is below a given yield stress, τ_y, the rate of strain, characterized by $\dot{\gamma}$, is 0, meaning no shear deformation. When the shear stress is larger than the yield stress, the stress tensor is given by Equation (4.47).

For the yield stress the formula of Coulomb is used:

$$\tau_y = c + p_{\text{eff}} \tan \phi, \tag{4.50}$$

where p_{eff} is the contact stress between particles, per unit area, ϕ_{c} is the internal friction angle, and c is the cohesion of the soil.

The yield stress is applied in the model via an effective viscosity, as follows:

$$\mu_{\text{eff}} = \frac{\tau_y}{\dot{\gamma}} + \mu_m. \tag{4.51}$$

Special care has to be taken when the shear rate, $\dot{\gamma}$, drops to 0, as this would give division by zero problems, this is discussed in Chapter 5. This effective viscosity is applied as in Equation (4.40). Thus:

$$\nabla \cdot \underline{\underline{\boldsymbol{\tau}}}_m = \nabla \cdot \mu_{\text{eff}} \left(\nabla \underline{\boldsymbol{u}}_{\text{m}} + (\nabla \underline{\boldsymbol{u}}_{\text{m}})^{\text{T}} - \frac{2}{3} \underline{\underline{\boldsymbol{I}}} \nabla \cdot \underline{\boldsymbol{u}}_m \right). \tag{4.52}$$

4.3.2 $\mu(I)$ Rheology

We estimate the ratio between shear stress and pressure, using the findings of GDR MiDi (2004). GDR MiDi investigated the results of experiments and discrete particle simulations of different types of dense granular flows in air. They found that the ratio between shear stress and pressure, can be scaled by the so-called inertial number, I. I is the ratio between the macro and mirco time scale of granular flow.

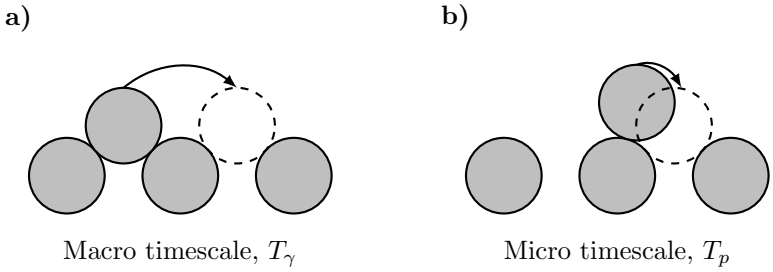

Figure 4.3: Schematic showing the physical meaning of the deformation and confinement time scales [Based on GDR MiDi (2004)]

The macro time, T_γ scale is the time it takes for a particle to move over another particle (Figure 4.3a).

$$T_\gamma = \frac{1}{|\dot{\gamma}|}. \tag{4.53}$$

The micro time scale is related to the time needed by a particle pushed down by the effective pressure, p_{eff}, to find a new position (Figure 4.3b). For dry granular flow this is

$$T_p = D\frac{p_{\text{eff}}}{\rho_{\text{d}}}. \tag{4.54}$$

Then, I is

$$I = \frac{|\dot{\gamma}|D}{\sqrt{p_{\text{eff}}/\rho_{\text{d}}}}. \tag{4.55}$$

The ratio between shear stress and pressure is given by the friction coefficent $\mu(I)$:

$$\mu(I) = \phi_s + I\frac{\phi_2 - \phi_s}{I_0 + I}. \tag{4.56}$$

where ϕ_s is the friction coefficient for static soil, ϕ_2, is friction coefficient at maximum shear rate, and I_0 is a parameter controlling how quickly ϕ_2 is approached.

Because I is a local parameter it cannot take into account non-local effects such as arching or grain clusters. However, this rheology seems to be able to accurately predict many different types of granular flows (Cassar et al., 2005; Jop et al., 2006; Doppler et al., 2007; Jop, 2008; Lagrée et al., 2011).

Jop et al. (2006) created a three-dimensional model for flow of granular material based on the results of GDR MiDi (2004) for dry granular flow. They calculate the yield stress, τ_{y}, as follows,

$$\tau_{\text{y}} = \mu(I)p_{\text{eff}}, \tag{4.57}$$

and the effective viscosity, μ_{eff}, as

$$\mu_{\text{eff}} = \frac{\tau_{\text{y}}}{\dot{\gamma}} + \mu_m. \tag{4.58}$$

Extension to Submerged Flows

Cassar et al. (2005) investigated submarine flows of granular materials down a rough incline. In this case the interstitial fluid plays an important role in the

flow. They found that the flow can still be described by the $\mu(I)$-rheology if a micro time scale is chosen which takes the effect of this interstitial fluid into account. The alternative time scale is based on the work of Courrech du Pont et al. (2003). For particle Reynolds numbers (Equation (2.36)) lower than 2.5, this new timescale is dominated by viscosity and is

$$T_v = \frac{\mu_\mathrm{c}}{p_\mathrm{eff}}, \tag{4.59}$$

and I becomes

$$I_v = \frac{\mu_c|\dot{\gamma}|}{p_\mathrm{eff}}. \tag{4.60}$$

For Reynolds particle numbers larger than 2.5, inertia effects become important. The micro timescale in this regime is

$$T_i = D\sqrt{\frac{2\rho_\mathrm{c}C_\mathrm{D}}{3p_\mathrm{eff}}}. \tag{4.61}$$

The inertial number becomes

$$I_i = |\dot{\gamma}|D\sqrt{\frac{2\rho_\mathrm{c}C_\mathrm{D}}{3p_\mathrm{eff}}}. \tag{4.62}$$

When the ratio between particle and fluid density is smaller than 4 (which is the case for sand particles in water), Equation (4.55) is not used, and only Re_p determines which inertial number is used.

4.4 Pore pressure feedback

The framework presented by Iverson (2013) is used to implement pore pressure feedback in our model.

The dilatancy is linked to the shear rate of the material by the dilatancy angle, ψ. The dilatancy angle is determined using the linearization of Equation (2.14), repeated here

$$\tan\psi = C_\mathrm{dil}\left(\alpha_\mathrm{d} - \alpha_\mathrm{eq}\right). \tag{4.63}$$

The equilibrium concentration, α_eq, is calculated by the following formula proposed by Boyer et al. (2011) (Equation (2.10)),

$$\alpha_{\text{eq}} = \frac{\alpha_{\text{eq;0}}}{1 + \sqrt{I}}. \tag{4.64}$$

The critical concentration, $\alpha_{\text{eq;0}}$, is assumed to be constant, which can be done with little error for effective pressures less than 100 kPa (Boyer et al., 2011).

Besides the change in concentration due to shearing, Iverson (2013) also takes into account the compression caused by a change in the mean effective stress. This leads to the following formula:

$$\frac{1}{\alpha_{\text{d}}} \frac{\partial \alpha_{\text{d}}}{\partial t} = -\nabla \cdot \underline{\boldsymbol{u}}_d = -\tan\psi \dot{\gamma} + C \frac{\mathrm{D}p_{\text{eff}}}{\mathrm{D}t}, \tag{4.65}$$

where C is the compressibility (the reciprocal of the bulk modulus) of the sand skeleton. The formula can also be written as

$$\tan\psi \dot{\gamma} = \nabla \cdot \underline{\boldsymbol{u}}_d + C \frac{\mathrm{D}p_{\text{eff}}}{\mathrm{D}t}. \tag{4.66}$$

It can now be seen that shearing causes a combination of 1) Dilatancy ($\nabla \cdot \underline{\boldsymbol{u}}_d$), and 2) An increase of the effective pressure ($C \frac{\mathrm{D}p_{\text{eff}}}{\mathrm{D}t}$).

To conserve the total volume, the dilatancy or compaction of the sand is countered by an influx or outflux of water.

$$\nabla \cdot \underline{\boldsymbol{u}}_d = -(1 - \alpha_{\text{d}}) \nabla \cdot (\underline{\boldsymbol{u}}_c - \underline{\boldsymbol{u}}_d). \tag{4.67}$$

The term $(1-\alpha_{\text{d}})(\underline{\boldsymbol{u}}_{\text{c}} - \underline{\boldsymbol{u}}_{\text{d}})$ can be linked to the water pressure gradient using Darcy's law (Darcy, 1856).

$$(1 - \alpha_{\text{d}})(\underline{\boldsymbol{u}}_c - \underline{\boldsymbol{u}}_d) = q_f = -\frac{k}{\rho_c \underline{\boldsymbol{g}}} \nabla p_e, \tag{4.68}$$

where q_f is the volumetric flux of pore water per unit area in $\mathrm{m\,s^{-1}}$, p_e is the excess pore water pressure in Pa, and k is the hydraulic permeability in $\mathrm{m\,s^{-1}}$.

Combining Equations (4.66) to (4.68) gives:

$$\nabla \cdot \frac{k}{\rho_c \underline{\boldsymbol{g}}} \nabla p_e = C \frac{\mathrm{D}p_{\text{eff}}}{\mathrm{D}t} - \tan\psi \dot{\gamma}. \tag{4.69}$$

Table 4.1: Overview of partial differntial equations.

Equation	Eq. no.	variables
Mixture mass and momentum balance	4.19 & 4.21	p_{m}, $\underline{\boldsymbol{u}}_{\mathrm{m}}$
Dispersed phase mass balance	4.28	α_{d}
k-ε equations	4.35 & 4.36	k_{t}, ε
Pore pressure equation	4.69	p_e

Table 4.2: Overview of constitutive equations.

Variable	ρ_{m}	$\underline{\boldsymbol{v}}_{dj}$	μ_t	μ_{eff}	ψ	p_{eff}
Equation	4.20a	4.29	4.39	4.58	2.14	See Section 5.2.2

The pore water component of the drift-flux is the opposite of the volumetric flux of pore water, q_f

$$\underline{\boldsymbol{v}}_{dj}^{\mathrm{Darcy}} = -q_f = \frac{k}{\rho_c \underline{\boldsymbol{g}}} \nabla p_e. \tag{4.70}$$

4.5 Summary

Combining everything leaves us with 6 partial differential equations to be solved (Table 4.1). Solving these equations gives us the mixture pressure and velocity, the concentration of dispersed particles, the turbulent kinetic energy and dissipation and the pore pressure. These equations are supplemented with constitutive equations to determine the mixture density, drift-flux, effective and turbulent viscosity, effective pressure, and the dilatancy angle (Table 4.2).

Chapter 5

Numerical Implementation

This chapter describes how the equations described in Chapter 4 are solved numerically. In Chapter 4 formulae to calculate the flow of the sand-water mixuture, as well as granular media were presented. These equations are solved using OpenFOAM (Greenshields, n.d.; Weller et al., 1998), an open-source C++ toolbox for the development of CFD (and other continuum mechanical) solvers. OpenFOAM allows users to easily extend the core program with, among others, their own solvers, boundary conditions and turbulence models. The model described in this thesis is an extension of an existing model, SettlingFoam. The chapter will start with a description of SettlingFoam, after which the extensions of the model are described.

5.1 SettlingFoam

SettlingFoam is a numerical solver for the mixture model equations (Equations (4.19), (4.21) and (4.28)), and is one of the solvers available in OpenFOAM.

5.1.1 Finite volume discretization

OpenFOAM uses an unstructured grid which divides the solution domain into non-overlapping control volumes. Control volumes are bounded by a set of flat faces and each face is shared with only one neighbouring control volume. All variables are stored at the centres of control volumes. To avoid decoupling of pressure and velocity, a method similar to Rhie and Chow (1983) is used. A

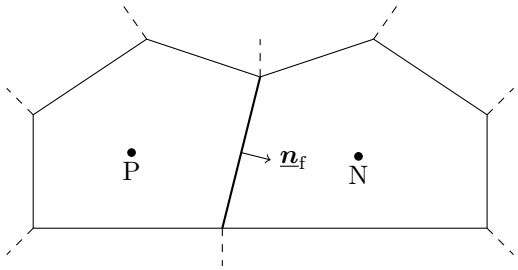

Figure 5.1: A typical control volume in OpenFOAM with centre P, and a neighbouring control volume with centre N. The vector $\underline{\boldsymbol{n}}_\mathrm{f}$ is the unit vector perpendicular to the face between the two control volumes.

typical 2D-representation of a control volume and its neighbour are shown in Figure 5.1, though OpenFOAM functions the same in 3D.

The governing equations are discretized using the finite volume method. To acquire the finite volume discretizations, governing equations are first integrated over a control volume. For example, the dispersed phase continuity (Equation (4.28)) equation becomes

$$\begin{aligned}&\iiint_{CV} \frac{\partial}{\partial t}\left(\alpha_\mathrm{d}\rho_\mathrm{d}\right)\mathrm{d}V + \iiint_{CV} \nabla\cdot\left(\alpha_\mathrm{d}\rho_\mathrm{d}\underline{\boldsymbol{u}}_\mathrm{m}\right)\mathrm{d}V \\ &= -\iiint_{CV} \nabla\cdot\left(\alpha_\mathrm{d}\frac{\rho_\mathrm{c}}{\rho_\mathrm{m}}\underline{\boldsymbol{v}}_{dj}\right)\mathrm{d}V + \iiint_{CV} \nabla\cdot\rho_\mathrm{d}\beta\mu_t\nabla\frac{\alpha_\mathrm{d}}{\rho_\mathrm{m}}\mathrm{d}V,\end{aligned} \tag{5.1}$$

where CV is the control volume. Using the Gauss' divergence theorem, to change the volume divergence integrals into surface flux integrals, this becomes

$$\begin{aligned}&\iiint_{CV} \frac{\partial}{\partial t}\left(\alpha_\mathrm{d}\rho_\mathrm{d}\right)\mathrm{d}V + \iint_{S} \left(\alpha_\mathrm{d}\rho_\mathrm{d}\underline{\boldsymbol{u}}_\mathrm{m}\cdot\underline{\boldsymbol{n}}\right)\mathrm{d}S \\ &= -\iint_{S} \left(\alpha_\mathrm{d}\frac{\rho_\mathrm{c}}{\rho_\mathrm{m}}\underline{\boldsymbol{v}}_{dj}\cdot\underline{\boldsymbol{n}}\right)\mathrm{d}S + \iint_{S} \left(\rho_\mathrm{d}\beta\mu_t\nabla\frac{\alpha_\mathrm{d}}{\rho_\mathrm{m}}\cdot\underline{\boldsymbol{n}}\right)\mathrm{d}V,\end{aligned} \tag{5.2}$$

which can then be numerically discretized in space as

$$\begin{aligned}&\frac{\partial}{\partial t}\left(\alpha_\mathrm{d}\rho_\mathrm{d}\right)_\mathrm{P} V_{CV} + \sum^{\text{faces}} \left(\alpha_{\mathrm{d;f}}\rho_\mathrm{d}\underline{\boldsymbol{u}}_{\mathrm{m;f}}\cdot\underline{\boldsymbol{n}}_\mathrm{f}A_\mathrm{f}\right) \\ &= -\sum^{\text{faces}} \left(\alpha_{\mathrm{d;f}}\frac{\rho_\mathrm{c}}{\rho_{\mathrm{m;f}}}\underline{\boldsymbol{v}}_{dj\,;\mathrm{f}}\cdot\underline{\boldsymbol{n}}_\mathrm{f}A_\mathrm{f}\right) + \sum^{\text{faces}} \left(\rho_\mathrm{d}\beta\mu_t\nabla\frac{\alpha_\mathrm{d}}{\rho_\mathrm{m}}\cdot\underline{\boldsymbol{n}}_\mathrm{f}A_\mathrm{f}\right),\end{aligned} \tag{5.3}$$

where V_{CV} is the volume of the control volume, and A_f is the surface area of the face. The subscript $_\mathrm{P}$ indicates cell averaged values, stored at the centre of the control volume, while $_\mathrm{f}$ indicates face averaged values, stored at the centre of the face. The cell averaged values are regarded as the unknowns for which discretized equations are derived. Interpolation is required to estimate face averaged values. This interpolation introduces an error of $O(\Delta x^n)$, where Δx is the difference between two cell centres, and n depends on the interpolation method used. OpenFOAM has several interpolation methods available, and the user prescribes which method to use. Descriptions of several of these methods can be found in Jasak (1996).

The mixture mass balance (Equation (4.19)) is discretized in space as

$$\frac{\partial}{\partial t}\left(\rho_{\mathrm{m;P}}\right)_\mathrm{P} V_{CV} + \sum_{\text{faces}}^{\text{faces}} \left(\rho_{\mathrm{m;f}} \underline{\boldsymbol{u}}_{\mathrm{m;f}} \cdot \underline{\boldsymbol{n}}_\mathrm{f} A_\mathrm{f}\right) = 0. \tag{5.4}$$

The momentum balance (Equation (4.21)) is discretized in a similar way.

$$\begin{aligned}
&\frac{\partial}{\partial t}\left(\rho_\mathrm{m}\underline{\boldsymbol{u}}_\mathrm{m}\right)_\mathrm{P} V_{CV} + \sum_{\text{faces}}^{\text{faces}} \left(\rho_{\mathrm{m;f}} \underline{\boldsymbol{u}}_{\mathrm{m;f}} \underline{\boldsymbol{u}}_{\mathrm{m;f}} \cdot \underline{\boldsymbol{n}}_\mathrm{f} A_\mathrm{f}\right) \\
&\quad = -V_{CV}\nabla p_\mathrm{m} + \rho_{\mathrm{m;P}}\underline{\boldsymbol{g}} + \sum_{\text{faces}} \mu_{\mathrm{eff,f}} \nabla \underline{\boldsymbol{u}}_\mathrm{m} \cdot \underline{\boldsymbol{n}}_\mathrm{f} A_\mathrm{f} \\
&\qquad - \sum_{\text{faces}} \mu_{\mathrm{eff,f}} \left(\nabla(\underline{\boldsymbol{u}}_\mathrm{m})^\mathrm{T} - \frac{2}{3}\underline{\underline{\boldsymbol{I}}}\nabla\cdot\underline{\boldsymbol{u}}_\mathrm{m}\right) A_\mathrm{f} \cdot \underline{\boldsymbol{n}}_\mathrm{f},
\end{aligned} \tag{5.5}$$

This can be discretized in time as follows

$$\begin{aligned}
&V_{CV}\rho^t_{\mathrm{m;P}} \frac{\underline{\boldsymbol{u}}^{t+\Delta t}_{\mathrm{m;P}} - \underline{\boldsymbol{u}}^{t+\Delta t}_{\mathrm{m;P}}}{\Delta t} + \sum_{\text{faces}}^{\text{faces}} \left(\rho^t_{\mathrm{m;f}} \underline{\boldsymbol{u}}^t_{\mathrm{m;f}} \underline{\boldsymbol{u}}^{t+\Delta t}_{\mathrm{m;f}} \cdot \underline{\boldsymbol{n}}_\mathrm{f} A_\mathrm{f}\right) \\
&\quad = -V_{CV}\nabla p^t_\mathrm{m} + \rho^t_{\mathrm{m;P}}\underline{\boldsymbol{g}} + \sum_{\text{faces}} \mu^t_{\mathrm{eff,f}} \nabla \underline{\boldsymbol{u}}^{t+\Delta t}_\mathrm{m} \cdot \underline{\boldsymbol{n}}_\mathrm{f} A_\mathrm{f} \\
&\qquad - \sum_{\text{faces}} \mu^t_{\mathrm{eff,f}} \left(\nabla(\underline{\boldsymbol{u}}^t_\mathrm{m})^\mathrm{T} - \frac{2}{3}\underline{\underline{\boldsymbol{I}}}\nabla\cdot\underline{\boldsymbol{u}}^t_\mathrm{m}\right) A_\mathrm{f} \cdot \underline{\boldsymbol{n}}_\mathrm{f},
\end{aligned} \tag{5.6}$$

where the superscript t indicates the variable at the current time, and the superscript $t + \Delta t$, the variable at the next time step. This introduces an error of $O(\Delta t)$, higher order schemes are also available in OpenFOAM. This equation is called the momentum predictor in OpenFOAM, and is optionally solved. When multiple iterations are used, variables denoted with superscript t, are replaced by the guess for $t + \Delta t$ from the latest iteration.

The discretized momentum balance can be rewritten to

$$a_{\mathrm{P}}\underline{\boldsymbol{u}}_{\mathrm{m;P}}^{t+\Delta t} = \sum_{\mathrm{nb}}^{\mathrm{neighbours}} a_{\mathrm{nb}}\underline{\boldsymbol{u}}_{\mathrm{nb}}^{t+\Delta t} + S(\underline{\boldsymbol{u}}_{\mathrm{m;P}}^{t}) + S^{t} - (\nabla p)_{\mathrm{P}}^{t}\,, \tag{5.7}$$

where $\underline{\boldsymbol{u}}_{\mathrm{m;P}}^{t+\Delta t}$ is the velocity at the centre of the cell under considerations at the next time step, a_{P}, is a coefficient which follows from the discretizations, $\underline{\boldsymbol{u}}_{\mathrm{m;nb}}$ is the cell averaged velocity of the neighbouring cell, a_{nb} is another discretization coefficient. $S(\underline{\boldsymbol{u}}_{\mathrm{m;P}}^{t})$ contains all the explicit terms of the discretized formula, and S contains all other source terms. $(\nabla p)_{\mathrm{P}}$, is the pressure gradient at the centre of the cell under consideration, and S is a container variable for all the terms not containing velocities at the next time step, or the pressure gradient.

To construct the pressure corrector, the pressure gradient in the left hand side, is replaced with the pressure gradient at the next time step, while all other terms on the left hand side are replaced with the guess from the latest iteration, denoted by superscript $*$.

$$a_{\mathrm{P}}\underline{\boldsymbol{u}}_{\mathrm{m;P}}^{t+\Delta t} = \sum_{\mathrm{nb}}^{\mathrm{neighbours}} a_{\mathrm{nb}}\underline{\boldsymbol{u}}_{\mathrm{nb}}^{*} + S(\underline{\boldsymbol{u}}_{\mathrm{m;P}}^{*}) + S^{*} - (\nabla p)_{\mathrm{P}}^{t+\Delta t}\,. \tag{5.8}$$

This is rewritten to

$$\underline{\boldsymbol{u}}_{\mathrm{m;P}}^{t+\Delta t} = \frac{H(u)}{a_{\mathrm{P}}} - \frac{1}{a_{\mathrm{P}}}\,(\nabla p)_{\mathrm{P}}^{t+\Delta t}\,, \tag{5.9}$$

where

$$H(u) = \sum_{\mathrm{nb}}^{\mathrm{neighbours}} a_{\mathrm{nb}}\underline{\boldsymbol{u}}_{\mathrm{nb}}^{*} + S(\underline{\boldsymbol{u}}_{\mathrm{m;P}}^{*}) + S^{*} \tag{5.10}$$

This can be interpolated to the face centre

$$\underline{\boldsymbol{u}}_{\mathrm{m;f}}^{t+\Delta t} = \left(\frac{H(u)}{a_{\mathrm{P}}}\right)_{\mathrm{f}} - \left(\frac{1}{a_{\mathrm{P}}}\right)_{\mathrm{f}} (\nabla p)_{\mathrm{f}}^{t+\Delta t}\,. \tag{5.11}$$

Combining this with Equation (5.4) gives the pressure correction equation:

$$\frac{\rho^*_{\mathrm{m;P}} - \rho^t_{\mathrm{m;P}}}{\Delta t} V_{CV} = \sum^{\text{faces}} \rho_{\mathrm{m;f}} A_{\mathrm{f}} \left(\frac{H(u)}{a_{\mathrm{P}}} \right)_{\mathrm{f}} \cdot \underline{\boldsymbol{n}}_{\mathrm{f}} - \sum^{\text{faces}} \rho_{\mathrm{m;f}} A_{\mathrm{f}} \left(\frac{1}{a_{\mathrm{P}}} \right)_{\mathrm{f}} (\nabla p)_{\mathrm{f}}^{t+\Delta t} \cdot \underline{\boldsymbol{n}}_{\mathrm{f}}. \tag{5.12}$$

The pressure is solved for with this equation in SettlingFOAM. After the pressure is updated, the mixture velocities are updated using Equation (5.11).

To avoid rounding errors, caused by subtracting two large and almost equal pressure values, a reference pressure is often subtracted from the total pressure. It is common to subtract reference density times $|\underline{\boldsymbol{g}}|h$, where h is the height in the direction opposite the gravity, from a given reference level. Instead, in SettlingFOAM a variable density, ρ_{m} is used. The total pressure term is then divided into a hydrostatic, and non-hydrostatic part

$$p = p' + \rho_{\mathrm{m}} |\underline{\boldsymbol{g}}| h, \tag{5.13}$$

The gradient becomes

$$\nabla p = \nabla p' + \rho_{\mathrm{m}} \underline{\boldsymbol{g}} + \underline{\boldsymbol{g}} \cdot h \nabla \rho_{\mathrm{m}}. \tag{5.14}$$

5.1.2 Solution procedure

Like many OpenFOAM solvers, the SettlingFOAM solvers uses the PIMPLE algorithm to solve the discretized equations. The PIMPLE algorithm is a combination of Patankar and Spalding's SIMPLE (Patankar and Spalding, 1972) and Issa's PISO (Issa et al., 1991).

The PIMPLE algorithm in SettlingFOAM (See Section 5.1.2) is as follows:

1. At the start of the algorithm, optionally the velocity field is updated using the discretized momentum balance (Section 5.1.1), using the current values of the pressure.

2. The concentration field is updated by solving for α with the discretized mass balance for the dispersed phase (Section 5.4).

3. The start of the pressure correction loop. The pressure is updated by solving for p', using the pressure correction equation (Section 5.1.1).

4. With the updated pressure, the velocity field is updated with Equation (5.11).

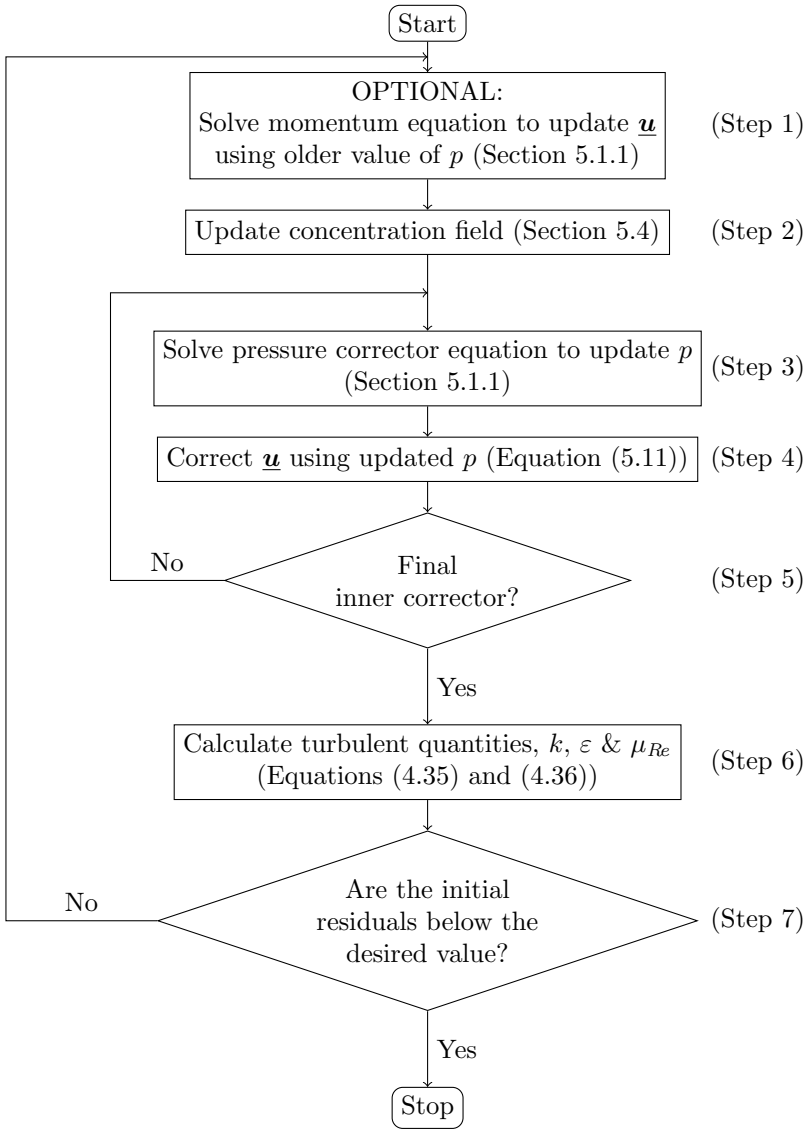

Figure 5.2: Flowchart of the PIMPLE solution procedure used in SettlingFOAM.

5. The pressure correction loop, Step 3 & 4, is repeated x number of times. Where x is determined by the user. When x is equal to 1, the PIMPLE algorithm is the same as the SIMPLE algorithm.

6. The turbulent quantities are updated, using the discretized versions of Equations (4.35) and (4.36).

7. The residuals of the pressure correction equation, and optionally the mixture momentum balance, are checked. If their residuals are larger than the desired minimal value, the algorithm is repeated. Otherwise, the calculation is complete.

5.2 Extension to granular media

To make the model suitable for simulating the breaching process, it is extended with the capability of modelling dense granular flows. The dense granular flow is modelled as a fluid with a yield stress. In granular materials this yield stress depends on the effective pressure, therefore the effective pressure is calculated as well. Finally, pore-pressure feedback plays an important role, and is implemented as well.

The goal is to model both the dense granular flow, as well as more dilute sand-water mixtures in the same domain. Therefore, the interface between these two regimes is modelled. At this interface the erosion by flow, and sedimentation to the bed need to be modelled correctly, and the turbulence near the interface needs to be handled correctly. Finally, the interpolation of variables to this interface requires special care.

5.2.1 Effective viscosity

As described in Chapter 4, granular media is modelled as a fluid with a yield stress. This is implemented in the model via Equation (4.58), which calculates an effective viscosity as

$$\mu_{\text{eff}} = \frac{\tau_{\text{y}}}{\dot{\gamma}} + \mu_m, \tag{5.15}$$

where τ_{y} is the yield stress, and $\dot{\gamma}$ is the second invariant of the shear rate (Equation (4.48)). τ_{y} is calculated using $\mu(I)$-rheology (Equation (4.57)) combined with the viscous inertial number, I_v (Equation (4.60)).

It is clear division by zero errors arise when using Equation (5.15) when the second invariant of the shear rate, $\dot{\gamma}$, goes to zero.

Regularization is used to avoid this problem. When using regularization the viscosity converges to a large finite value, instead of infinity. When using a regularized effective viscosity, the unyielded region thus becomes region of high viscosity instead, whose viscosity depends on a regularization parameter ϵ.

The simplest regularization (e.g. Allouche et al. (2000)) simply adds a small parameter, ϵ, giving.

$$\mu_{\text{eff}} = \frac{\tau_y}{\dot{\gamma} + \epsilon} + \mu_{\text{m}}. \tag{5.16}$$

Another regularization proposed by Bercovier and Engelman (1980) is

$$\mu_{\text{eff}} = \frac{\tau_y}{\sqrt{\dot{\gamma}^2 + \epsilon^2}} + \mu_m. \tag{5.17}$$

Yet another alternative was proposed by Papanastasiou (1987):

$$\mu_{\text{eff}} = \frac{\tau_y}{\dot{\gamma}} \left(1 - \exp\left(-\frac{\dot{\gamma}}{\epsilon}\right)\right) + \mu_m. \tag{5.18}$$

This last regularization retains division by zero when the shear rate is zero. However, the term between brackets will also be equal to zero, thus the viscosity reduces to μ_{m}, but special care might be required to avoid numerical division by zero problems.

Finally, a bi-viscosity model can be applied (O'Donovan and Tanner, 1984). In the bi-viscosity model, the effective viscosity is set to a user defined high value, $\mu_{\text{eff};0}$, when the second invariant of the shear rate is below a given value, $\dot{\gamma}_{\text{min}}$

$$\mu_{\text{eff}} = \begin{cases} \mu_{\text{eff};0}, & \text{if } \dot{\gamma} < \dot{\gamma}_{\text{min}} \\ \frac{\tau_{\text{y}}}{\dot{\gamma}} + \mu_{\text{m}}, & \text{if } \dot{\gamma} \geq \dot{\gamma}_{\text{min}} \end{cases} \tag{5.19}$$

When comparing viscosity, and shear stress, to those of Bingham model (Figure 5.3), It can be seen that for similar regularization parameters, the simple regularization shows the largest errors. The equations of Bercovier and Engelman (1980) and Papanastasiou (1987) show very similar errors, and the bi-viscosity model has the smallest errors, but does not have a smooth viscosity or shear stress function. Burgos et al. (1999) compare yield surfaces recovered using the regularization of Papanastasiou (1987), and the bi-viscosity model. They find that the method of Papanastasiou (1987), for small enough regularization parameters, recovers the correct yield surface, while the bi-viscosity

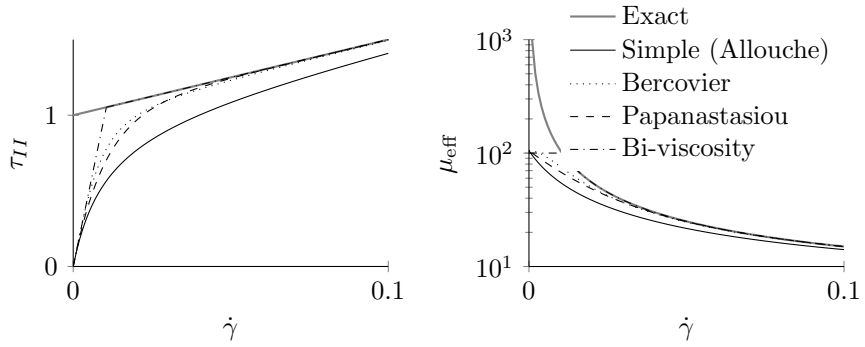

Figure 5.3: The resulting relation between shear rate, shear stress (left), and effective viscosity (right) when using different regularization methods, compared to the exact result.

model can recover concave yield surfaces, where convex yields surfaces are expected. Burgos et al. (1999) claim that the method of Bercovier and Engelman (1980) behaves similarly to that of Papanastasiou (1987), although no proof is shown. Both the methods of Papanastasiou (1987) and Bercovier and Engelman (1980) seem suitable for the problem at hand. Here, the method of Bercovier and Engelman (1980) is chosen because it is slightly easier to implement.

To increase the stability of the simulations further, the viscosity is limited by a maximum viscosity, $\mu_{\max}$ (This has the same effect as limiting the yield stress, τ_y). The final effective viscosity equation is then

$$\mu_{\text{eff}} = \min\left(\frac{\tau_y}{\sqrt{\dot{\gamma}^2 + \epsilon^2}} + \mu_{\text{m}}, \mu_{\max}\right) \tag{5.20}$$

5.2.2 Effective particle pressure

Closure of the effective particle pressure, p_{eff}, is necessary, as it is an important variable for determining the inertial number, I, and the effective viscosity μ_{eff} (Equations (4.55) to (4.62)). For flow of granular material in air, the effect of the continuum phase can be neglected (as in e.g. Jop et al. (2006)). In this case single phase equations can be used, and the particle pressure follows directly from solving the equations. However, this work deals with flow of granular materials in water, and the continuum phase is not negligible. In the applied

mixture approach, only the mixture pressure, p_{m}, follows from the governing equations, and extra closure is needed to determine the effective pressure.

From Equation (4.14) it follows that the gradient in effective pressure is,

$$\nabla p_{\mathrm{eff}} = \nabla p_{\mathrm{m}} - \nabla p_{\mathrm{c}} \tag{5.21}$$

∇p_{m} is known, while the continuum phase pressure gradient, ∇p_{c}, follows from the continuum phase momentum balance Equation (4.13),

$$\begin{aligned}\alpha_{\mathrm{c}} \nabla p_{\mathrm{c}} = &- \frac{\partial \alpha_{\mathrm{c}} \rho_{\mathrm{c}} \underline{\boldsymbol{u}}_{\mathrm{c}}}{\partial t} + \nabla \cdot \alpha_{\mathrm{c}} \rho_{\mathrm{c}} \underline{\boldsymbol{u}}_{\mathrm{c}} \underline{\boldsymbol{u}}_{\mathrm{c}} + \nabla \cdot \left(\alpha_{\mathrm{c}} \left(\underline{\underline{\boldsymbol{\tau}}}_{\mathrm{c}} + \underline{\underline{\boldsymbol{\tau}}}_{\mathrm{c}}^{Re} \right) \right) \\ &+ \alpha_{\mathrm{c}} \rho_{\mathrm{c}} \underline{\boldsymbol{g}} + \underline{\boldsymbol{M}}_{\mathrm{c}} - p_{\mathrm{c}} \nabla \alpha_{\mathrm{c}},\end{aligned} \tag{5.22}$$

where $\underline{\boldsymbol{u}}_{\mathrm{c}}$ can be written in terms of known variables

$$\underline{\boldsymbol{u}}_{\mathrm{c}} = \underline{\boldsymbol{u}}_{\mathrm{m}} + \frac{\alpha_{\mathrm{c}} \rho_{\mathrm{d}}}{\alpha_{\mathrm{d}} \rho_{\mathrm{m}}} \underline{\boldsymbol{v}}_{dj} \tag{5.23}$$

The dispersed phase stress is assumed to be zero when the concentration is below a limiting value, and is assumed hydrostatic at the boundaries.

To solve Equation (5.22) for ∇p_{c}, closures for $\nabla \cdot \left(\alpha_{\mathrm{c}} \left(\underline{\underline{\boldsymbol{\tau}}}_{\mathrm{c}} + \underline{\underline{\boldsymbol{\tau}}}_{\mathrm{c}}^{Re} \right) \right)$, $\underline{\boldsymbol{M}}_{\mathrm{c}}$, and $p_{\mathrm{c}} \nabla \alpha_{\mathrm{c}}$ are required.

The interaction force, $\underline{\boldsymbol{M}}_{\mathrm{c}}$ is approximated using the Darcy equations. The Darcy equations are valid for pore Reynolds numbers smaller than 10 (Zeng and Grigg, 2006). This Reynolds number is defined as

$$Re_{\mathrm{pore}} = \frac{\rho D |\underline{\boldsymbol{u}}_r|}{\mu} \frac{1}{\alpha_{\mathrm{d}}}, \tag{5.24}$$

where D is the particle diameter, and $\underline{\boldsymbol{u}}_r$ is the velocity of the continuum phase, relative to the dispersed phase: $(\underline{\boldsymbol{u}}_{\mathrm{c}} - \underline{\boldsymbol{u}}_{\mathrm{d}})$.

It is assumed that the only source for pore water flow, is the dilation, pore water flows forced by gradients in water pressure are thus not modelled. In this case the interaction force is equal to the pore pressure gradient

$$\underline{\boldsymbol{M}}_{\mathrm{c}} = \alpha \nabla p_e \tag{5.25}$$

In this case no turbulence is expected, thus the term $\underline{\underline{\boldsymbol{\tau}}}_{\mathrm{c}}^{Re}$ is neglected. This leaves the term $\underline{\underline{\boldsymbol{\tau}}}_{\mathrm{c}}$ which is approximated as

$$\nabla \cdot \alpha_{\mathrm{c}} \underline{\underline{\boldsymbol{\tau}}}_{\mathrm{c}} = \nabla \cdot \left(\mu_{\mathrm{c}} \left(\nabla \underline{\boldsymbol{u}}_{\mathrm{c}} + \left(\nabla \underline{\boldsymbol{u}}_{\mathrm{c}} - \frac{2}{3} \underline{\underline{\boldsymbol{I}}} \nabla \cdot \underline{\boldsymbol{u}}_{\mathrm{c}} \right)^{\mathrm{T}} \right) \right). \tag{5.26}$$

The gradient of the effective pressure can now be estimated with

$$\begin{aligned}\nabla p^{*}_{\text{eff}} = \nabla p_{\text{m}} + \frac{1}{\alpha_{\text{c}}}\Bigg(&\frac{\partial \alpha_{\text{c}}\rho_{\text{c}}\underline{\boldsymbol{u}}_{\text{c}}}{\partial t} - \nabla\cdot\,\alpha_{\text{c}}\rho_{\text{c}}\underline{\boldsymbol{u}}_{\text{c}}\underline{\boldsymbol{u}}_{\text{c}} \\ &- \nabla\cdot\left[\mu_{\text{c}}\left(\nabla\underline{\boldsymbol{u}}_{\text{c}} + \left(\nabla\underline{\boldsymbol{u}}_{\text{c}} - \frac{2}{3}\underline{\underline{\boldsymbol{I}}}\nabla\cdot\,\underline{\boldsymbol{u}}_{\text{c}}\right)^{\text{T}}\right)\right]\Bigg) - \rho_{\text{c}}\underline{\boldsymbol{g}} - \nabla p_{e},\end{aligned} \tag{5.27}$$

where $\nabla p^{*}_{\text{eff}}$ is the estimated gradient of the effective particle pressure.

The calculation of the continuum phase pressure can be simplified by considering only the hydrostatic continuum phase pressure and the simplified interaction term. This simplifies Equation (5.21) to

$$\nabla p^{\text{hc}}_{\text{eff}} = \nabla p_{m} - \rho_{c}\underline{\boldsymbol{g}} - \nabla p_{e}. \tag{5.28}$$

The difference between this simplified effective pressure, $p^{\text{hc}}_{\text{eff}}$, and the actual effective pressure gradient is

$$\begin{aligned}\nabla p^{\text{hc}}_{\text{eff}} - \nabla p_{\text{eff}} &= \nabla p_{\text{c}} - \rho_{\text{c}}\underline{\boldsymbol{g}} - \nabla p_{e} \\ &= \frac{1}{\alpha_{\text{c}}}\Bigg(-\frac{\partial \alpha_{\text{c}}\rho_{\text{c}}\underline{\boldsymbol{u}}_{\text{c}}}{\partial t} + \nabla\cdot\,\alpha_{\text{c}}\rho_{\text{c}}\underline{\boldsymbol{u}}_{\text{c}}\underline{\boldsymbol{u}}_{\text{c}} \\ &\quad + \nabla\cdot\left(\alpha_{\text{c}}\left(\underline{\underline{\boldsymbol{\tau}}}_{\text{c}} + \underline{\underline{\boldsymbol{\tau}}}^{Re}_{\text{c}}\right)\right) - p_{\text{c}}\nabla\alpha_{\text{c}}\Bigg).\end{aligned} \tag{5.29}$$

For small velocities and accelerations, the error caused by this simplification are small as well.

A further simplification is made by assuming the dispersed phase pressure to be hydrostatic. This gives

$$\nabla p^{\text{hd}}_{\text{eff}} = \alpha_{d}\left(\rho_{d} - \rho_{c}\right)\underline{\boldsymbol{g}}. \tag{5.30}$$

The difference between the hydrostatic pressure and the actual pressure gradient is

$$\nabla p^{\text{hd}}_{\text{eff}} - \nabla p_{\text{eff}} = \left(\nabla p_{\text{c}} - \rho_{\text{c}}\underline{\boldsymbol{g}} - \nabla p_{e}\right) - \left(\nabla p_{\text{m}} - \rho_{\text{m}}\underline{\boldsymbol{g}}\right). \tag{5.31}$$

The first term on the right hand side is equal to the difference found in Section 5.2.2, the second term is equal to

$$\nabla p_{\text{m}} - \rho_{\text{m}}\underline{\boldsymbol{g}} = -\frac{\partial}{\partial t}\rho_{\text{m}}\underline{\boldsymbol{u}}_{\text{m}} - \nabla\cdot\left(\rho_{\text{m}}\underline{\boldsymbol{u}}_{\text{m}}\otimes\underline{\boldsymbol{u}}_{\text{m}}\right) + \nabla\cdot\left(\underline{\underline{\boldsymbol{\tau}}}_{\text{m}} + \underline{\underline{\boldsymbol{\tau}}}^{Re}_{\text{m}} + \underline{\underline{\boldsymbol{\tau}}}^{\text{D}}_{\text{m}}\right). \tag{5.32}$$

Even in slowly flowing and accelerating granular material a large error is introduced via the viscous shear stress, $\underline{\underline{\boldsymbol{\tau}}}_{\text{m}}$ (See Equation (4.52)), as in quasistatic regions the effective viscosity, μ_{eff}, becomes large. This can cause large shear stresses even when the velocity gradients might seem negligible.

Implementation

Once the pressure gradient has been determined, the effective pressure is solved for with a Laplace equation

$$\nabla^2 p_{\text{eff}} = \nabla \cdot \nabla p^*_{\text{eff}}, \tag{5.33}$$

where ∇p^*_{eff} is the estimated pressure gradient. In all cells which are not labeled as soil, and thus should have an effective pressure of 0, the effective pressure is manually set to 0. This is done in OpenFOAM by first setting the value in the cell to 0, as well as the source term for this cell.

At the domain boundaries, a hydrostatic effective pressure is assumed

$$\nabla p^*_{\text{eff}} = \alpha_{\text{d}} \left(\rho_{\text{d}} - \rho_{\text{c}}\right) \underline{\boldsymbol{g}} \cdot \underline{\boldsymbol{n}}_{\text{fb}}, \tag{5.34}$$

where $\underline{\boldsymbol{n}}_{\text{fb}}$ is the unit vector perpendicular to the boundary face.

Comparison

	Equation
Full equation	$\nabla p^{\text{full}}_{\text{eff}} = \nabla p_{\text{m}} - \nabla p_c$
Hydrostatic p_{c}, minus interaction term	$\nabla p^{\text{hc}}_{\text{eff}} = \nabla p_m - \rho_c \underline{\boldsymbol{g}} - \nabla p_e$
Hydrostatic p_{eff}, minus interaction term	$\nabla p^{\text{hd}}_{\text{eff}} = \alpha_d \left(\rho_d - \rho_c\right) \underline{\boldsymbol{g}} - \nabla p_e.$

Table 5.1: Overview of different methods to calculate the effective pressure gradient

Three different methods were proposed (Table 5.1). The three methods are compared in a simulation of a column collapse, where both shear stress and acceleration are not negligible. This simple simulation starts with a rectangular block of sand inside a domain filled with water, as in Figure 5.4. We run the simulation for a short period of time, 0.01 seconds, and compare the calculated effective pressures.

The size of the sand column is $2\,\text{m} \times 1\,\text{m}$. The total domain is $2.125\,\text{m} \times 4\,\text{m}$, with grid cells of $31.25\,\text{mm} \times 31.25\,\text{mm}$, and a time step of $0.001\,\text{s}$. The sand has a density of $2650\,\text{kg}\,\text{m}^{-3}$, with a internal friction angle of $0.6\,\text{rad}$.

As expected, when using the hydrostatic effective pressure, there is a linear increase in effective pressure along the y-axis, while the pressure is constant in the x-direction (Figure 5.5a). This approach leads to large, unrealistic, gradients in effective pressure along the vertical edge of the column.

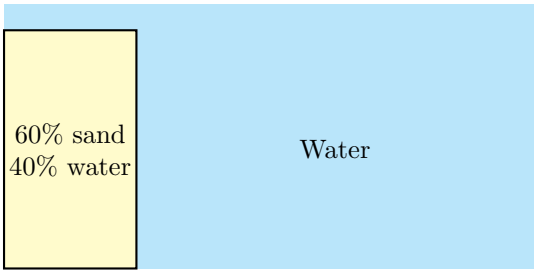

Figure 5.4: The set-up of the domain for the comparison of the effictive pressures

Using the full equations, or assuming the continuum phase pressure to be hydrostatic, results in more realistic pressure distributions (Figure 5.5b & c), with an effective pressure approaching zero near the soil water interface. Overall, these approaches lead to a lower pressure over the whole domain. When assuming hydrostatic pressure, we see a drop in pressure near the left boundary. This drop is not present when using the full equations. The difference between these two approaches is most likely caused by the effect of acceleration (The time derivative in Section 5.2.2).

5.2.3 Flux limiting

To avoid unrealistically high concentrations, which can also cause numerical instability, the drift-flux is limited using the approach of Zalesak (1979). The algorithm is as follows:

1. For each cell, calculate the sum of all inflowing fluxes:

$$P^+ = \sum^{\text{faces}} \max\left(\frac{1}{V_{\text{cell}}}\phi_{vdj}\Delta t, 0\right), \tag{5.35}$$

   where ϕ_{vdj} is the flux due to drift-flux, and is positive for inflowing flux, and negative for outflowing flux.

2. Determine current concentration, plus the added concentration due to inflowing fluxes.

$$Q^+ = \alpha_{\text{d}} + P^+ \tag{5.36}$$

   where α_{d} is the current concentration.

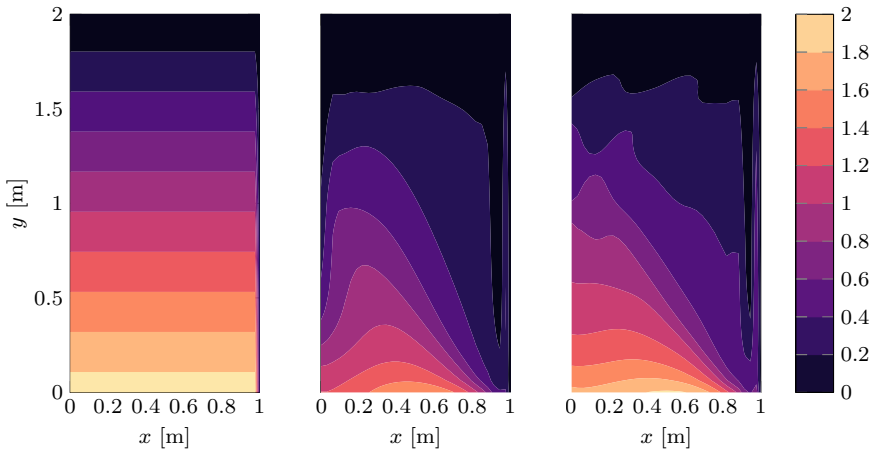

a) Hydrostatic p_{eff} b) Hydrostatic p_{c} c) Full equation

Figure 5.5: Effective pressure scaled by weight of sand ($p_{\text{eff}}/(\alpha(\rho_d - \rho_c)g)$) in meters. Only the stress inside the sand column is shown here.

3. If this concentration exceeds the maximum concentration, a limiting factor, λ^+, is calculated as

$$\lambda^+ = \frac{\alpha_{\max} - \alpha_{\text{d}}}{P^+}, \tag{5.37}$$

where $\alpha_{\max}$ is the maximum allowed concentration. If Q^+ does not exceed $\alpha_{\max}$, λ^+ is equal to 1 (no limiting).

In a similar fashion the flux is limited to avoid the concentration dropping below 0, leading to a factor λ^-. Then the flux is limited as follows:

$$\phi_{vdj} = \phi_{vdj} \min\left(\lambda^+, \lambda^-\right) \tag{5.38}$$

5.2.4 Dilatancy Modelling

The modelling of dilatancy effects is done in three steps. First the change in concentration is determined. Secondly, this change of concentration is used as a source term to calculate the resulting pore pressure. Finally, this calculated pore pressure is used to update the drift flux, to include pore water flow.

To determine the change in concentration, first the equilibrium concentration is estimated using the formula proposed by Boyer et al. (2011) (Equation (2.10)). This equilibrium concentration is combined with the linearisation proposed by Pailha and Pouliquen (2009) (Equation (2.15)) to arrive at the dilatancy angle. Finally this dilatancy angle is multiplied with the second invariant of the shear rate to estimate the change in concentration:

$$\Delta\alpha_{\mathrm{d}} = C_{\mathrm{dil}} \left(\alpha_d - \frac{\alpha_{\mathrm{eq;0}}}{1 + \sqrt{I_v}} \right) \dot{\gamma}. \tag{5.39}$$

Material properties C_{dil}, and $\alpha_{\mathrm{eq;0}}$ have to be set by the user.

Once the change in concentration has been calculated, it serves as the source term for the calculation of the pore pressure. The pore pressure is calculated using the equation of Iverson (2013) (Equation (4.69)):

$$\nabla \cdot \frac{k}{\rho_{\mathrm{c}} |\underline{\boldsymbol{g}}|} \nabla p_e = C \frac{\mathrm{D}p_{\mathrm{eff}}}{\mathrm{D}t} + \Delta\alpha_{\mathrm{d}} \tag{5.40}$$

Appropriate boundary conditions are required to solve this equation. At fixed walls, where there is no pore water flow, the gradient of the pore pressure should be zero. Furthermore, the excess pore pressure is assumed to only exist inside the soil, therefore the excess pore pressure is fixed to zero in cells not labeled as soil, similar to the calculation of p_{eff}. The permeability, k, in the equation is determined using the Kozeny-Carman equation (Carman, 1937)

$$k = \rho_{\mathrm{c}} |\underline{\boldsymbol{g}}| D_{15}^2 c_{\mathrm{shape}} \frac{(1 - \alpha_{\mathrm{d}})^3}{\alpha_{\mathrm{d}}^2} \tag{5.41}$$

The shape factor, c_{shape}, is usually in the order of 0.001, and can be used by the user to tune the permeability. Harmonic interpolation is used to interpolate the permeability to the cell faces, at locations with large gradients in permeability, like at the soil-water interface, this gives interpolated values closer to the lower values.

Finally, when the underpressure has been calculated, the drift flux is updated to include the pore water flow. Without this update, there would be no change in concentration due to dilation observed in the model. The pore water flow is calculated using the Darcy equation (Equation (4.68)). The drift flux due to dilation, $\underline{\boldsymbol{v}}_{dj}^{\mathrm{Darcy}}$ is then (see also Equation (4.68)):

$$\underline{\boldsymbol{v}}_{dj}^{\mathrm{Darcy}} = (1 - \alpha_{\mathrm{d}}) \left(\underline{\boldsymbol{u}}_{\mathrm{d}} - \underline{\boldsymbol{u}}_{\mathrm{c}} \right) = - \frac{k}{\rho_{\mathrm{c}} |\underline{\boldsymbol{g}}|} \nabla p_e, \tag{5.42}$$

5.3 Interface modelling

To accurately model erosion and sedimentation at the soil-water interface, small grid cells, in the order of a grain diameter, are required. Because the model is applied to large scale phenomena, using grid cells of this size is not feasible. Instead, erosion at the soil-water interface is parametrized. To do this, the location of this interface needs to be known. This is done by first determining which cells are considered soil, and which are considered sand-water mixture.

Whether a cell belongs to the soil, is determined by its dispersed phase concentration, α_d. If in a cell this concentration exceeds a given concentration α_soil, it is considered soil. For stability, the change from non-soil to soil occurs at a higher concentration than the change from soil to non-soil. The interface is the collection of cell faces, which have a soil cell on one side, and a non-soil cell on the other side.

Handling of the soil-water interface is important. In the finite volume approach of OpenFOAM, several variables are interpolated from the cell centres to the cell faces. Especially at the interface between soil and water this has to be done carefully, as large gradients in variables can occur. This is most noticable when discretizing the Laplacian part of the shear stress term (Equation (4.52)):

$$\iiint_{CV} \nabla\cdot \mu_\mathrm{eff} \nabla \underline{\boldsymbol{u}} \mathrm{d}V = \sum_\mathrm{faces} \mu_\mathrm{eff,f} \frac{\underline{\boldsymbol{u}}_\mathrm{cell1} - \underline{\boldsymbol{u}}_\mathrm{cell2}}{\Delta \underline{\boldsymbol{X}}} A_\mathrm{f} \cdot \underline{\boldsymbol{n}}_\mathrm{f}, \tag{5.43}$$

where $\mu_\mathrm{eff,face}$ is the effective viscosity interpolated to the face, the subscripts, cell1 and cell2, indicate the centres of the two cells neighbouring the face, $\Delta \underline{\boldsymbol{X}}$ is the distance between the two cell centres.

There are several methods to interpolate the effective viscosity. The most straight-forward way to interpolate the viscosity to the cell faces, is a simple linear interpolation. The downside of this approach is that it leads to relatively high viscosities at the soil-water interface. Using Equation (5.17), the viscosity in unyielded soil is of order $O\left(\frac{1}{\epsilon}\right)$, while the viscosity of water is around $O\left(1 \times 10^{-3}\right)$. When using a linear interpolation, the viscosity at the interface is of the same order of magnitude as in the soil. This viscosity will likely dominate the Laplacian term in this cell (See Equation (5.43)). This viscosity has a strong influence on the turbulent properties of the flow past it, and the behaviour of the soil.

To improve the calculation of turbulent properties of flows along the interface, the viscosity at the interface can be determined by applying the law of the

wall (Kármán, 1930). Then, the viscosity is determined based on flow properties of the cell on the water side of the interface. With this method the flow near the wall and its turbulent properties are more in line with experiments. To correctly model the turbulent properties near the wall, proper boundary conditions for turbulent kinetic energy, k_t, and turbulent dissipation, ε, need to be set as well.

Another issue arises when the actual soil-water interface does not align with the numerical grid. When this occurs, in cells which contain the actual interface, the numerical concentration will be a mixture of the concentrations of the soil, and that of the sand-water mixture next to it (Figure 5.6). The numerical soil-water interface will be located on the nearest face, and sand which is part of the soil will be seen as sand-water mixture. This leads to a much lower viscosity, and this sand is easily transported by the flow.

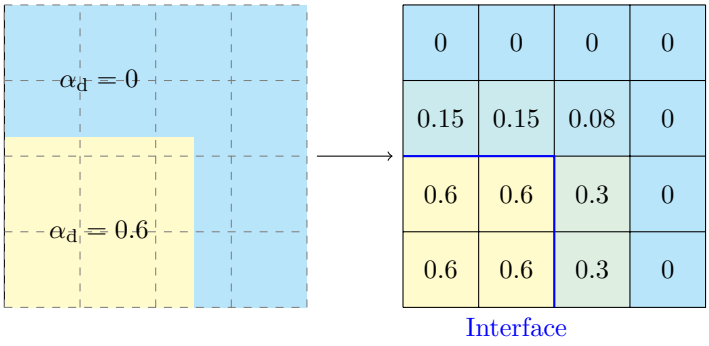

Figure 5.6: The differences between the actual numerical interface, and concentrations.

A buffer layer is introduced, creating a second, artificial interface (Figure 5.7). All non-soil cells adjacent to the interface, are labelled as buffer cells, and an artificial interface is determined between buffer cells and non-soil cells. Linear interpolation is used at the real interface, while a viscosity based on the law of the wall is applied at the artificial interface. The linear interpolation at the real interface, leads to high viscosities at the interface, causing the cells in the buffer layer to 'stick' to the interface, while the use of the law of the wall at the artificial interface leads to better prediction of turbulent properties.

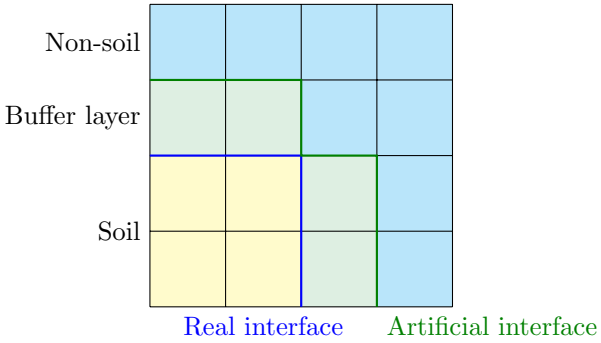

Figure 5.7: The interfaces as applied in the model

5.3.1 Erosion modelling

Pick-up of sediment is modelled by calculating a pick-up-flux, E, based on the flow properties near the interface, and adding it as diffusion to the dispersed phase mass balance equation (Equation (4.28)). The diffusion coefficient, C_{E}, is calculated using the pick-up flux, E, calculated with Equation (2.59), as follows:

$$C_{\mathrm{E}} = E \frac{\rho_{\mathrm{m}}^2}{\rho_{\mathrm{d}} \rho_{\mathrm{c}}} \frac{\Delta x}{\alpha_{\mathrm{soil}}} f_\alpha, \tag{5.44}$$

where f_α is a reduction factor, to adjust for the fact that a cell is considered fully eroded (i.e. not considered part of the soil) not when the concentration becomes 0, but when it drops below a value set by the user, α_{soil}.

$$f_\alpha = r_S + (1 - r_S) \frac{\alpha_- \alpha_{\mathrm{soil}}}{\alpha_{\mathrm{max}}}, \tag{5.45}$$

where r_S is the ratio of the sedimentation flux, S, and the erosion flux, E, limited between 1 and 0. Thus when the sedimentation flux exceeds the erosion flux, this correction factor becomes 1, and erosion flux is not reduced. α_{max}, is the maximum concentration of the cell while it is subject to erosion.

E is calculated according to Equation (2.59), but can easily be replaced by any formula. The Shields parameter, θ, is calculated at the artificial interface, while other variables are determined at the real interface (Figure 5.7). When a buffer cell is adjacent to multiple faces belonging to the artificial interface, the maximum Shields parameter at these faces is used.

The following diffusion term is added to Equation (4.28):

$$\nabla\cdot C_{\mathrm{E}}\nabla\frac{\rho_{\mathrm{d}}\alpha}{\rho_{\mathrm{m}}}. \tag{5.46}$$

Using diffusion to model the erosion 1) improves stability of the simulation, and 2) introduces the concept of hindered erosion (Section 2.4.2) in a natural way. When the flow past the interface consists of pure water, the erosion following from the diffusion method, is similar to the calculated flux, E. However, as the concentration of sand in the flow increases, the erosion rate reduces.

5.3.2 Wall functions

The wall shear stress at a boundary, or at the artificial soil-water interface, is defined as

$$\tau_\tau = (\mu_{\mathrm{c}} + \mu_{Re})\,\frac{\partial u}{\partial y}, \tag{5.47}$$

where y is the coordinate perpendicular to the wall or interface, and u is the velocity parallel to the wall or interface, In OpenFOAM, for cells adjacent to a no-slip boundary, this is discretized to

$$\tau_\tau = (\mu_{\mathrm{c}} + \mu_{Re})\,\frac{u}{\Delta y_\tau}, \tag{5.48}$$

where Δy_τ is the shortest distance between the boundary and the cell centre.

To make sure the calculated shear stress is in accordance with Equation (5.47), μ_{Re} has to be chosen accordingly. Using the law of the wall (Equation (4.43)), τ_τ, can be rewritten as

$$\tau_\tau = \rho_{\mathrm{c}} u_*^2 = \frac{\rho_{\mathrm{c}} u u_* \kappa}{\ln(Ey^+)}. \tag{5.49}$$

Combining this with Equation (5.47) gives for the turbulent viscosity at the no-slip boundary:

$$\mu_{Re;\tau} = \frac{\mu_{\mathrm{c}}\kappa y^+}{\ln(Ey^+)} - \mu_{\mathrm{c}}, \tag{5.50}$$

where y^+ is calculated as:

$$y^+ = \frac{\Delta y_\tau u_*}{\nu_{\mathrm{c}}}, \tag{5.51}$$

and u_* is estimated with the relation

$$u_* = C_\mu^{0.25}\sqrt{k_{\mathrm{t}}}. \tag{5.52}$$

Because the law of the wall is used to arrive at this turbulent viscosity, the formulation is only valid for $y^+ \geq 30$ where the law of the wall applies.

Boundary conditions for ϵ follow from the assumption that the turbulent production P and the dissipation $\rho\epsilon$ are equal. Close to the wall, if the velocity perpendicular to the wall is zero, the production term is

$$P = (\mu_\mathrm{c} + \mu_{Re}) \frac{\partial u}{\partial y} \frac{\partial u}{\partial y} = \tau_\tau \frac{\partial u}{\partial y} = \rho_\mathrm{c} u_*^2 \frac{\partial u}{\partial y} = \rho_\mathrm{c} \epsilon, \tag{5.53}$$

using the law of the wall (Equation (4.43)) gives:

$$\frac{\partial u}{\partial y} = \frac{u_*}{\kappa y}, \tag{5.54}$$

which gives:

$$\epsilon = \frac{u_*^3}{\kappa y}. \tag{5.55}$$

In OpenFOAM, instead of fixing the turbulent velocity, k_t, the production of turbulent velocity is set near the boundary. The production, P, in the cell adjacent to the boundary or interface is modelled as

$$P = (\mu_\mathrm{c} + \mu_{Re}) \frac{\partial u}{\partial y} \frac{\partial u}{\partial y} = (\mu_\mathrm{c} + \mu_{Re}) \frac{u}{\Delta y_\tau} \frac{u_*}{\kappa y} = (\mu_\mathrm{c} + \mu_{Re}) \frac{u}{\Delta y_\tau} \frac{k_\mathrm{t}^{0.5} C_\mu^{0.25}}{\kappa y} \tag{5.56}$$

5.4 Adapted advection equation

The dispersed phase continuity equation (Equation (4.28)) is solved to update the concentration field:

$$\frac{\partial}{\partial t} (\alpha_\mathrm{d} \rho_\mathrm{d}) + \nabla \cdot (\alpha_\mathrm{d} \rho_\mathrm{d} \underline{\boldsymbol{u}}_\mathrm{m}) = - \nabla \cdot \left(\alpha_\mathrm{d} \frac{\rho_\mathrm{c} \rho_\mathrm{d}}{\rho_\mathrm{m}} \underline{\boldsymbol{v}}_{dj} \right), \tag{5.57}$$

where the drift-flux, $\underline{\boldsymbol{v}}_{dj}$, can be separated into several components: drift-flux due to settling, $\underline{\boldsymbol{v}}_{dj}^{\mathrm{settle}}$, drift-flux due to turbulent diffusion, $\underline{\boldsymbol{v}}_{dj}^{\mathrm{diff}}$, drift-flux due to pick-up of sediment, $\underline{\boldsymbol{v}}_{dj}^{\mathrm{ero}}$, and drift-flux due to pore water flow, $\underline{\boldsymbol{v}}_{dj}^{\mathrm{Darcy}}$. These drift-flux can be divided into diffusion fluxes and other fluxes. In this approach, besides the drift-flux due to turbulent diffusion, the erosion flux (Section 2.4) is modelled as a diffusion as well.

The updated formula becomes:

$$\frac{\partial}{\partial t}\left(\alpha_{\mathrm{d}}\rho_{\mathrm{d}}\right)+\nabla\cdot\left(\alpha_{\mathrm{d}}\rho_{\mathrm{d}}\underline{\boldsymbol{u}}_{\mathrm{m}}\right)=-\nabla\cdot\left(\alpha_{\mathrm{d}}\frac{\rho_{\mathrm{c}}\rho_{\mathrm{d}}}{\rho_{\mathrm{m}}}\underline{\boldsymbol{v}}_{dj}^{*}\right)+\nabla\cdot\left(\mu_t\beta+C_{\mathrm{E}}\right)\nabla\frac{\rho_{\mathrm{d}}\alpha_{\mathrm{d}}}{\rho_{\mathrm{m}}}, \tag{5.58}$$

where $\underline{\boldsymbol{v}}_{dj}^{*}=\underline{\boldsymbol{v}}_{dj}^{\mathrm{settle}}+\underline{\boldsymbol{v}}_{dj}^{\mathrm{Darcy}}$.

Using the Gauss theorem this can be rewritten to:

$$\begin{aligned}&\frac{\partial}{\partial t}\left(\alpha_{\mathrm{d}}\rho_{\mathrm{d}}\right)_{\mathrm{P}}V_{CV}+\sum^{\mathrm{faces}}\left(\alpha_{\mathrm{d;f}}\rho_{\mathrm{d}}\underline{\boldsymbol{u}}_{\mathrm{m;f}}\cdot\underline{\boldsymbol{n}}_{\mathrm{f}}A_{\mathrm{f}}\right)\\&=-\sum^{\mathrm{faces}}\left(\alpha_{\mathrm{d;f}}\frac{\rho_{\mathrm{c}}}{\rho_{\mathrm{m;f}}}\underline{\boldsymbol{v}}_{dj;\mathrm{f}}^{*}\cdot\underline{\boldsymbol{n}}_{\mathrm{f}}A_{\mathrm{f}}\right),+\sum^{\mathrm{faces}}\left(\left(\beta\mu_t+C_{\mathrm{E}}\right)\nabla\frac{\alpha_{\mathrm{d;f}}}{\rho_{\mathrm{m}}}\cdot\underline{\boldsymbol{n}}_{\mathrm{f}}A_{\mathrm{f}}\right).\end{aligned} \tag{5.59}$$

Discretizing this in time gives:

$$\alpha_{\mathrm{d}}^{t+\Delta t}=\alpha_{\mathrm{d}}t+\frac{\Delta t}{V_{CV}}\left(U(\alpha_{\mathrm{d}}^{t+\Delta t})+D(\alpha_{\mathrm{d}}^{t+\Delta t})\right), \tag{5.60}$$

where

$$U(\alpha_{\mathrm{d}}^{t+\Delta t})=-\sum^{\mathrm{faces}}\left(\alpha_{\mathrm{d;f}}^{t+\Delta t}\rho_{\mathrm{d}}\underline{\boldsymbol{u}}_{\mathrm{m;f}}\cdot\underline{\boldsymbol{n}}_{\mathrm{f}}A_{\mathrm{f}}\right)-\sum^{\mathrm{faces}}\left(\alpha_{\mathrm{d;f}}^{t+\Delta t}\frac{\rho_{\mathrm{c}}}{\rho_{\mathrm{m;f}}}\underline{\boldsymbol{v}}_{dj;\mathrm{f}}\cdot\underline{\boldsymbol{n}}_{\mathrm{f}}A_{\mathrm{f}}\right) \tag{5.61}$$

$$D(\alpha_{\mathrm{d}}^{t+\Delta t})=\sum^{\mathrm{faces}}\left(\left(\beta\mu_t+C_{\mathrm{E}}\right)\nabla\frac{\alpha_{\mathrm{d;f}}^{t+\Delta t}}{\rho_{\mathrm{m}}}\cdot\underline{\boldsymbol{n}}_{\mathrm{f}}A_{\mathrm{f}}\right) \tag{5.62}$$

The concentration field is now updated as follows: 1) update using only diffusion:

$$\alpha_{\mathrm{d}}^{*}=\alpha_{\mathrm{d}}^{t}+\frac{\Delta t}{V_{CV}}D(\alpha_{\mathrm{d}}^{*}) \tag{5.63}$$

2) update using the other fluxes:

$$\alpha_{\mathrm{d}}^{t+\Delta t}=\alpha_{\mathrm{d}}^{*}+\frac{\Delta t}{V_{CV}}U(\alpha_{\mathrm{d}}^{t+\Delta t}) \tag{5.64}$$

And finally, 3) calculate the total drift-flux to be used in the momentum balance (Equation (4.21)):

$$\underline{\boldsymbol{v}}_{dj}=\underline{\boldsymbol{v}}_{dj}^{*}+\frac{\rho_{\mathrm{m}}}{\rho_{\mathrm{c}}\alpha_{\mathrm{d}}^{*}}\left(\beta\mu_t+C_{\mathrm{E}}\right)\nabla\frac{\alpha_{\mathrm{d}}^{*}}{\rho_{\mathrm{m}}} \tag{5.65}$$

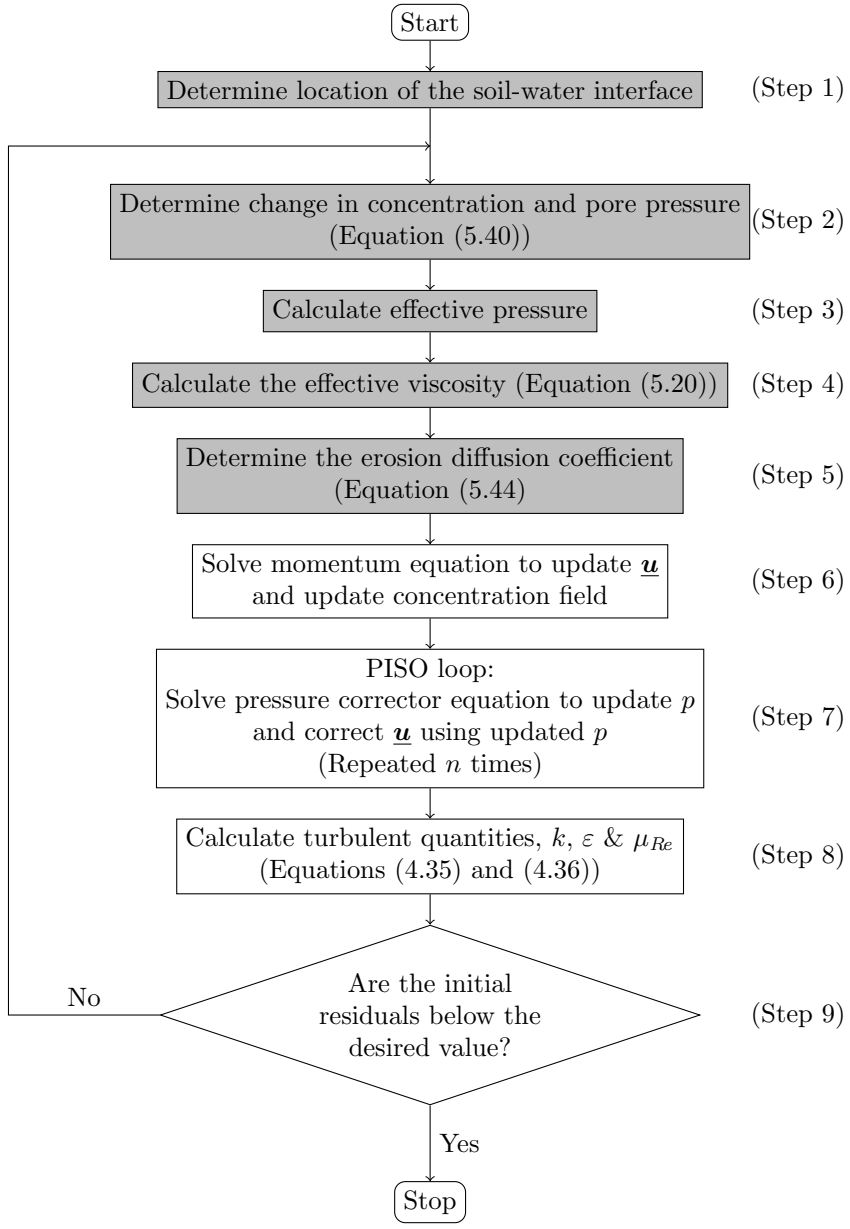

Figure 5.8: The solution procedure for the extended SettlingFoam model. Steps not in the original SettlingFoam model are labeled in light grey.

5.5 New Solution procedure

Compared to the original SettlingFoam, the solution procedure of the extended model has several new steps (Figure 5.8). The new procedure is as follows:

1. Each time step starts by determining the location of the soil-water interface. This is done by first determining which cells belong to the soil. Non-soil cells adjacent to soil cells are labelled as buffer cells, and the face between the two cells is added to the interface. Cell faces of the buffer cells not shared with a soil cell are added to the artificial interface.

2. Next the change in concentration due to dilation is calculated (Equation (5.39)), and used to calculate the pore pressure (Equation (5.40)). The calculated pore pressure is used to determine the dilatancy component of the drift flux (Equation (5.42)).

3. The pore pressure is then used in the calculation of the effective pressure. This is done by estimating the gradient of the effective pressure, and using this to solve a Laplace equation to determine the effective pressure.

4. Once the effective pressure is determined, the effective viscosity can be calculated (Equation (5.20)).

5. Then, the erosion flux is determined (Equation (2.59)), and used to calculate the erosion diffusion coefficient (Equation (5.44)).

What follows (Step 6–9) is equal to the solution procedure of the original SettlingFoam solver. Optionally the momentum balance is solved to update the velocity. Then the concentration field is updated. After this the pressure corrector loop is repeated a set number of times, decided by the user. In the pressure corrector loop, the pressure correction equation Section 5.1.1 is solved, and the velocity field is updated using Equation (5.11). After this the turbulence equations (Equations (4.35) and (4.36)) are solved. If the residuals are not below the desired values, all steps, starting from Step 2 are repeated.

Chapter 6

Validation sub processes

In this chapter, and the next, the model, as presented in Chapters 4 and 5, is validated. In this chapter the ability of the model to simulate the subprocesses important in unstable breaching is validated, while the validation of the models ability to model the actual unstable breaching process is handled in the following chapter. The subprocesses which are validated in this chapter are:

- The flow of sand-water mixtures, for sand concentrations up to 30%. this subprocess is validated by comparing modelling results to experiments of open channel flow of sand-water mixtures by Xingkui and Ning (1989).
- The formation of a dense bed due to settling of sediment. This is validated using experiments in a settling tank by Runge (1999), where an initially homogeneous sand-water mixture is allowed to settle and form a bed.
- The soil mechanical behaviour of the dense bed. To validate whether our approach can reproduce the formation of a yield surface, we apply the model to a purely cohesive vertical cut, for which analytical upper and lower bounds are known. The behaviour of granular material, without a cohesion but with an internal friction angle, is also validated. This is done by initializing piles of sand with varying initial slope angles, and varying internal friction angles.
- The erosion of a dense bed by a flow. This is first validated in a simple 1D channel flow, using cyclic boundaries. This validation serves mostly

to check the proper implementation of the erosion formula, as well as our implementation of dilatancy retarded erosion. Next, the model is applied to a sand-fill experiment by Mastbergen et al. (1988), where due to a balance between sedmentation and erosion, a certain equilibrium slope should form.

- The formation of an underpressure due to dilation. This process is validated using experiments by Rondon et al. (2011) of a granular column collapse under different initial concentrations. During these experiments pore pressures where measured which can be used as validation.

6.1 Channel flow

The flow of sand-water mixtures, for low sand concentrations is validated by comparing modelling results to experiments of open channel flow of sand-water mixtures by Xingkui and Ning (1989).

6.1.1 Methods

Xingkui and Ning (1989) studied open channel flow of sediment-laden water, in a channel 0.3 m wide, and 20 m long, with an incline of 1%. They used beach sand with a median grain diameter, D_{50}, of 150 µm, and a density of 2640 kg m^{-3}, with concentrations up to 2.1%, and plastic particles with a median grain diameter, D_{50}, of 266 µm, and a density of 1052 kg m^{-3}, with concentrations up to 15%. They published measurements of mean velocity and concentration along the centreline of the channel, which are used to compare their results to model results.

Here the three experiments (named SQ1, SQ2 & SQ3 in Xingkui and Ning (1989)) using beach sand, are modelled. The height of the flow is 8 cm for all three flows. In the model the flows are modelled with a rigid lid, instead of a free water surface. The difference between the three experiments is the average concentration, $\bar{\alpha}$, which is 0.0054, 0.0177, and 0.021 for SQ1, SQ2, and SQ3. The experiments are modelled in 3D, with a single cell, and periodic boundaries, in the streamwise direction. 32 cells are used along the height of the channel, and 64 along the width of the channel. The forcing is done via a pressure jump over the periodic boundary, based on the gravitational acceleration and the 1% incline. Instead of a free surface, a rigid lid with a slip boundary condition is applied.

The Schmidt-Prandtl number, β (see Equation (4.30)), which controls the relation between turbulent diffusion and diffusion of particles, is set to 1, sim-

ilar to successful simulations carried out by Goeree et al. (2016) for the same experiments.

6.1.2 Results

Model results compare well with the experimental measurements (Figure 6.1). Flow velocities follow a similar logarithmic profile as measured, but are slightly larger. This might be due to an error in the incline, or due to roughness applied at the wall boundaries. The concentration also match well with experimental results.

6.2 Settling

The settling of sediment is validated using experiments in a settling by Runge (1999), where an initially homogeneous sand-water mixture is allowed to settle and form a bed.

6.2.1 Method

These experiments were carried out in a circular column with a height of 1.5 m and a diameter of 0.28 m. Inside this column an initial homogeneous sand-water mixture is formed with concentrations ranging from 5 to 45%, using two types of sand with median diameters of 270 µm and 80 µm. These mixtures are then allowed to settle. Concentration meters are placed along the height of the column, measurements of the concentration meters at 0.9 m, 1.05 m, 1.2 m and 1.35 m from the bottom are reported by Runge (1999). A rotating grid is installed inside the column to create different levels of turbulence, for this validation only experiments without this grid are used. Experiments 42, 46, 108, and 112 are used to for validation (Table 6.1).

Exp #	D_{50} (µm)	α_d	T (°C)
42	80	0.25	24.7
46	80	0.17	21.7
108	270	0.25	25.1
112	270	0.17	21.2

Table 6.1: Experiments from Runge (1999) used for validation

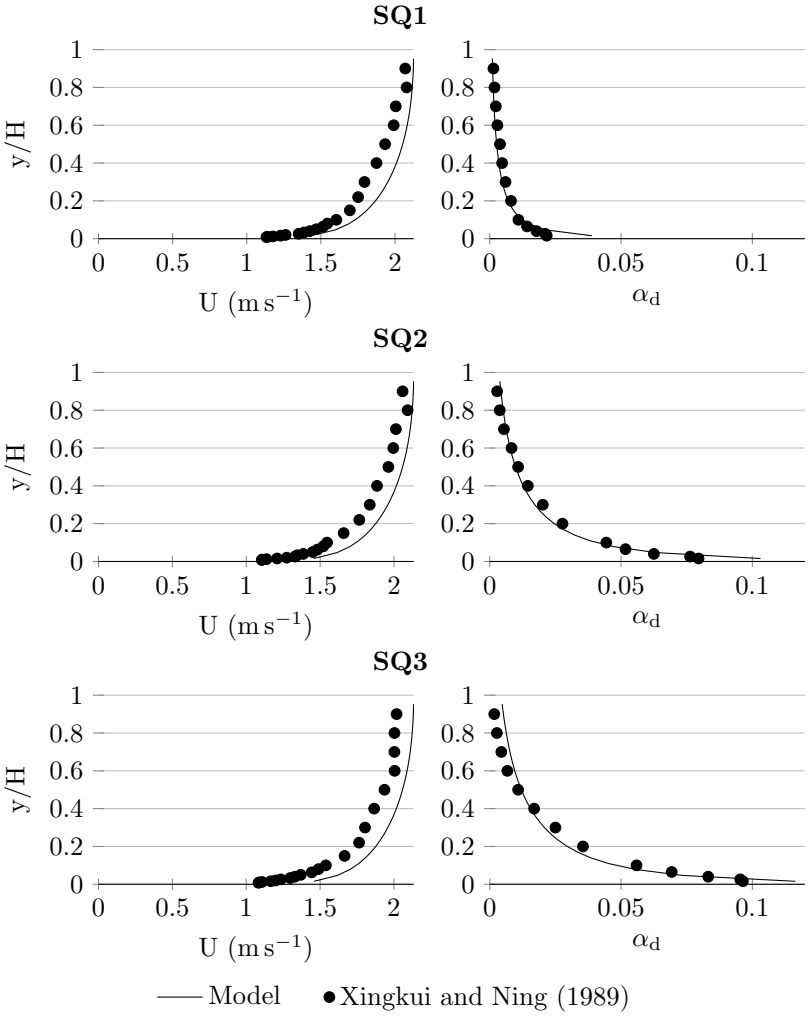

Figure 6.1: A comparison between experimental results obtained by Xingkui and Ning (1989), and model results, for three different experiments, SQ1, SQ2, and SQ3.

6.2.2 Results

The change from initial concentration to clear water at the concentration meters takes longer during the experiments, than during the simulation (Figure 6.2). During the experiments this change is spread over 10 s to 50 s, while during the numerical simulation, the change takes only a few seconds. This can be caused by using only a single grain diameter for the simulation, while the sand used during the experiment contains a range of grain diameters, each settling at a different rate.

However, the timescale of the settling, or the distance along the time axis between measurements at the different levels, is very similar between the experiments and the numerical simulations. This indicates that the calculated hindered settling velocities for our single grain diameter are accurate.

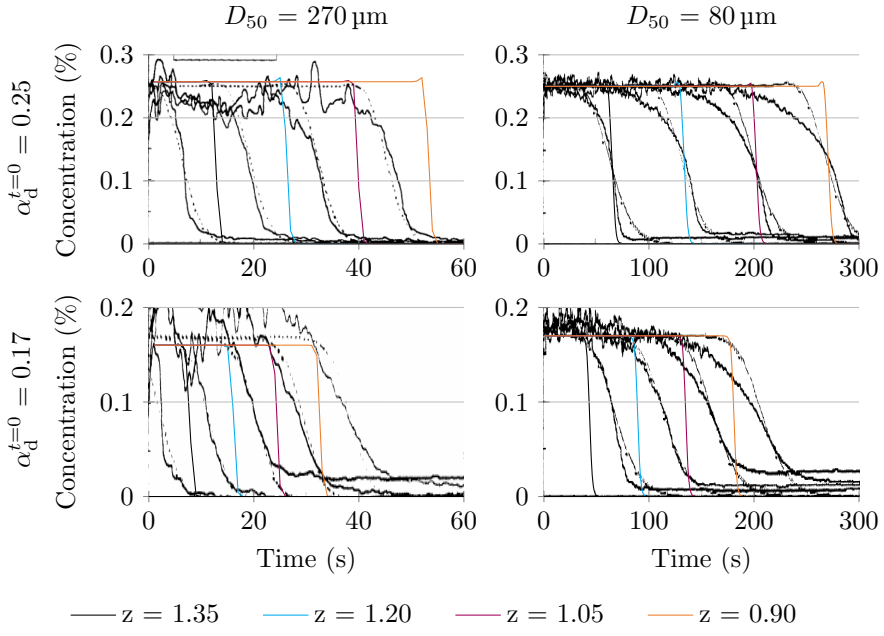

Figure 6.2: Concentrations measured during settling tests at various heights. Numerical results are plotted over results found in Runge (1999).

6.3 Erosion

The correct implementation of erosion in the model is checked by comparing the erosion velocity of a flat bed, over which a flow driven by a constant pressure gradient. This constant pressure gradient should lead to a constant shields parameter, θ, as long as acceleration is negligible.

6.3.1 Method

A two dimensional domain of 0.4 m high and 0.1 m wide is used (Figure 6.3). A Cartesian grid is used with grid cells of 0.004 m $\times$ 0.004 m (Unless mentioned otherwise). Inside this domain, a layer of sand, with a concentration of 60% is placed up to a height of 0.1 m. A cyclical is used for the inlet and outlet, and a slip boundary condition is applied at the top of the domain. A concentration jump is applied, so that the sand concentration of inflowing water is always zero.

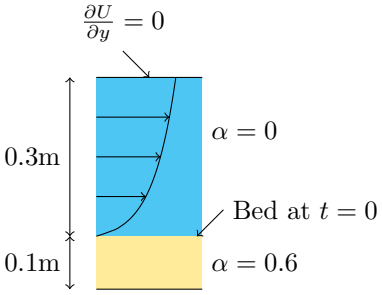

Figure 6.3: The setup of the erosion tests in OpenFOAM.

A pressure jump is applied between the inlet and outlet. The pressure jump is only applied where there is no soil adjacent to the inlet boundary. This pressure jump is chosen so that the total force on the water column is constant. If there is no acceleration this constant force can be related to the shields parameter, θ. Simulations are initiated by running the model with a fixed bed until a steady state is reached. The simulation is then run with an erodible bed until no soil remains in the domain. Results are then compared to the theoretical results, which are simply using the erosion speeds following from whatever erosion formula is used (In this case van Rijn (1984)), using the Shields parameter related to the forcing. This means that we only check whether the formula is implemented correctly, and not whether the resulting

erosion is actually correct. Unless mentioned otherwise, the dilatancy of the soil is ignored.

6.3.2 Results

Increasing the forcing, and thus Shields parameter, results in faster erosion velocities in agreement with the theory (Figure 6.4). However, the observed erosion velocity is slower than predicted by theory. This can be because as the bed erodes, and the height of the water flow increases, water close to the bed needs time to accelerate to a steady state. Until it reaches this steady state, the actual Shields parameter is lower then the theoretical, and therefor erosion velocity is also lower. When the Shields parameter is held fixed, instead of being derived from the flow field, the erosion velocity is indeed in agreement with the theoretical (Figure 6.5).

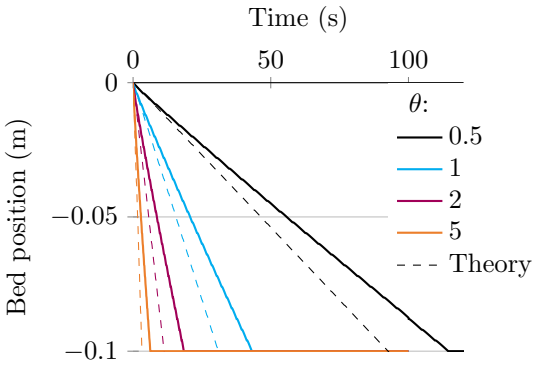

Figure 6.4: Simulated position of the bed, compared to the theoretical solution, for varying Shields parameters.

Changing the grid size, has small effects of the erosion velocity (Figure 6.6). Previous simulations did not take dilatancy into account, and therefore the effect of retarded erosion (Section 2.4.1) is not seen. When permeability of the soil is reduced from $1000\,\mathrm{m\,s^{-1}}$ (Dilatancy effects are negligible) to $1 \times 10^{-4}\,\mathrm{m\,s^{-1}}$, a clear decrease in erosion velocity is observed. The reduced erosion velocity is in agreement with velocities predicted using Section 2.4.1.

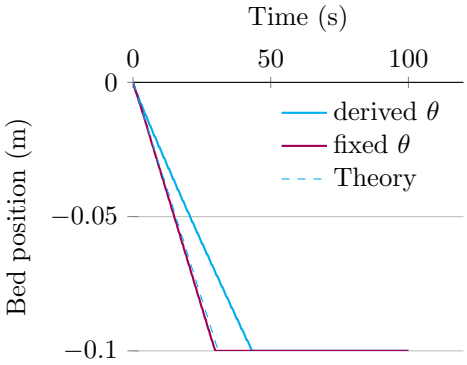

Figure 6.5: Simulated position of the bed, compared to the theoretical solution, with the Shields parameter either fixed, or derived from the flow properties.

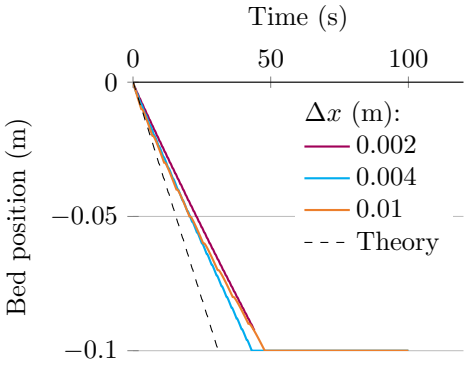

Figure 6.6: Simulated position of the bed, compared to the theoretical solution, for varying grid size parameters.

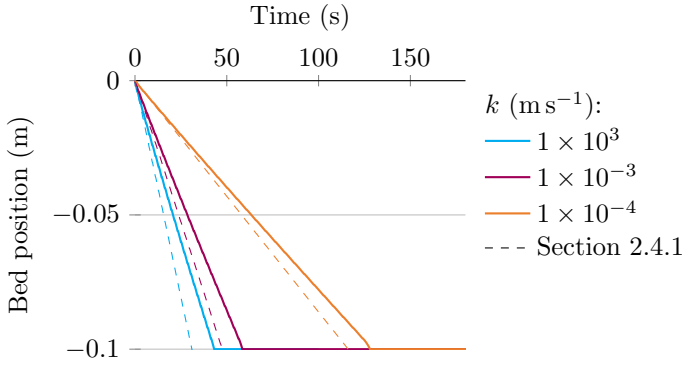

Figure 6.7: Simulated position of the bed, compared to the theoretical solution, for varying permeabilities.

6.4 Bingham flow

In this section the model is applied to the plane Bingham Poiseuille flow. The steady state solution and stopping times are compared to analytical solutions. This serves as a check of the correct implementation of the yield stress in the model, and the ability to model large scale deformations.

6.4.1 Steady state

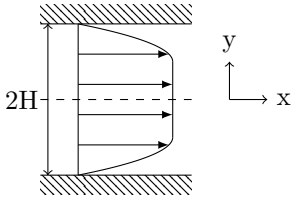

Figure 6.8: Bingham pouiselle flow

The plane Bingham Pouiselle flow is the flow of a fluid, with a yield stress τ_y, and a viscosity μ_c through a channel of total height $2H$, with no slip boundary conditions (see Figure 6.8), where the flow is driven by a constant pressure gradient, $\frac{\mathrm{d}p}{\mathrm{d}x}$, The steady state horizontal velocity profile for a Bingham Pouiselle flow is:

$$u_x = \begin{cases} \frac{1}{2\mu_c}\frac{\mathrm{d}p}{\mathrm{d}x}\left(H - y_0\right)^2 & \text{for } 0 \leq |y| \leq y_0 \\ \frac{1}{2\mu_c}\frac{\mathrm{d}p}{\mathrm{d}x}\left(H^2 - y^2\right) - \frac{\tau_y}{\mu}\left(H - y\right) & \text{for } y_0 \leq |y| \leq H \end{cases} \tag{6.1}$$

where

$$y_0 = \tau_y |\frac{\mathrm{d}p}{\mathrm{d}x}|^{-1} \tag{6.2}$$

This is valid when:

$$\frac{\mathrm{d}p}{\mathrm{d}x} > \frac{\tau_y}{H} \tag{6.3}$$

The Bingham Pouiselle flow is modelled using: $\tau_y = 0.25\,\mathrm{Pa}$, $H = 0.5\,\mathrm{m}$, $\mu = 1\,\mathrm{Pa\,s}$, and $\frac{\mathrm{d}p}{\mathrm{d}x} = 1\,\mathrm{Pa\,m^{-1}}$. The domain is discretized into 64 cells over the height, giving us a grid size of $1/64\,\mathrm{m}$. The regularization parameter ranges from $1 \times 10^{-2}\,\mathrm{s^{-1}}$ to $1 \times 10^{-5}\,\mathrm{s^{-1}}$. The model runs until a steady state is reached.

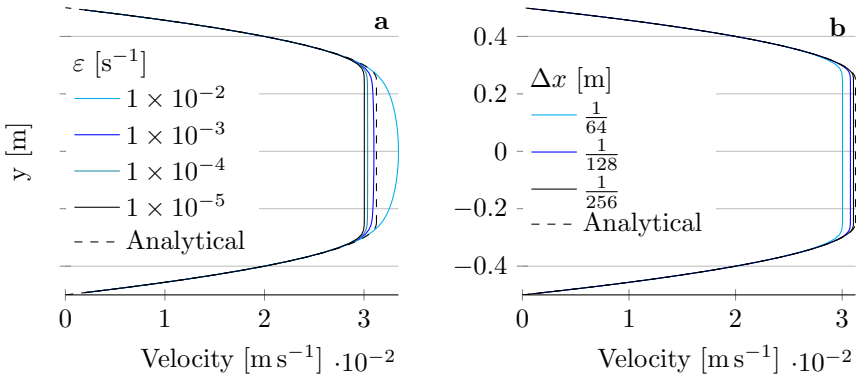

Figure 6.9: Comparison between OpenFOAM results and the analytical solution of the Bingham Pouiselle flow, a) for several regularization parameters, b) for several grid sizes, using $\varepsilon = 1 \times 10^{-5}$

The modelled steady state flow profiles are close to the analytical solution (Figure 6.9). As the regularization parameter decreases, the shear inside the plug also decreases. However, as the regularization parameter decreases, the modelled velocity of the plug converges to $0.03\,\mathrm{m\,s^{-1}}$, instead of the analytical value of $0.031\,25\,\mathrm{m\,s^{-1}}$. This discrepancy reduces as the grid size decreases (Figure 6.9b).

6.4.2 Cessation

When a steady state plane Bingham Pouiselle flow is reached, and the pressure gradient is reduced below the critical value for flow (Equation (6.3)), the flow rate will reduce to zero in a finite time. An analytic upper bound for this stopping time is given by Chatzimina et al. (2007):

$$T_f \leq \frac{4}{\pi^2} \ln \left[1 + \frac{\pi^2}{4} \frac{||u(0)||}{Bn - f} \right], \tag{6.4}$$

where T_f is the dimensionless stopping time, which is the stopping time t_f made dimensionless by $\rho H^2/\mu_c$, Bn is the Bingham number, which is the yield stress made dimensionless by $\mu_c V/H$, f is the pressure gradient made dimensionless by $\mu_c V/H^2$, where V is the steady state mean velocity of the domain, and $||u(0)||$ is defined as:

$$||u(0)|| = \int_0^1 U \, \mathrm{d}Y, \tag{6.5}$$

where U is the steady state dimensionless velocity u/V, and Y is the dimensionless y-coordinate, y/H.

The ability of the model is tested by reducing the pressure gradient to zero for six different simulations, with varying Bingham numbers. There is good agreement between the analytical upper limit (Equation (6.4)) and the modelled stopping times (Figure 6.10).

6.5 Vertical cohesive wall

To test the ability of the model to accurately reproduce the transition of cohesive soils, from stable to unstable, it is applied to the well-known vertical cohesive wall problem. In this test, a vertical cut submerged in water is initiated, as in Figure 6.11, with height h, and cohesion c. This simulation is carried out with different cohesions to identify the critical cohesion, c_{cr}, where failure of the vertical wall occurs.

6.5.1 Known Analytical Bounds

While no exact limit has been derived for this problem, it is possible to derive an upper and a lower bound for the critical cohesion. The simplest lower limit

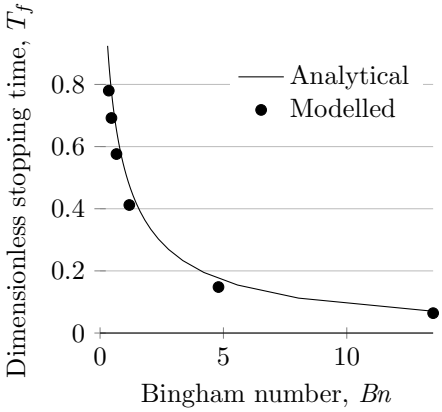

Figure 6.10: Comparison between OpenFOAM results and the analytical upper bound of the stopping time for the Bingham Pouiselle flow

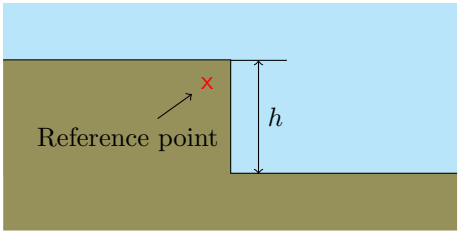

Figure 6.11: Vertical wall of cohesive material . The red cross indicates the reference point. All velocity plots in the results section are sampled at this reference point

Table 6.2: Default values used in simulations

Variable	Value
Wall height [m]	1
Gravitational constant [$\mathrm{m\,s^{-2}}$]	9.81
Dispersed phase concentration [%]	0.6
Dispersed phase density [$\mathrm{kg\,m^{-3}}$]	2650
Continuum phase density [$\mathrm{kg\,m^{-3}}$]	1000
Regularization parameter [$\mathrm{s^{-1}}$]	1×10^{-5}
Grid size [m]	0.05
Threshold concentration for rheology [%]	0.5

can be derived by assuming a straight slip surface. In this case we find that the cohesion needed to keep a wall with height h stable, is

$$c_{\mathrm{cr}} \geq \frac{h\alpha_d \left(\rho_{\mathrm{d}} - \rho_{\mathrm{c}}\right) g}{4}. \tag{6.6}$$

A higher limit was found by Fellenius (1948) by using circular slip surfaces:

$$c_{\mathrm{cr}} \geq \frac{h\alpha_d \left(\rho_{\mathrm{d}} - \rho_{\mathrm{c}}\right) g}{3.83}. \tag{6.7}$$

The best analytical upper limit was found by De Josselin De Jong (1980):

$$c_{\mathrm{cr}} \leq \frac{h\alpha_d \left(\rho_{\mathrm{d}} - \rho_{\mathrm{c}}\right) g}{3.39}. \tag{6.8}$$

More accurate, but not analytical, limits were found recently, using the finite element method, by Pastor et al. (2000)

$$\frac{h\alpha_d \left(\rho_{\mathrm{d}} - \rho_{\mathrm{c}}\right) g}{3.786} \leq c_{\mathrm{cr}} \leq \frac{h\alpha_d \left(\rho_{\mathrm{d}} - \rho_{\mathrm{c}}\right) g}{3.760}. \tag{6.9}$$

6.5.2 Method

The values given in Table 6.2 are used, unless mentioned otherwise. For these values, Pastor et al. (2000) predict a critical cohesion between 2565 Pa and 2582 Pa

We run this test case for 0.2 seconds, and look at velocity magnitudes at the reference point (See Figure 6.11). These velocities should indicate whether

the vertical wall is stable or not. When it is not stable, constant acceleration is expected, while for a stable simulation no acceleration should occur. Due to the regularization applied in Equation (5.17), the final velocity for stable solutions will be non-zero, but after an initial acceleration towards this non-zero value, no further acceleration should occur.

6.5.3 Results

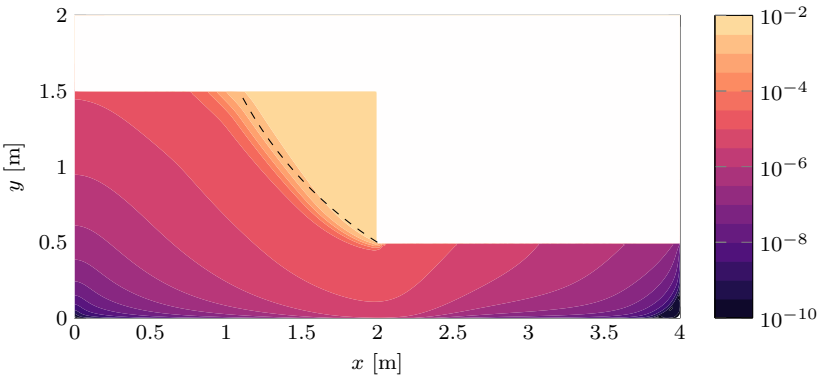

Figure 6.12: Contour plot of velocity magnitude, U, $[\mathrm{m\,s^{-1}}]$ for a cohesion of 2200 Pa, 0.1 seconds after the start of the simulation. The dashed line denotes the circular slip surface of Fellenius.

The contour plots of the velocity magnitude (Figure 6.12) and the second invariant of the shear rate (Figure 6.13) for a cohesion of 2200 Pa, show a band with strong gradient in the velocity. This indicates the development of a slip surface that separates non-moving soil from the mobilized soil wedge. The dashed line in both figures denote the circular slip surface given by Fellenius (1948). This slip circle corresponds well with the area of high velocity gradients. In the stable parts of the vertical cohesive wall, a non-zero velocity is observed. It is again hypothesized that this is the result of the regularization.

Although there is no validation material for the deformation of the vertical wall after failure, it is still interesting. To show the deformation after failure, longer simulations of 4 seconds are carried out with cohesions of 2000 Pa and 1500 Pa (Figures 6.14 and 6.15). With a cohesion of 2000 (Figure 6.14), we see a small slump of the vertical wall, which comes to a stop after approximately 2 seconds. With a cohesion of 1500 Pa (Figure 6.15), we see a larger deformation

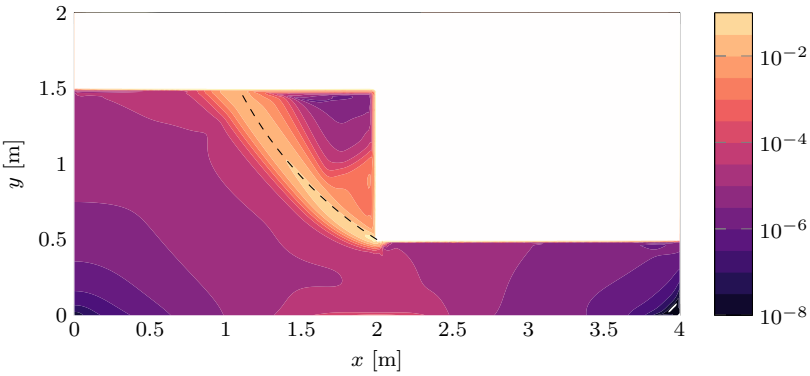

Figure 6.13: Contour plot of the second invariant of the shear rate, $\dot{\gamma}$, $[s^{-1}]$ for a cohesion of 2200 Pa, 0.1 seconds after the start of the simulation. The dashed line denotes the circular slip surface of Fellenius.

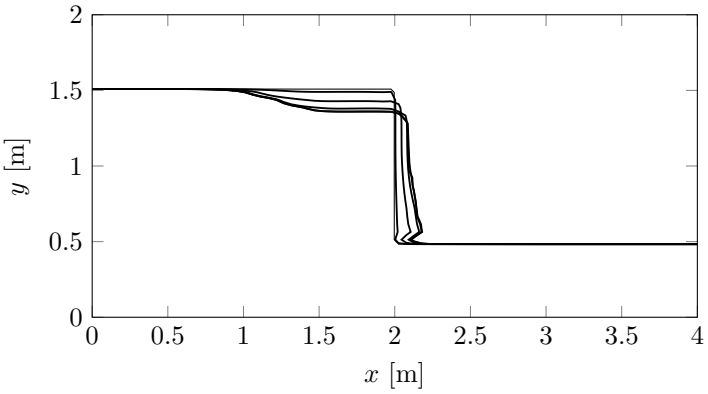

Figure 6.14: Contours of $\alpha = 0.45$ plotted every 0.5 seconds, for a cohesion of 2000.

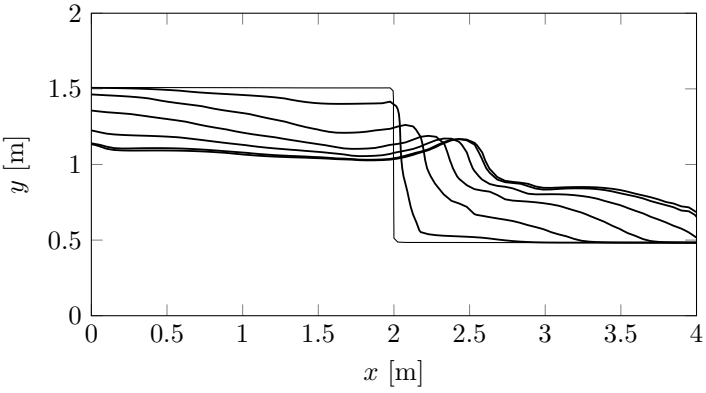

Figure 6.15: Contours of $\alpha = 0.45$ plotted every 0.5 seconds, for a cohesion of 1500.

of the wall, which comes to a stop after approximately 3 seconds.

The velocity magnitude at the reference point (See Figure 6.11), is strongly dependend on the cohesion used. A clear change in behaviour is seen between 2200 kPa to 2300 kPa (Figure 6.16). Simulations with a cohesion of 2200 kPa or lower show a clear continuous acceleration over the simulation period, indicating a yielded vertical wall. Simulations with a cohesion of 2300 kPa or higher on the other hand, show a small acceleration at the start of the simulation from 0 to a small velocity, after which the velocity remains constant, indicating an unyielded vertical wall. These results indicate a critical cohesion between 2200 kPa to 2300 kPa, lower than the lower boundary of 2565 kPa proposed by Pastor et al. (2000), but in the same order of magnitude.

The chosen regularization parameter for the viscosity regularization (Equation (5.20)) has a strong effect on the resulting velocity magnitude (Figure 6.17). For a yielded vertical cut, the acceleration increases as the regularization parameter decreases. The acceleration converges for regularization parameters of $1 \times 10^{-5}\,\mathrm{s}^{-1}$ and lower. For the unyielded vertical cut the regularization parameter affects the residual velocity, which converges to a fixed value for parameters of $1 \times 10^{-4}\,\mathrm{s}^{-1}$ and smaller.

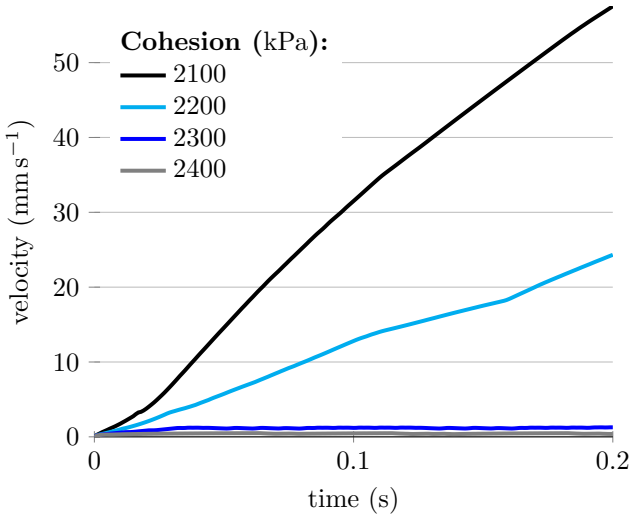

Figure 6.16: Velocity magnitudes, at the reference point in the vertical wall, for varying cohesions.

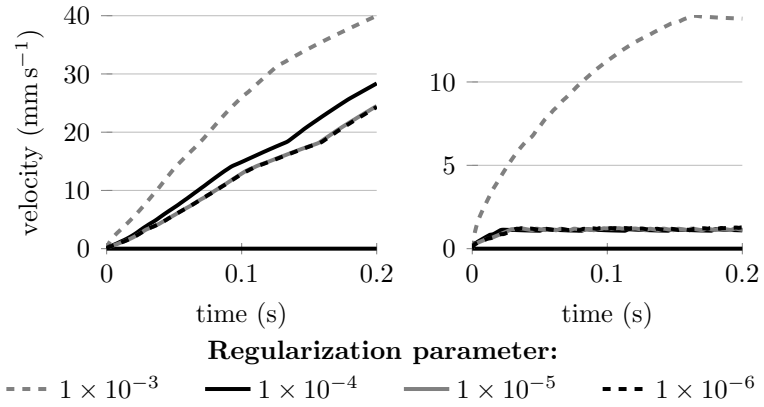

Figure 6.17: Velocity magnitudes at the reference point for varying regularization parameters, for cohesions of a) 2200, and b) 2300.

6.6 Internal friction angle

A simple test of the implementation of the friction angle, is to initiate simulations with triangular sand piles with varying initial slope angles, ϕ_{init}. When the initial slope angle is greater than the internal friction angle, ϕ_c, it is expected that sand starts moving until the slope angle is below the internal angle of friction. On the other hand, when the initial slope angle is milder than the internal friction angle, no flow should occur.

6.6.1 Results

Results show that the model behaves as expected (Figure 6.18). When the initial slope, ϕ_{init}, is milder than the internal friction angle, ϕ_c, the pile is stable and does not move (Figure 6.18b). When the initial slope is lower than the internal friction angle, movement of the pile is observed (Figure 6.18a,c & d). Movement stops when the slope angle drops below the internal friction angle.

Interestingly, the method used to determine the effective pressure (See Section 5.2.2) has an important effect on the results. When the hydrostatic effective pressure is used, no movement of the pile is observed, even when the slope angle exceeds the internal friction angle (Figure 6.18e). Both other methods do yield the expected movement of the pile.

6.7 Pore pressure feedback

To test the pore pressure feedback the data of Rondon et al. (2011) is used. Rondon et al. (2011) experimentally investigated the collapse of a granular column in a viscous liquid, for varying volume fractions. They varied the initial volume fraction from 0.55 to 0.6. For The dense columns (0.6) the pore pressure feedback slows down the process, while it speeds up the process for the loose columns. They used glass beads of 225 µm with a density of $2500\,\mathrm{kg\,m^{-3}}$, and an angle of repose of 21°. The equilibrium concentration of the material is 0.58.

Inside a flume with a length of 0.7 m, and a width and height of 0.15 m, filled with liquid with viscosities of 0.012 Pa s and 0.024 Pa s, they construct a columns with varying heights and lengths behind a liftable gate (Figure 6.19). During the experiment they measured the pore pressure at a single point, in the bottom of the tank, 2 cm from the end of the tank.

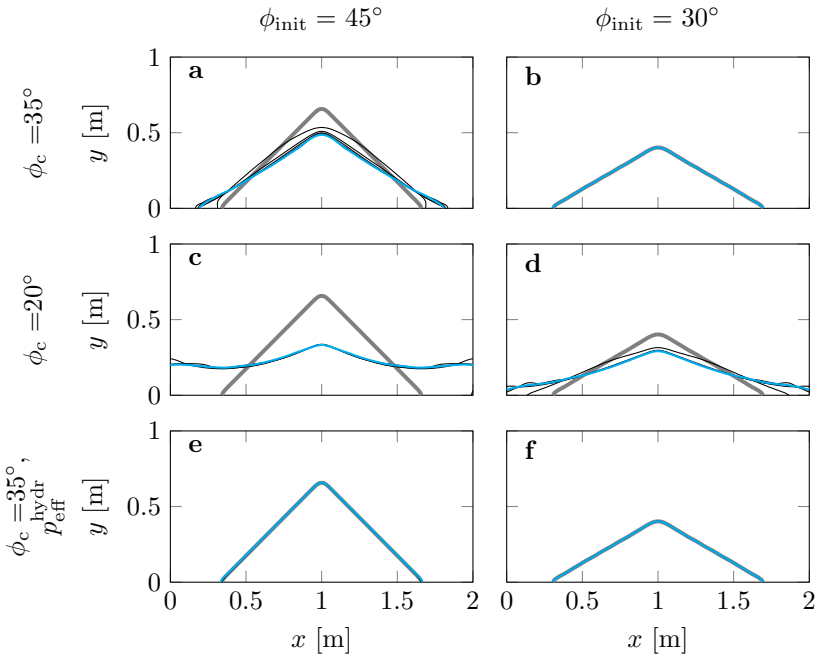

Figure 6.18: Contours of granular piles over time for varying initial slope angle, ϕ_{init}, and varying internal friction angle, ϕ_c. The last two are simulations where the effective pressure, p_{eff}, was assumed to be hydrostatic. Thick grey lines indicate the initial profile, and cyan lines indicate the final position of the granular pile, after 5 s of simulation. Black lines indicate profiles in between the initial and final position, for every second.

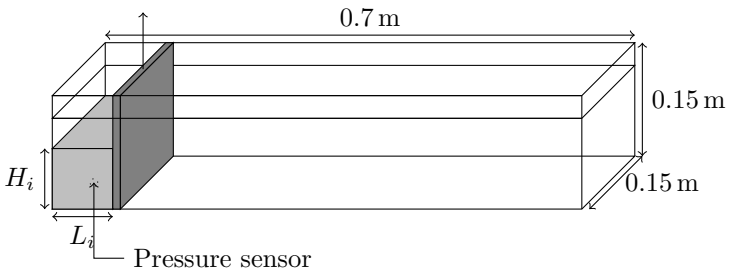

Figure 6.19: The setup used by Rondon et al. (2011).

For two experiments, pore pressure data is available. One is a case with dense packing ($\alpha_d = 0.6$), with a starting height of 4.2 cm, and starting length of 6 cm, and a liquid viscosity of 0.012 Pa s. The other is a case with loose packing ($\alpha_d = 0.55$), with a starting height of 4.8 cm, and starting length of 6 cm, and a liquid viscosity of 0.012 Pa s. Here we focus on the dense packing case.

The permeability of the granular media is not reported, and nothing is known about the relation between shear rate and dilation rate. Therefore, the permeability, k, and the dilation constant, C_{dil}, will be varied during the various simulations. The dilation constant, C_{dil}, controls the dilation angle (Equation (2.14)). A larger value of C_{dil}, results in larger dilation angles. The permeability will be varied by varying the shape factor, c_{shape}, in Equation (5.41), the base value will be the standard shape factor of 0.01. For the dilation constant a value of 4 is taken as base value, similar to Pailha and Pouliquen (2009).

6.7.1 Results

The overall behaviour of the pore pressure during the granular collapse is similar during both the simulation, and the experiment. There is a quick drop of pore pressure at the start, after which it slowly drops while the granular media dilates and shears. The peak of the pore pressure found in the simulations is larger than measured during the experiments, but in the same order of magnitude (Figures 6.20 and 6.21). After the initial peak, the pore pressure quickly returns to zero. The speed at which this reduction takes place is much higher during simulations than observed during experiments.

Permeability has a clear effect on the results (Figure 6.20). As the permeability decreases, the reduction of pore pressure slows down. As the shape factor reduces to 0.002, there is good agreement in reduction time between the experiment and simulation. However, the reduction of pore pressure during simulations is smoother than measured during the experiment. The reduction in permeability also slightly increases the peak pore pressure.

The dilation factor also has a strong influence on the results (Figure 6.21). For smaller values ($C_{\text{dil}} < 2$), increasing the factor increases the pore pressure peak. This is because at these lower values more shear is necessary the generate enough negative pore pressure to keep the granular column stable. For low values of C_{dil}, this negative pore pressure cannot be generated. For larger values ($C_{\text{dil}} \geq 2$), increasing the dilation factor leads to a wider peak, with a smaller peak value.

These results show that the pore pressure feedback mechanism functions as

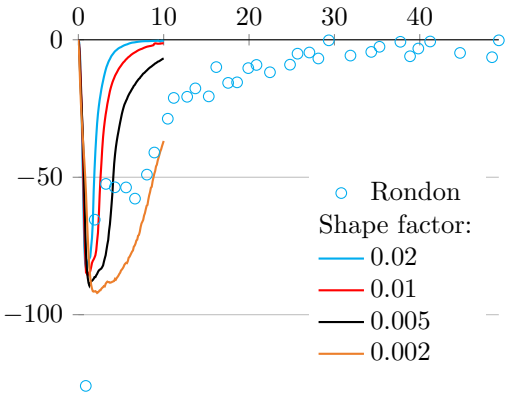

Figure 6.20: The pore pressures measured during numerical simulations with varying permeabilities, compared to the pore pressures measured during the laboratory experiments. $C_{\text{dil}} = 4$.

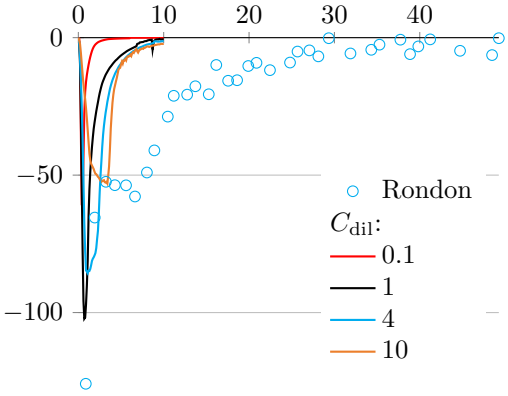

Figure 6.21: The pore pressures measured during numerical simulations with varying dilation factors, compared to the pore pressures measured during the laboratory experiments. Shape factor = 0.01.

expected in our numerical model. Furthermore, by varying the permeability and dilation factor we can get close to the observed experimental pore pressure measurements.

6.8 Sand fill

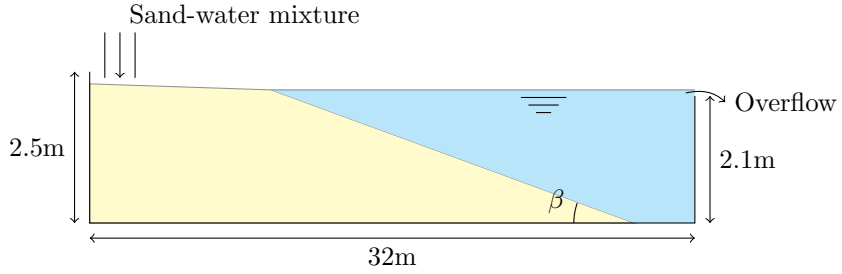

Figure 6.22: The experimental setup used by Mastbergen et al. (1988).

Mastbergen et al. (1988) created a sand fill dam in a $32\,\mathrm{m} \times 2.5\,\mathrm{m} \times 0.5\,\mathrm{m}$ flume, by releasing a sand-water mixture at one side. The resulting underwater slope, i, during construction of this dam (Figure 6.22) was measured. Two sand types were used, a fine sand with a median grain size of 135 µm, and a bit coarser sand with a median grain size of 200 µm, both with a density of $2650\,\mathrm{kg\,m^{-3}}$. Concentrations of the sand-water mixture where 12% and 30%, and the specific flow rates, q, used where: $0.01\,\mathrm{m^2\,s^{-1}}$, $0.025\,\mathrm{m^2\,s^{-1}}$ and $0.1\,\mathrm{m^2\,s^{-1}}$. This gives specific flow rates ($s = \rho_\mathrm{d} q \alpha_\mathrm{d}$) ranging from $3\,\mathrm{kg\,s^{-1}\,m^{-1}}$ to $80\,\mathrm{kg\,s^{-1}\,m^{-1}}$ For flows with a low production rate ($s < 10\,\mathrm{kg\,s^{-1}\,m^{-1}}$) grain flows were observed, with intermittent flow slides. Slope angles increased during grain flows, while after a flow slide much milder slopes were observed. Because of this the average slope varied a lot in time. For higher production rates ($s > 10\,\mathrm{kg\,m^{-1}\,s^{-1}}$) turbidity currents were observed. Flow slides occur a lot less for this kind of flow, after some time the slope reaches an equilibrium, α_eq, after which the slope barely changes. These slopes are reported by Mastbergen et al. (1988).

The numerical setup differs somewhat from the experimental setup. In the experimental setup the sand-water mixture is released from a pipe, which moves vertically during the experiment so that the discharge is always close to the sand bed. Instead, in the numerical setup, for simplicity a fixed inlet

point is chosen. Furthermore, instead of a free surface like in the experiments, a rigid lid is applied in the numerical simulations.

6.8.1 Results

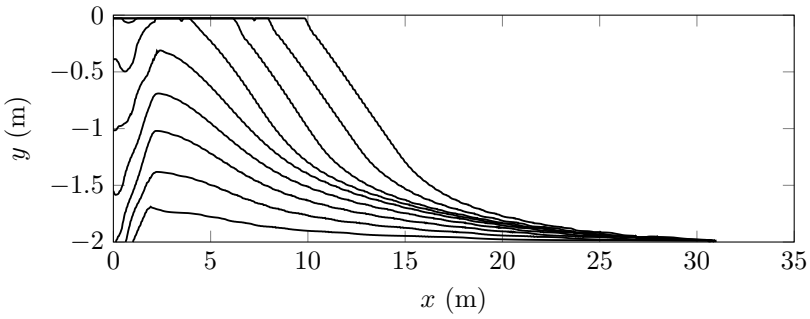

Figure 6.23: Contour lines of the soil every 100 seconds for the experiment using $D_{50} = 200\,\mu\text{m}$, $s = 30\,\text{kg}\,\text{s}^{-1}\,\text{m}^{-1}$.

The formation of the equilibrium slope occurs in roughly two stages. First, below the inlet a recirculation zone is formed, with a peak just right of it (Figure 6.23). This peak becomes higher as time goes on, until it reaches the top of the flume. Once the top of the flume is reached, the formed slope starts to expand towards the right, away from the inlet. After a while the top part of this slope keeps a constant slope angle.

These slope angles are compared to those measured by Mastbergen et al. (1988) and the empirical relation given (Figure 6.24). Similarly to Mastbergen et al. (1988), the slope is measured between $y = -1.5$, and $y = -0.5$ metres. Results for a median grain diameter of 200 µm compare well with those obtained experimentally. The resulting slopes with a median grain diameter of 135 µm are, as expected, milder than those with a median diameter of 200 µm. However, the measured slopes are milder than seen in experiments by about 5°. Overall, the numerical experiments capture the trends (Milder slopes for larger fluxes, and milder slopes for smaller grains) well.

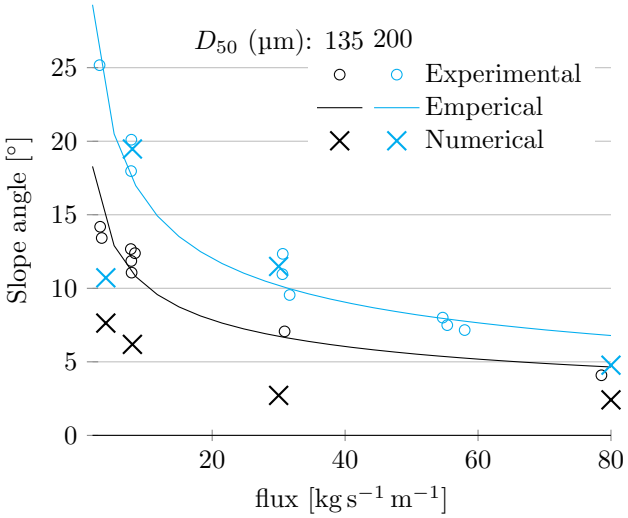

Figure 6.24: Comparison between experimental data, emperical formula (Mastbergen et al., 1988) and numerical results.

Chapter 7

Validation breaching process

This chapter compares the results of the model with the breaching experiments described in Chapter 3. Results of the model are compared to the experimental data, to judge how well the model is able to simulate the breaching process, and how well it can predict the change from a stable to an unstable breach. Profiles, wall velocities, pore pressures, and stability are compared. The sensitivity of the model to certain variables is also checked.

7.1 Methods

With our numerical model we simulate all the laboratory experiments (Chapter 3). Experiments in the lab with equal starting conditions, are simulated only once (Table 3.1).

For the sand properties the measured variables of Table 7.2 are used. The critical concentration, $\alpha_{\mathrm{eq};0}$, is chosen to be the same as as the sand concentration during breaching, just before it is released from the breach face $(1 - n_1)$.

This leaves the dilatancy factor, C_{dil} unknown. Here a value of 4 is chosen. This is similar to what was used by Pailha and Pouliquen (2009), who derived a value of 4.09 by looking at which slope angle motion is initiated with varying concentrations, and Wang et al. (2017), who used a value of 4 after calibration.

The domain of the numerical simulations is the same size as the tank used in the experiments, with a $0.3\,\mathrm{m} \times 0.3\,\mathrm{m}$ space cut out where the pump sump is located. The domain is divided into cells of $25\,\mathrm{mm} \times 25\,\mathrm{mm}$. Results are not

Table 7.1: List of simulated experiments, their comparable laboratory experiments, starting height H_{start}, starting slope β_{start} and sand type. Definitions of H_{start} and β_{start} are shown in Figure 7.1

Lab exp.	H_{start} (m)	β_{start} (°)	sand type
1, 2 & 3	0.66	0	GEBA
4, 5 & 6	1.17	0	GEBA
7	0.8	20	GEBA
8 & 10	1.47	0	GEBA
9	0.8	30	GEBA
11	0.66	30	GEBA
12	0.66	20	GEBA
13	0.66	0	D9
14	1.17	0	D9
15	0.8	30	D9
16	1.47	0	D9

Table 7.2: 50th and 15th percentile grain size, D_{50}, D_{15}, initial sand concentration, $\alpha_{\text{d};0}$, initial permeability, k_0, internal friction angle, ϕ_{c}, the critical concentration $\alpha_{\text{eq};0}$, and the density of the dispersed phase, ρ_{d}, of the GEBA and D9 sand types.

Sand	D_{50} (µm)	D_{15} (µm)	$\alpha_{\text{d};0}$	α_{eq}	k_0 ($\text{m}\,\text{s}^{-1}$)	ϕ_{c} (°)	ρ_{d} ($\text{kg}\,\text{m}^{-3}$)
GEBA	120	80	0.585	0.545	9.5×10^{-5}	35.8	2650
D9	330	225	0.57	0.56	2.2×10^{-4}	40.1	2650

yet fully converged at this grid size, but this size is chosen to keep simulation times reasonable.

The pump sump is replaced by an outlet boundary. The return flow is modelled as an 0.3 m wide inlet boundary, in the top right of the domain. At the inlet and outlet there is a constant flow of $1.5\,\mathrm{l\,s^{-1}}$. All other boundaries are wall boundaries, with a no slip condition.

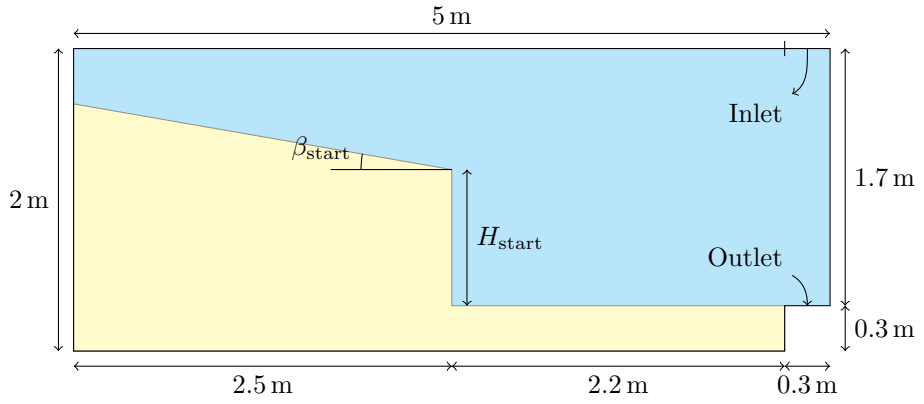

Figure 7.1: Numerical domain used for the breaching simulations.

There is no removable gate employed in the numerical simulations. Instead, the sand bed is initiated without, and is able to move immediately after starting the simulation. Effects caused by the lifting of the gate (Disturbance of the soil near the gate, and erosion of the bottom of the breach face while the gate is not fully lifted) are thus not modelled.

The viscosity regularization parameter, ε, is set to $1 \times 10^{-3}\,\mathrm{s^{-1}}$, chosen as small as possible, while keeping the simulation stable. And a maximum viscosity, $\mu_{\max}$ of $1 \times 10^{6}\,\mathrm{Pa\,s}$, chosen as large as possible, while keeping the simulation stable. The time step used during the simulation is 0.002 s. The simulation is run until the breach is no longer active, defined here as not change in the profile for at least 10 seconds.

7.2 Results

Simulation results show that the model is able to qualitatively reproduce the laboratory experiments. Just after the start of the experiments the soil re-

mains stable due to a large excess negative pore pressure formed inside the soil (Figure 7.3), and a turbidity current is formed by sand released from the steep breach face (Figure 7.2), with increasing velocity as the sediment moves down (Figure 7.3). Initially ($t = 0.01\,\mathrm{s}$) the negative pore pressure concentrates around the initial shear plane. As the pore pressure drops, the yield stress along this plane increases, causing a shear plane to form elsewhere, and decrease pore pressure along the plane instead. As the pore pressure drops along this new plane, again another shear plane will form, and so on. After 5 s, a large area of negative pore pressure can be observed.

As the experiment continues, due to sand released at the wall, the breach face moves horizontally. Part of the released sand settles at the toe of the breach, with a lower concentration. During the experiments the excess pore pressure reduces, and the peak moves closer to the breach face. As the breach height and angle decreases over time, so does the size and the velocity of the turbidity current.

Finally, at the end of the simulation, a bed is formed, with angles milder than the internal friction angle. No excess pore pressure, or turbidity current remains.

7.2.1 Profiles

Here we compare three representative experiments (Figures 7.4 to 7.6). One experiment without slope, using GEBA sand (Figure 7.4), one experiment with slope, using GEBA sand (Figure 7.5), and one experiment without slope, using Dorsolit 9 sand (Figure 7.6).

The profiles show that the model is able to numerically reproduce breaching behaviour. The steep breach wall is semi-stable due to negative pore pressure, and moves horizontally by releasing particles at the breach face, instead of failing due to a large slide. As the experiment progresses, the breach wall diminishes in size and becomes less steep. However, comparing numerical profiles to experimentally obtained profiles reveals several differences between experiments and simulation, the most important are:

- The buildup of a slope at the toe of the breach is slower during simulations than observed in experiments. This causes the breach height to reduce slower in simulations, compared to experiments. Thus, unstable breaching becomes more likely. It also causes stable breaches to travel further horizontally.

- In the simulations, during breaching, there is strong rounding of the profile near the top of the breach wall. This rounding is not observed

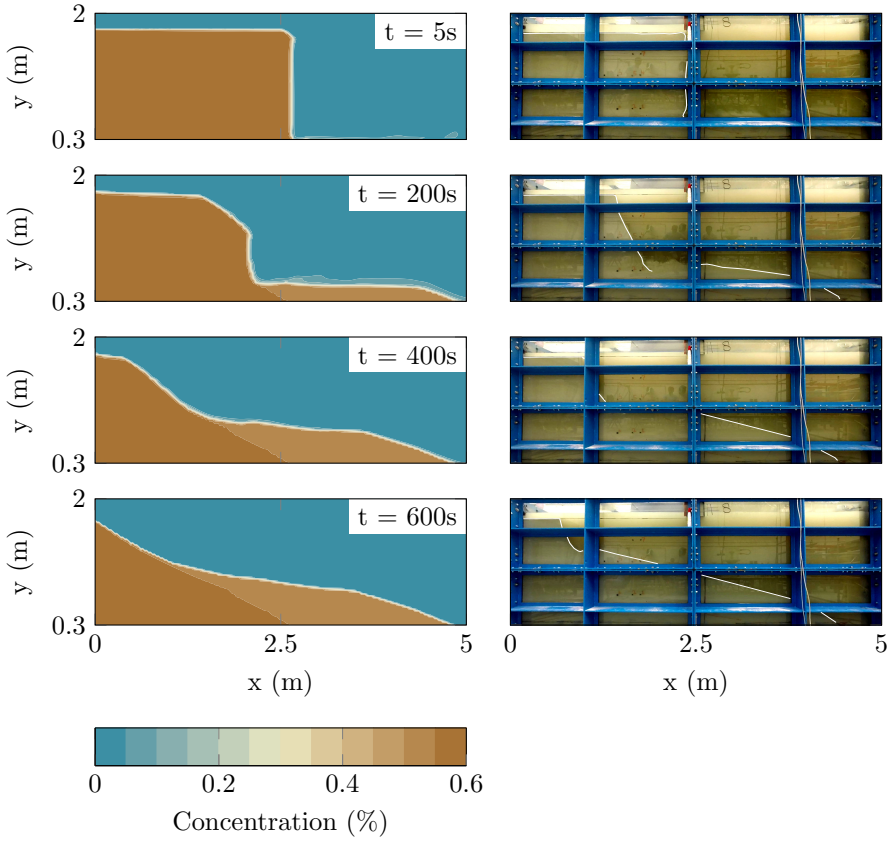

Figure 7.2: Comparison between simulated concentrations (Left) and the images of the laboratory experiment 8 ($H_{\text{start}} = 1.47\,\text{m}$, $\beta_{\text{start}} = 0°$, GEBA sand).

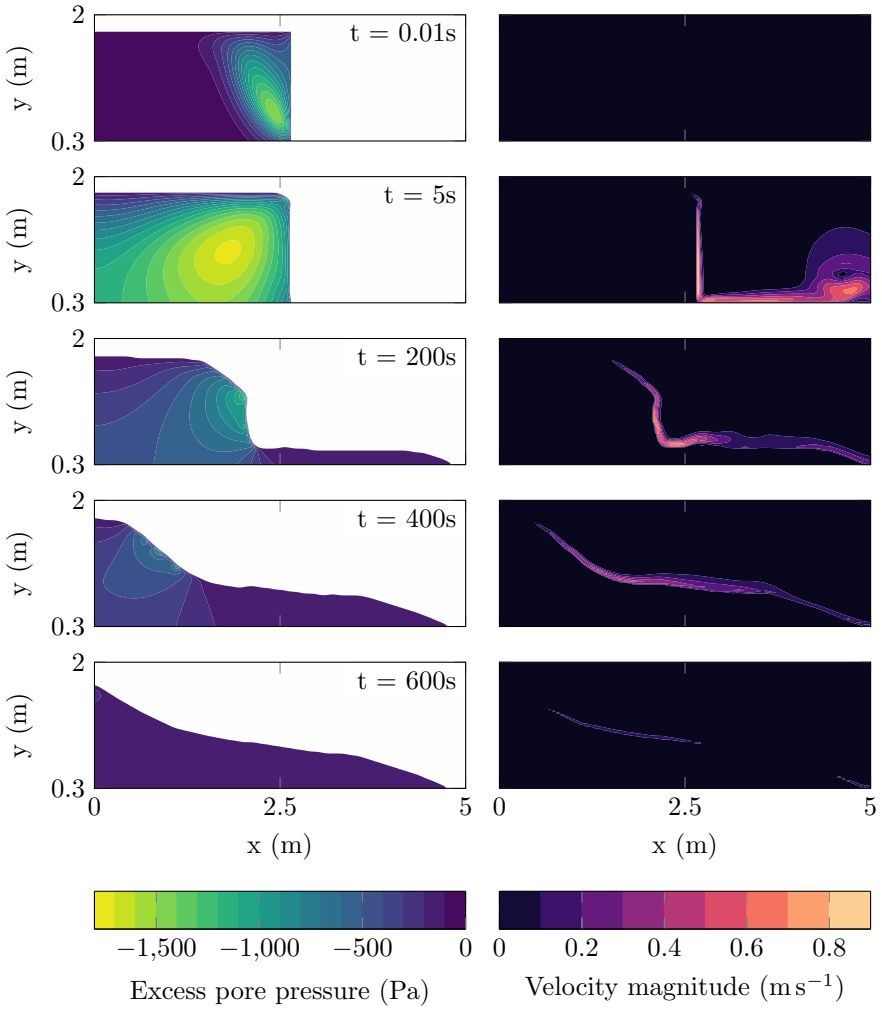

Figure 7.3: Excess pore pressure inside the soil, and mixture velocity magnitudes during simulation of experiment 8 ($H_{\text{start}} = 1.47\,\text{m}$, $\beta_{\text{start}} = 0°$, GEBA sand).

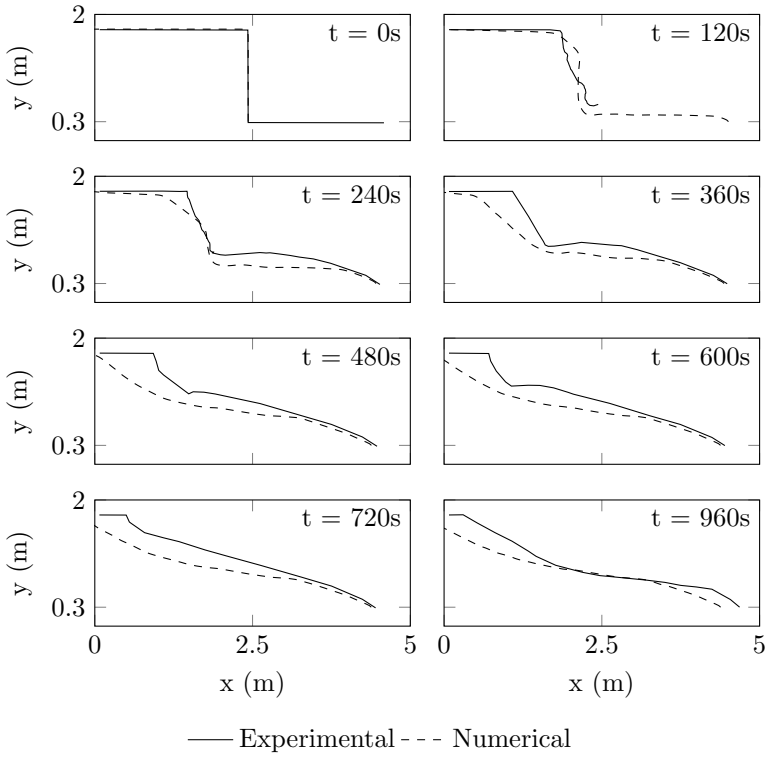

Figure 7.4: Comparison of numerical and experimental profiles for experiment 8 ($H_{\text{start}} = 1.47\,\text{m}$, $\beta_{\text{start}} = 0°$, GEBA sand).

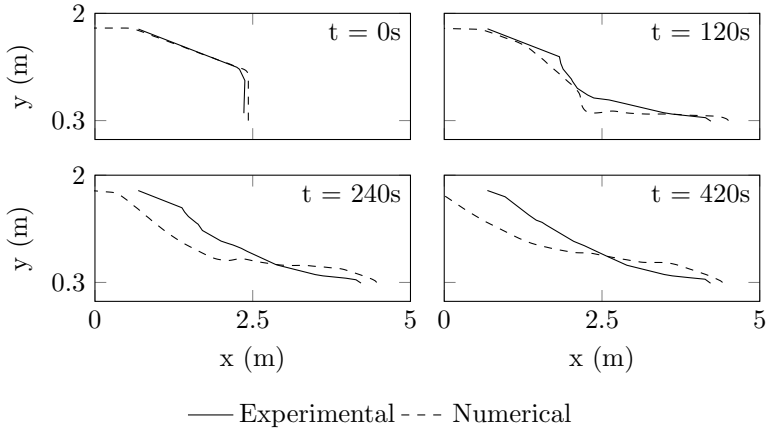

Figure 7.5: Comparison of numerical and experimental profiles for experiment 7 ($H_{\text{start}} = 0.8\,\text{m}$, $\beta_{\text{start}} = 20°$, GEBA sand).

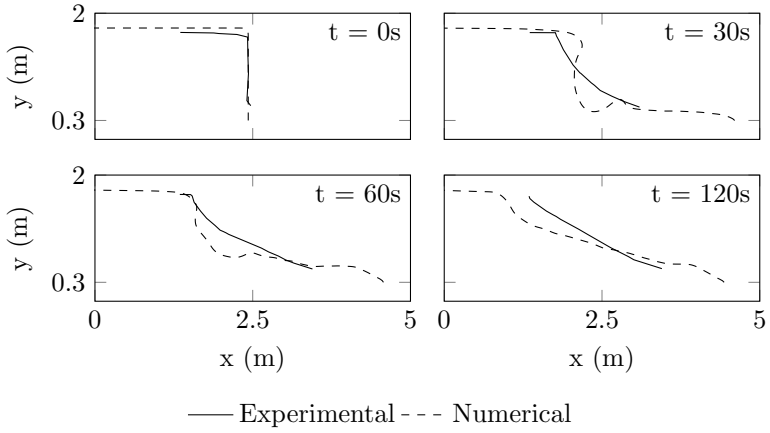

Figure 7.6: Comparison of numerical and experimental profiles for experiment 16 ($H_{\text{start}} = 1.47\,\text{m}$, $\beta_{\text{start}} = 0°$, Dorsolit 9 sand).

during experiments. This is particularly troublesome during experiments with a slope above the wall, where this effect is even larger. This also causes breaches to travel further horizontally. The amount of rounding observed depends on values of C_{dil} and Δx, with more rounding for larger grid cells and lower dilatancy factors. However, the lower part of the breach wall, not affected by the rounding at the top, moves with a velocity similar to that observed during experiments.

- For the experiment with Dorsolit 9 sand (Experiment 16, Figure 7.6), the breach wall advances faster initially in experiments. This is likely caused because large slides observed at the start of these experiments are not observed in simulations. These slides have a large contribution to the wall velocity at the start of experiments.

7.2.2 Wall velocity

The experimental and numerical average x-coordinate of the breach wall over time are compared for the three experiments (Figure 7.7). Similar behaviour is observed for all three experiments. Initially, there is a match between the numerical and experimental breach wall positions. However, after a while, a difference between the two emerges. In the numerical simulations the wall is moving faster than during experiments. During the experiments, the wall velocity reduces over time. During numerical simulations the wall velocity reduces slower, or even increases.

This effect is also visible in the mean difference between numerical and simulated velocity. Figure 7.8 displays the difference in wall velocity, averaged over $0.005/k_0$ (the time it takes to transverse 0.1 m if we assume $v_{\text{wall}} = 20k_0$). For experiments using GEBA sand, the difference is initially almost 0, and increases over time to a maximum of $3\,\text{mm}\,\text{s}^{-1}$. For experiments using D9 sand, numerical simulations initially underestimate the wall velocity, Over time the numerically derived velocity for these experiments starts to overestimate the wall velocity by about $5\,\text{mm}\,\text{s}^{-1}$.

The discrepancy between simulations and experiment can be explained by several things:

- The lack of large slides observed in the numerical simulations. Particularly for experiments using the coarser D9 sand this effect is significant.

- The difference between wall height and angle. During the experiments the wall height reduces quicker than during the simulations, mostly due to less build up of sediment at the toe of the breach during simulations.

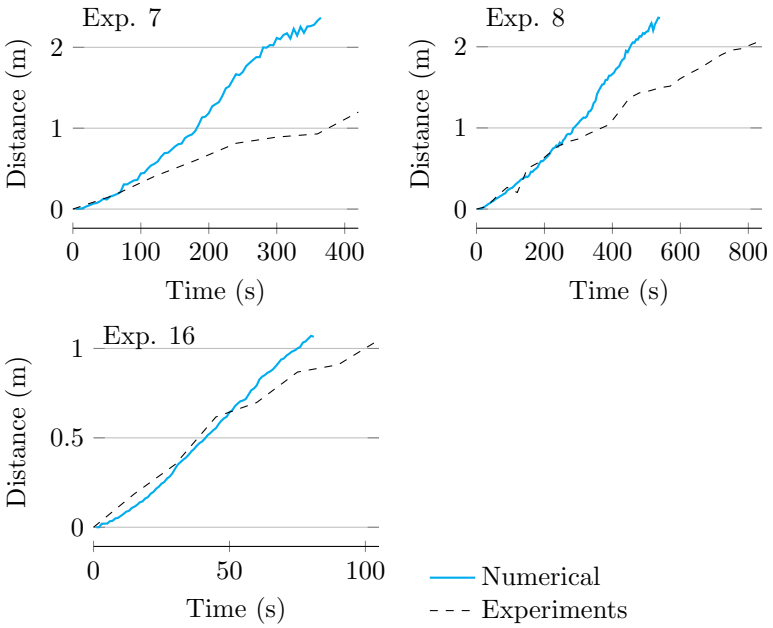

Figure 7.7: Comparison of numerical and experimental average x-coordinate for experiments 7, 8 and 16.

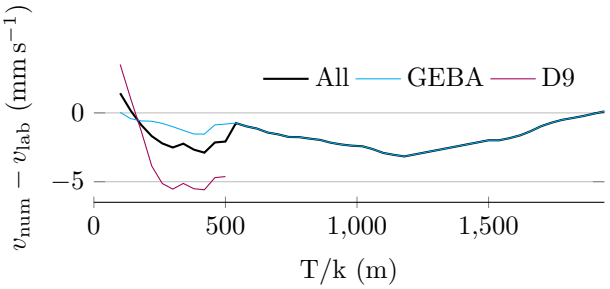

Figure 7.8: The mean difference between the wall velocity during numerical simulations and experiments, averaged over all experiments, plotted over time scaled with the initial permeability of the sand during the experiments. The wall velocities are averaged over $0.005/k_0$ (the time it takes to transverse 0.1 m if we assume $v_{\text{wall}} = 20k_0$).

Also the breach angle reduces quicker during experiments. This causes the wall velocity to reduce more quickly over time than seen during simulations.

- The rounding at the top of the breach wall during experiments. The transition from the breach wall to the top of the breach becomes smooth in the numerical experiments, while in the laboratory experiments a sharper transition can be seen. This effect causes an increase of the horizontal velocity near the top of the breach face. This also explains why the wall velocity increases over time for certain simulations (Figure 7.7).

7.2.3 Pore pressure

As in the experiments, during simulations the excess pore pressure peaks shortly after the start of the experiment, and then reduces over time (Figure 7.9). However, there is a discrepancy in the speed of this reduction. During numerical simulations the excess pore pressure reduces slower than during experiments. This can be partly explained by the difference in breach wall height during the experiments (breach walls reduce in height more quickly during experiments), as lower excess pore pressures are expected for smaller wall heights.

A difference is also found for the horizontal distribution of excess pore pressure (Figure 7.10). There is a initial negative pore pressure peak close to

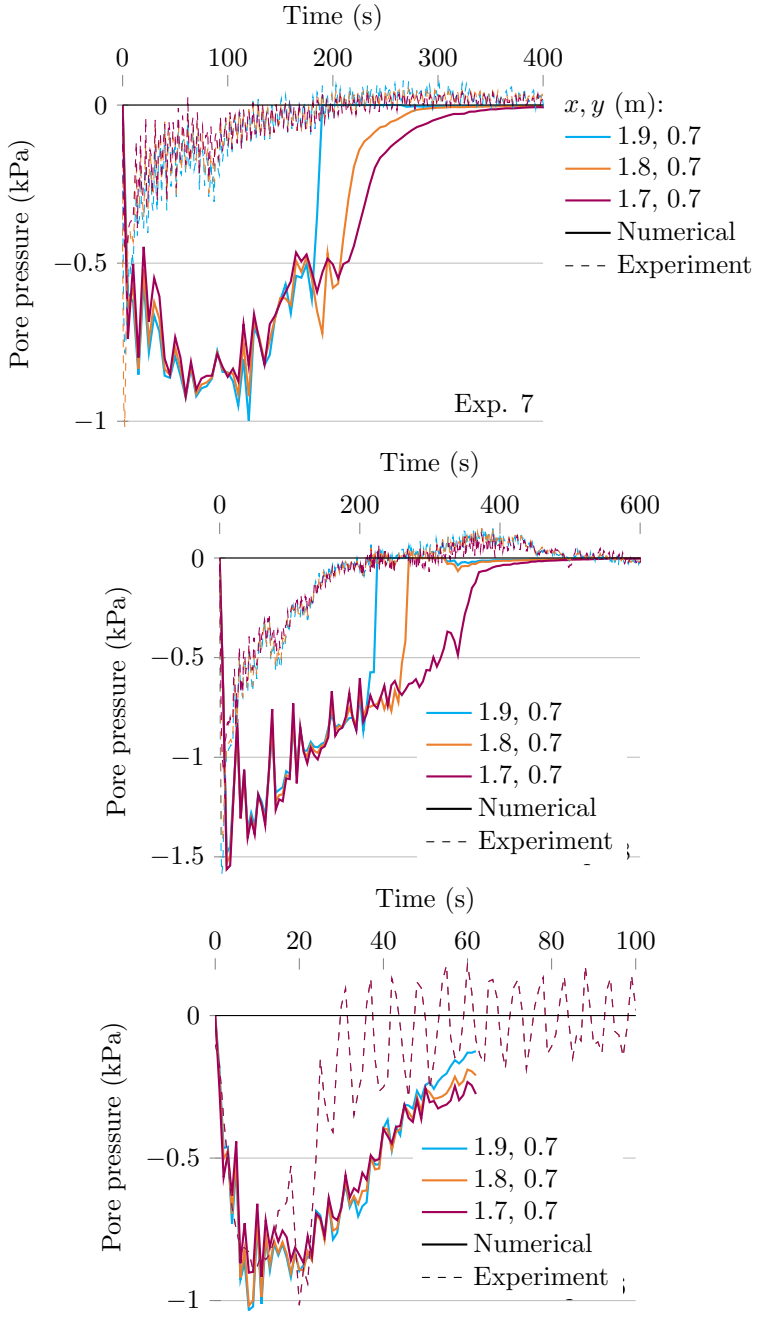

Figure 7.9: Comparison of numerical and experimental pore pressure measurements for experiment 7, 8, and 16

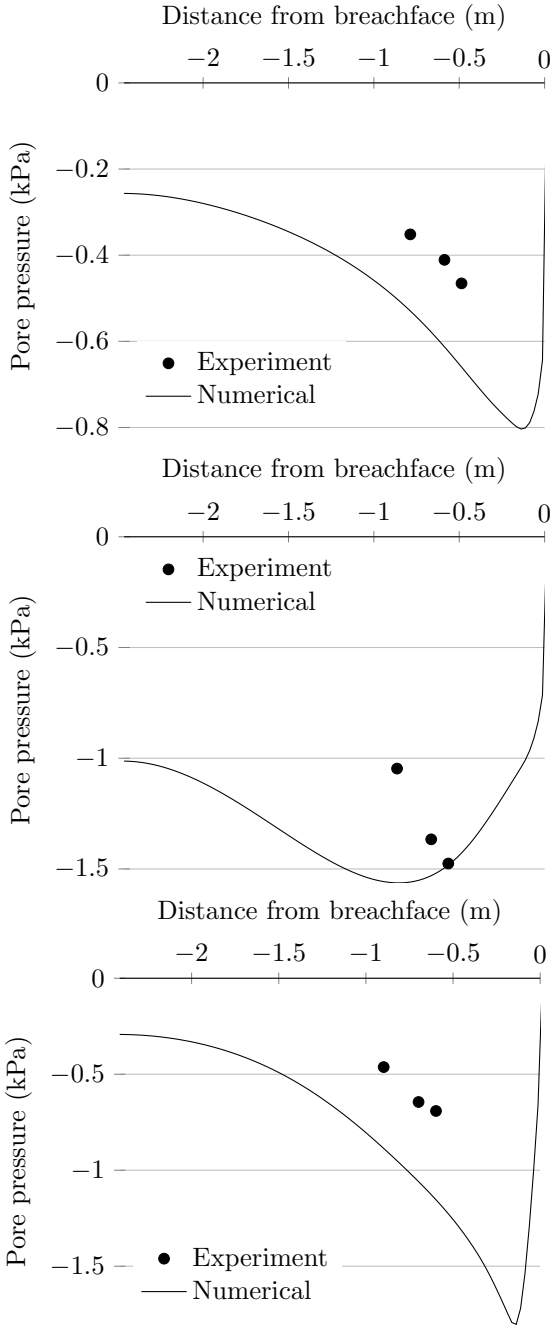

Figure 7.10: Comparison of numerical and experimental pore pressure measurements for experiment 7, 8, and 16, along a horizontal line at y = 0.7 m from the bottom of the tank, 15 seconds after lifting the door.

the breach face, just as during experiments. After this peak, the pore pressure increases, towards zero. During numerical simulations this rate of increase is slower than during experiments. For experiment 8, the numerical peak is also further away from the breach face than during the physical experiment. This can be explained by the regularization (Equation (5.17)). Regularization causes a small shear rate in non-yielded areas, and these small shears are still a source in the pore pressure equation (Equations (5.39) and (5.40)), thus causing larger excess pore pressure further away from the breach face, where the soil has not yet yielded.

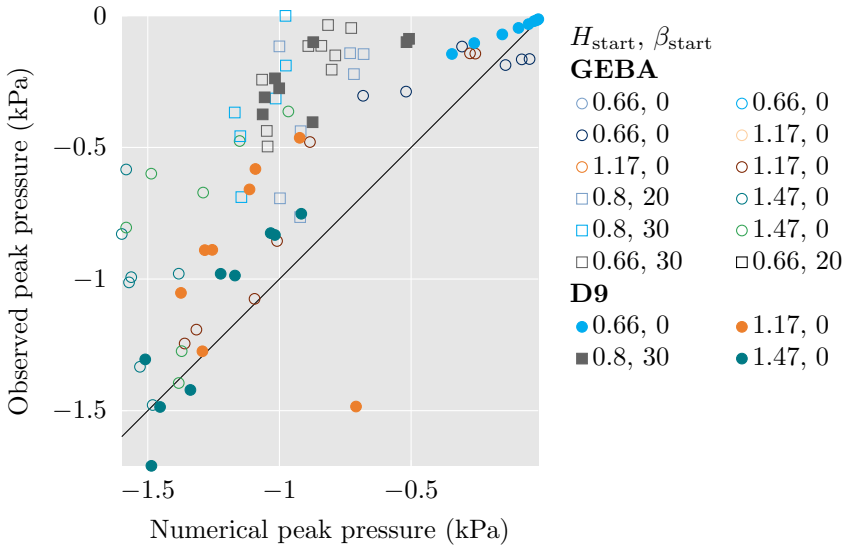

Figure 7.11: Comparison of numerical and experimental pore pressure peaks measured during experiments at various pressure probe locations. Results are grouped by experiment.

The excess pore pressure peaks over time, at a given fixed location, are similar in physical experiments and numerical simulations. In most cases, the peak is larger during numerical simulations. The largest discrepancies are seen for experiments with a slope on top of the breach.

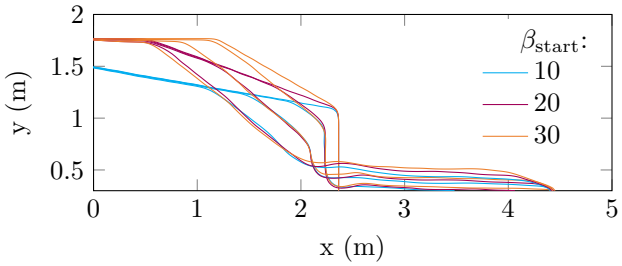

Figure 7.12: Profiles shown every 60 seconds, for simulations with a starting height of 0.8 m, and varying slope angles above the breach face, using GEBA sand properties.

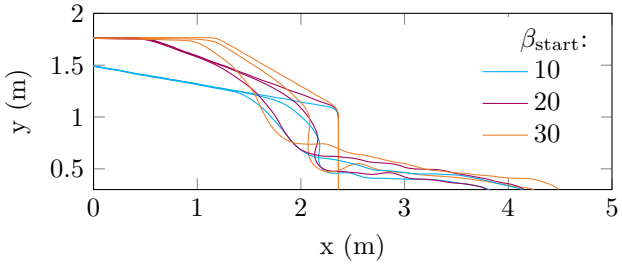

Figure 7.13: Profiles shown every 30 seconds, for simulations with a starting height of 0.8 m, and varying slope angles above the breach face, using D9 sand properties.

7.2.4 Breach stability

The stability of a breach is determined by the change of its wall height over time. A breach is considered unstable when the breach height increases over time, and stable when it decreases over time.

The stability is tested using simulations with a starting height of 0.8 m and a slope above the breach wall of 10°, 20°, and 30° for both GEBA and D9 sand. For simulations using the GEBA sand, the effect of the rounding of profiles near the top of the breach has a strong effect on the resulting profiles (Figure 7.12). As the slope above the breach wall steepens, the effect of the rounding increases. For simulations with the D9 sand this effect is smaller, likely because the speed of rounding is smaller relative to the larger wall velocity when using D9 sand.

When looking at the development of breach height over time (Figure 7.14), the expected trend is observed. Breaches with a steeper slope on top of the breach have a faster increase, or a slower decrease, of breach height over time. Unstable breaches, where the breach height increases over time, are observed for simulations with GEBA and slopes of 30° and 20°, and for the simulation using D9 with a slope of 30°.

The stability of the simulated breaches is less than observed during physical experiments. This is possibly caused by the slower built up of the slope at the toe of the breach during simulations, causing the bottom of the breach face to be lower than during physical experiments. Furthermore, the rounding of the profile observed during simulations likely plays a role as well.

7.3 Model sensitivity

7.3.1 Dilatancy factor

The dilatancy factor, C_{dil}, plays an important role (Equation (4.63)). It controls the ratio between shear velocity and dilation, with more dilation (with the same shear rate) for larger dilatancy factors. However, determining the appropriate value of C_{dil} is difficult. In this work a common value for C_{dil} is used, but the actual value remains unknown. Therefore, it is important to know the effects of changing this parameter. For experiments 8, and 16 the C_{dil} is varied between 1 and 16.

The dilatancy factor appears to have a strong effect on the rounding at the top of the breach face (Figures 7.15 and 7.16). As the dilatancy factor decreases, meaning more shearing is required to get the same amount of dilation, the rounding at the top of the breach wall increases.

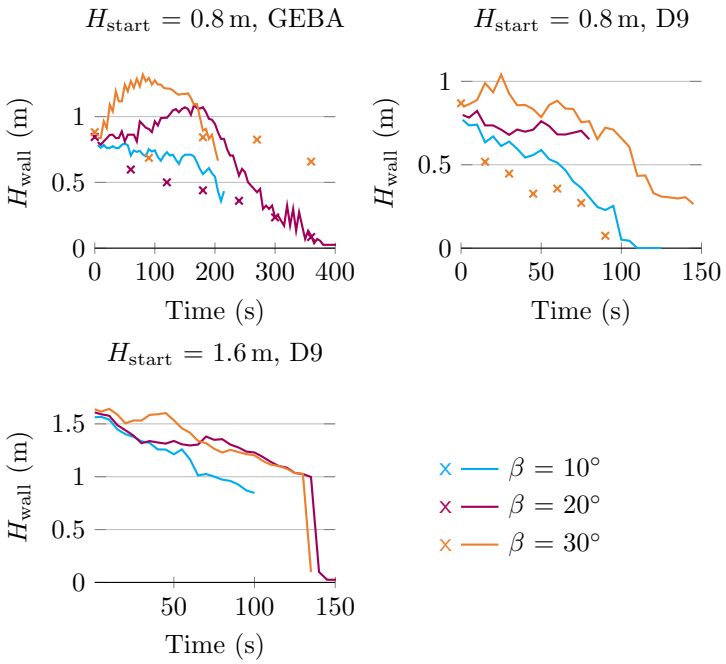

Figure 7.14: The breach height of different simulations over time, compared to physical experiments (indicated by x).

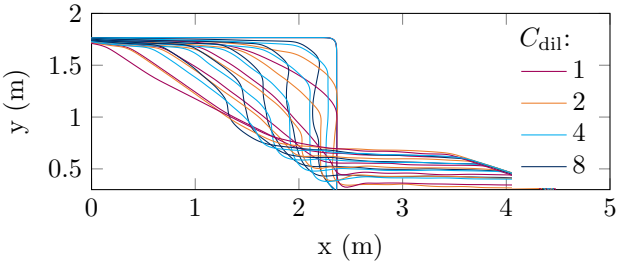

Figure 7.15: Profiles shown every 60 seconds, for simulations with a starting height of 1.47 m, and varying dilatancy factors, using GEBA sand properties.

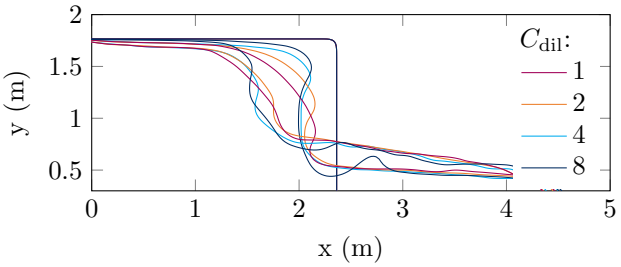

Figure 7.16: Profiles shown every 30 seconds, for simulations with a starting height of 0.8 m, and varying dilatancy factors, using D9 sand properties.

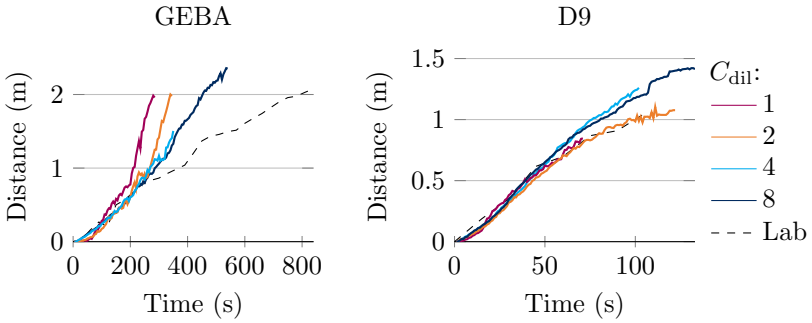

Figure 7.17: Comparison of the average x-coordinate of the breach wall for varying C_{dil}

The effect of the dilatancy factor on the wall velocity (Figure 7.17) is minimal when using the more permeable D9 sand. For simulations with GEBA sand there is a clear effect of C_{dil} on the wall velocity, with larger wall velocities for lower values of C_{dil}. When looking at the profiles (Figure 7.15), it seems that the differences in velocity are mostly caused by rounding at the top of the breach face.

There is also a strong effect of the dilatancy factor on the pore pressures, for the experiments with GEBA sand Figure 7.18. For the experiments with a C_{dil} of 1, or 2, The initial minimum of the pore pressure is doubled compared with the laboratory experiments, and the experiments with a C_{dil} of 4, or 8. As a higher value of C_{dil} means more dilatancy at the same shear rate, and thus lower pore pressure, these results are somewhat surprising. However, at the lower C_{dil}, the initial shear rate inside the sand also increased, causing the lower pore pressures. For the experiments with D9 sand, changing the C_{dil} has a minimal effect on the observed pore pressures.

Slides

One of the main purposes for developing the model was the incorporation of large slides, which could not be modelled with conventional models. However, while the model is able to simulate slides (Section 6.5), these were not observed during the simulations of the physical experiments. Simulations with varying C_{dil} show that formation of slides depends on this variable (Figure 7.19). As C_{dil} is reduced, the formation of a clear sliding wedge can be seen. This sliding wedge also explains the changing profiles for lower C_{dil} (Figure 7.16).

7.3.2 Equilibrium concentration

The equilibrium concentration, $\alpha_{\text{eq};0}$, controls the amount of dilation. In the current model is also assumed that concentration at which particles are released at the breach face (That is, the term $(1 - n_1)$ in Equation (2.28)). It is therefore expected that changing $\alpha_{\text{eq};0}$ will have significant effects on the breaching process. Because the equilibrium concentration (as well as n_1) are difficult to determine, it is important to understand their effect on the process. As expected, $\alpha_{\text{eq};0}$ controls the wall velocity, with the largest velocity observed for the highest equilibrium concentration (Figures 7.20 to 7.22).

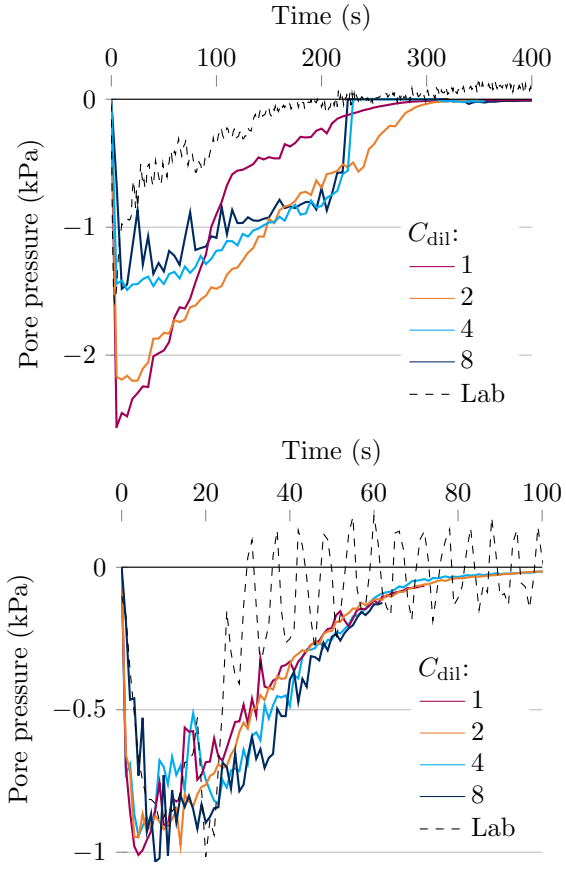

Figure 7.18: Excess pore pressure over time measured at $x = 1.9$, $y = 0.7$, for simulations with a starting height of 1.47 m, using GEBA sand (top) and D9 sand (bottom), using varying C_{dil}.

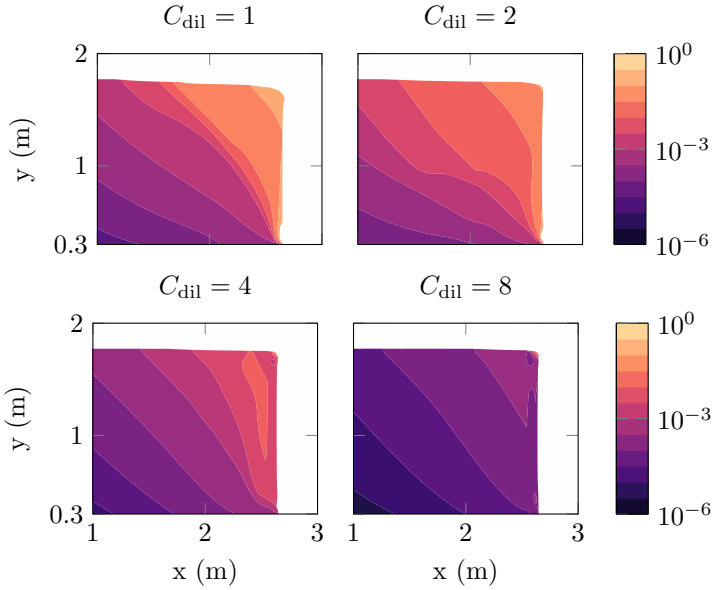

Figure 7.19: Velocity magnitudes inside the soil, 1 second after the start of a simulation, With a starting height of 1.47 m, using D9 sand, for varying dilation factors, C_{dil}. Only the relevant part of the domain is shown.

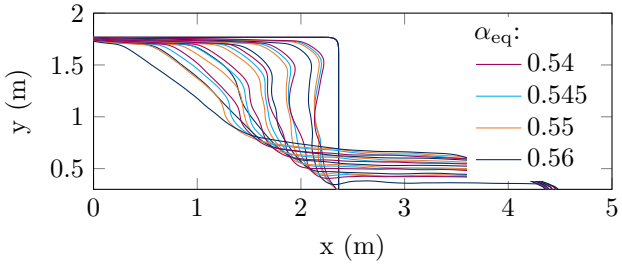

Figure 7.20: Profiles shown every 60 seconds, for simulations with a starting height of 1.47 m, and varying equilibrium concentrations, using GEBA sand properties.

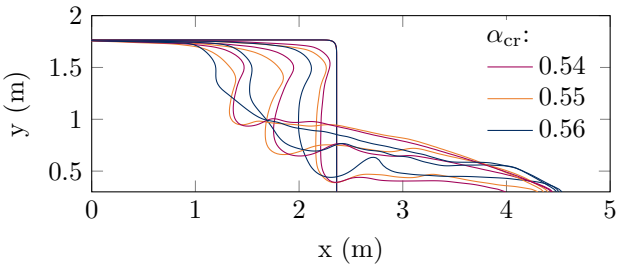

Figure 7.21: Profiles shown every 30 seconds, for simulations with a starting height of 0.8 m, and varying equilibrium concentrations, using D9 sand properties.

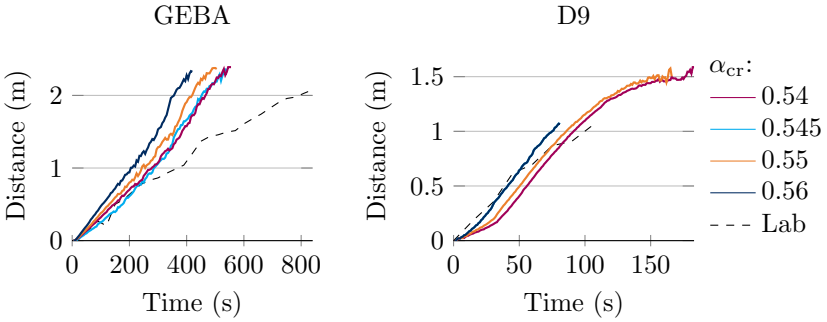

Figure 7.22: Comparison of the average x-coordinate of the breach wall for varying α_{eq}

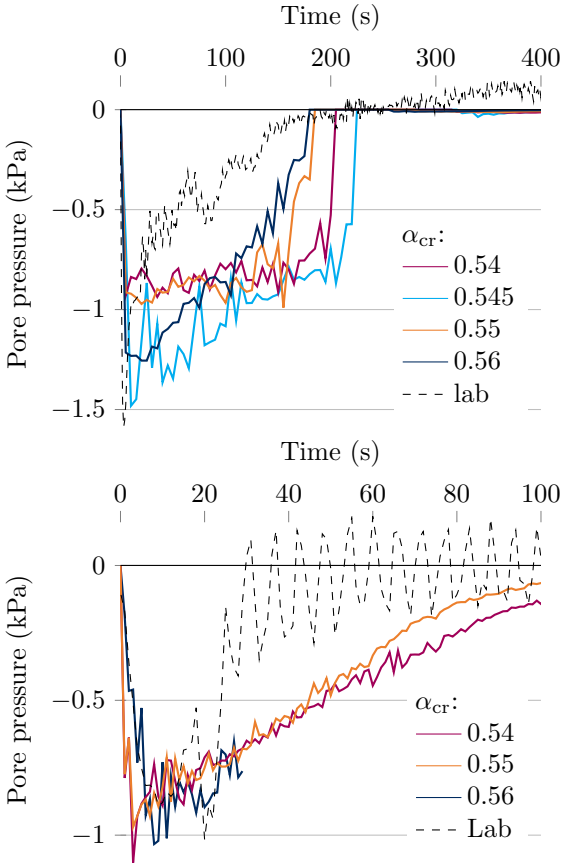

Figure 7.23: Excess pore pressure over time measured at $x = 1.9$, $y = 0.7$, for simulations with a starting height of 1.47 m, using GEBA sand (top) and D9 sand (bottom), using varying α_{eq}.

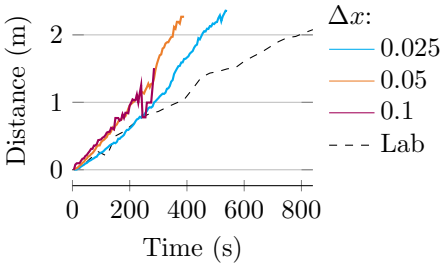

Figure 7.24: Comparison of the average x-coordinate of the breach wall for varying grid size.

7.3.3 Grid dependence

The amount rounding observed at the top of the breach wall depends on the size of the grid size, with more rounding observed for larger grid cells (Figure 7.26). This also causes a small increase in wall velocity as grid cells become larger (Figure 7.24). There is also an increase in pore pressure observed for an increase in grid cell size, with the pore pressures closest to the measured values for the smallest grid cells (Figure 7.25).

7.3.4 Starting height

Increasing the starting height leads to an increased peak of the excess pore pressure (Figure 7.27). For a starting height of 2 m or higher, an increased erosion along the breach wall is observed (Figure 7.28). This increased erosion leads to an increasing wall velocity compared to breaches with a lower starting height. It was expected that shear slides would play a larger role at larger starting heights, however, the current simulations do not show this effect.

7.3.5 3D effects

Until now, all simulations have been two-dimensional. To study the effects of this simplification, experiment 8 has been simulated using a three-dimensional domain, with a domain width of 0.5 m, as well. A cell size of 0.05 m × 0.05 m was used, and a no-slip boundary was used at the side walls.

There is an observable difference between the three- and two-dimensional simulations. The three-dimensional simulation shows less rounding near the top of the domain, as well as steeper breach walls (Figure 7.29). The 3D

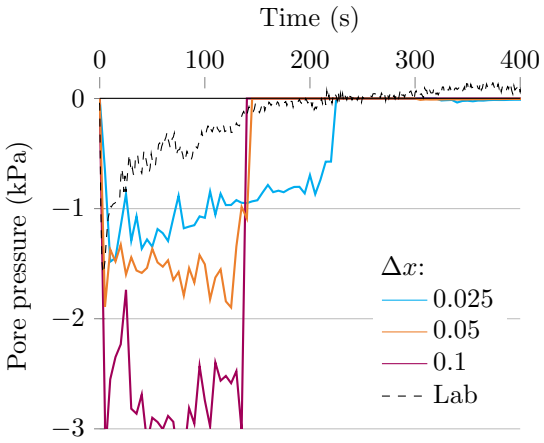

Figure 7.25: Excess pore pressure over time measured at $x = 1.9$, $y = 0.7$, for simulations with a starting height of 1.47 m, using GEBA sand, using varying grid sizes.

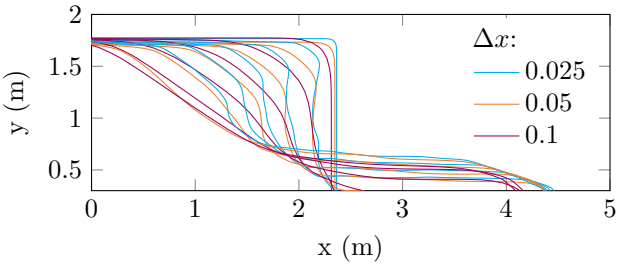

Figure 7.26: Profiles shown every 60 seconds, for simulations with a starting height of 1.47 m, using GEBA sand properties, and varying grid sizes.

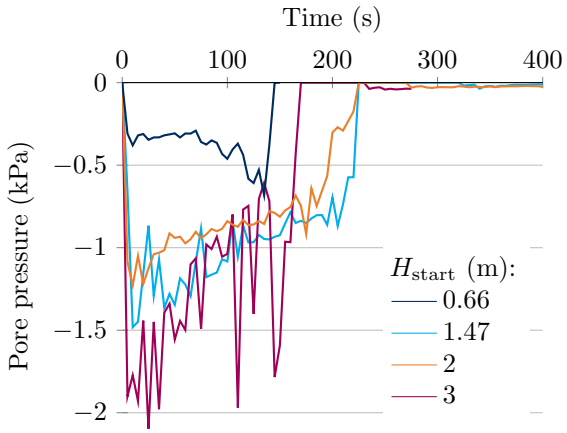

Figure 7.27: Excess pore pressure over time measured at $x = 1.9$, $y = 0.7$, for simulations with varying starting heights, using GEBA sand.

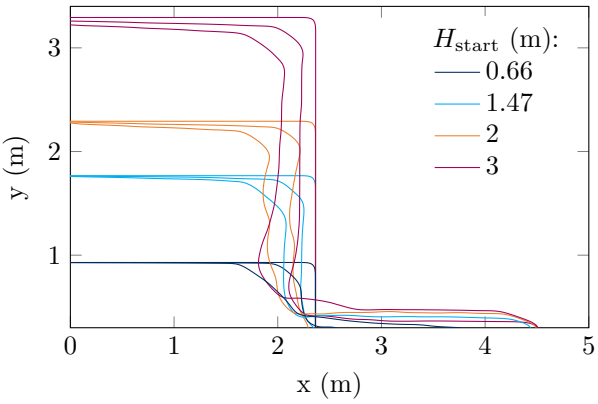

Figure 7.28: Profiles shown every 60 seconds, for simulations with varying starting heights, using GEBA sand.

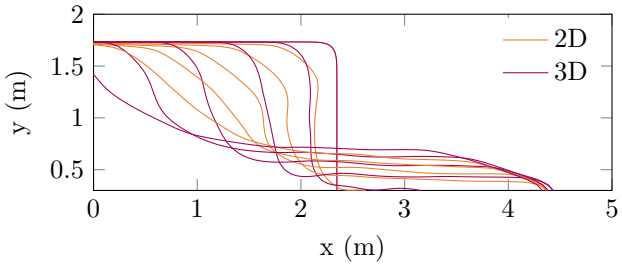

Figure 7.29: Profiles shown every 60 seconds, for simulations with a starting height of 1.47 m, using GEBA sand, along the centreline for a 2D and a 3D simulation.

simulations also has larger wall velocities (Figure 7.30), possibly caused by the steeper breach faces.

The excess pore pressures observed during the 3D simulations are larger than during the 2D simulations. This is likely due to the no-slip boundary applied at the sides in the 3D case. Because of the no-slip boundary, larger shear rates are observed here, causing an increase in dilatancy, and thus increased pore pressure as well. The different pore pressure distributions will also affect the breach profiles and wall velocities. Results also show that there is no big difference between pore pressures measured at the centre of the domain (at z = 0.25 m), or along the side of the domain (at z= 0 m).

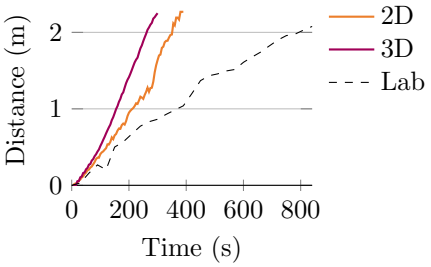

Figure 7.30: Comparison of the average x coordinate of the breach wall, for a 2D and a 3D simulation.

To further test the 3D capabilities of the model, a final, three-dimensional simulation is carried out. In a domain 3 m long, 2 m wide, and 1 m high, a

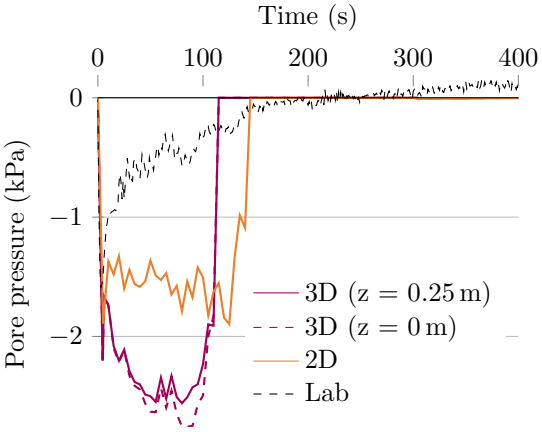

Figure 7.31: Excess pore pressure over time measured at $x = 1.9$, $y = 0.7$, for a 2D and a 3D simulation.

0.5 m high, 1:2 slope is created. Out of this slope a 0.3 m × 0.6 m block of soil is removed to initiate breaching (Figure 7.32). D9 sand properties were used. A cell size of 0.05 m × 0.05 m was used, with no-slip boundaries was used at all walls.

At the start of the simulation, the breach spreads out radially from the initial position (Figure 7.33). After about 30 seconds, the breach covers the complete width of the domain, and continues breaching in the x-direction. After about 55 seconds the breaching process stops, and during the next 65 seconds most sediment released during the breaching process settles.

7.4 Concluding remarks

In this chapter the created model has been applied to the breaching experiments of Chapter 3. Results show that the model is able to numerically reproduce breaching behaviour. A steep breach wall is formed, with particles releasing slowly from the breach face, instead of a big slide. As sediment is released at the breach face, the breach face moves horizontally with a velocity similar to that observed in physical experiments. As the experiment progresses, the breach wall diminishes in size and becomes less steep. Furthermore, as observed during physical experiments, the excess pore pressure is the lowest just after the starting the experiment. The excess pore pressure then

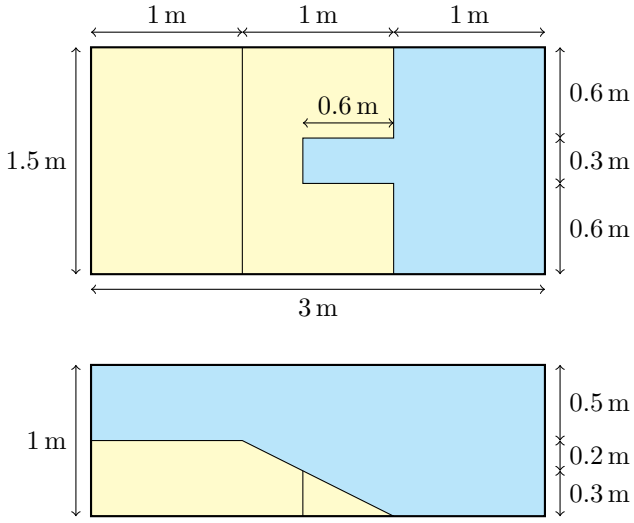

Figure 7.32: Initial set-up of the 3D simulation.

slowly converges to 0 Pa over time. The model is also able to simulate both stable (Breach height diminishes over time) as well as stable (Breach height increases over time) breaches.

However, comparing numerical results to physical experiments also reveals several differences:

- The buildup of a slope at the toe of the breach is slower during simulations than observed in experiments. This causes the breach height to reduce slower in simulations, compared to experiments. Thus, unstable breaching becomes more likely. It also causes stable breaches to travel further horizontally.

- In the simulations, during breaching, there is strong rounding of the profile near the top of the breach wall. This rounding is not observed during experiments. This is particularly troublesome during experiments with a slope above the wall, where this effect is even larger. This also causes breaches to travel further horizontally. This is probably due to shear deformations in the model, which are either not observed during experiments, or would lead to small shear slides in experiments.

- For the experiment with D9 sand (Figure 7.6), the breach wall advances

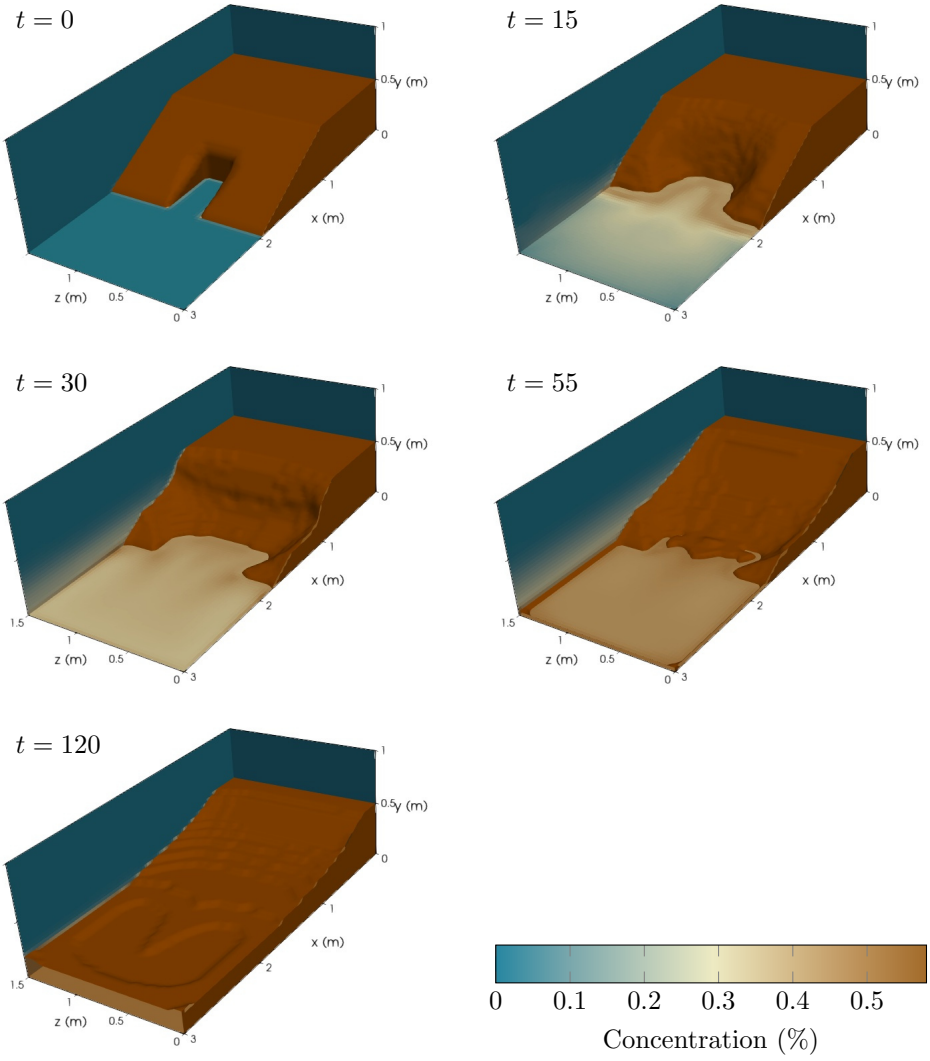

Figure 7.33: results of the 3D simulation. Sidewalls are coloured according to the sand concentration. And the soil is shown by a brown surface.

faster initially in experiments. This is likely caused because large slides observed at the start of these experiments are not observed in simulations. These slides have a large contribution to the wall velocity at the start of experiments.

- For experiments with GEBA sand, the wall velocity at the start of the experiment is similar to that observed during physical experiments. However, over time a discrepancy between observed and simulated wall velocity emerges, with larger velocities during simulations. This can be linked to the breach height reducing more slowly compared to experiments, and to the rounding observed during simulations.

- The observed excess pore pressure peak, at the start of the experiments are similar in the simulations and physical experiments. However, the rate at which the pore pressure reduces is slower during simulations. This can be caused by the slower reduction in breach height. However, a slower reduction is also observed spatially, with a slower decrease in pore pressures further away from the breach face for simulations. This can be caused by the use of regularization. During simulations, in quasi-static areas where no shearing should occur, there is still some shear when applying regularization. Therefore, there is still a source of dilation, and thus excess pore pressure, in these regions, where there should be none. This can cause the higher excess pore pressures further away from the breach face.

- Shear slides, like observed during the physical experiments, do not appear in the simulations, unless C_{dil} is lowered. This can partly explain why the build-up of sediment at the toe of the breach is smaller during simulations, as after large shear slides, large parts of the slides remain in front of the breach face. A possible reason for the lack of slides is a too high C_{dil}, but can also be caused by excess pore pressures being too large, and thus making the soil stabler than in reality. One reason shear slides are observed less than during experiments, is that during experiments a very narrow internal shear surface forms for slides. Due to the chosen numerical approach, in the model the shearing is spread over a larger area, thus changing the behaviour of the soil.

Simulations show that results depend heavily on the values used for the dilation factor, C_{dil}, and the equilibrium concentration α_{eq}. α_{eq} has a strong effect on the wall velocity, with larger velocities for larger equilibrium concentrations, while C_{dil} has a strong effect on the shape of the profile over time,

with more rounding for smaller dilation factors. Finally, simulations show the effects of simulating in two or three dimensions, and the effects of no-slip boundaries at the sides of the breach.

Finally we have shown that the model is able to model three dimensional breaches. Three dimensional aspects of the model need to be validated as well. For this three dimensional validation material needs to be generated.

Chapter 8

Conclusions and Recommendations

As stated in the introduction, the goal of this dissertation was to answer the following question

How can we improve the prediction of the (unstable) breaching process?

with the following two sub-questions

What is the effect of increasing breach height on the breaching process?

How does changing from a two-dimensional to a three-dimensional setup affect the breaching process?

8.1 Conclusions

8.1.1 Breach height effects

During laboratory experiments, a correlation between breach height and wall velocity was found, with larger velocities as breach height increases. This effect is not included in the standard wall velocity equation Equation (2.28).

Interestingly, the breach height does not affect the contribution of shear slides significantly, nor do shear slides increase the total wall velocity.

Instead, increased wall velocities can be explained by increased erosion by the turbidity current, due to increased sand production. Numerical experiments with increasing wall heights support this theory.

Numerical experiments also show a strong link between the wall height and the measured negative pore pressure peak, with more negative pore pressure as wall height increases.

As predicted by the equations, the stability of a breach decreases as breach height increases.

8.1.2 3D effects

The numerical model is suitable to model the breaching process in both 2D and 3D. The model can be a helpful tool in gaining better understanding of the effects of three dimensionality.

There are clear effects when switching to three dimensional simulations. In 3D an initially small disturbance spreads in multiple directions. This leads to a greater increase in breach surface over time than during two dimensional experiments. This leads to a greater increase in sand production, and will affect settling of the sand at the toe, and could thus lead to less stable breaches.

8.1.3 Predicting stability

Experiments show that the equations commonly used to predict the wall velocity (Equation (2.28)), and the slope angle at the toe of the breach (From Mastbergen et al. (1988), Equation (2.30)), correspond well with values measured during experiments.

Predicting the stability of a breach, by combining these two equations (Equation (2.69)) proves more difficult, the chance of a stable breach is underestimated. In some cases a breach turns out to be stable when the equations predict an unstable breach. The equations can thus be used as a conservative

estimate of breach stability, although this has not yet been tested in three dimensional cases.

The numerical model, modelling the frictional regime, where grains are in constant contact with each other, as a fluid with a yield stress, can reproduce breaching behaviour. The model is also able to simulate both stable (breach height diminishes over time) as well as unstable (breach height increases over time) breaches.

However, there are still several important differences between model and physical experiment. First, there is a slower buildup of sediment at the toe of the breach, causing milder slopes, and a slower reduction of the breach height over time. Second, there is rounding of the profile seen at the top of the breach face, which is not observed during experiments. Third, while initially the wall velocity corresponds with measurements from experiments, over time numerical wall velocities become larger than the experimentally measured velocities. Fourth, the reduction of excess pore pressure is slower in both space and time compared to experiments. Finally, the shear slides observed during experiments, are not seen during most simulations. Thus, the numerical in its current state should not be used to predict the stability of a breach, until the model has been developed further.

8.1.4 Other conclusions

There is a large contribution of shear slides to the total sand flux from the breach, when the breach face is steep. The amount of slides also correlates strongly with the permeability of the sand. The contribution of shear slides to the total sand flux went up from 10% to 80% when the permeability increased by a factor of just 2.3.

Shear slides were observed mostly at the start of the experiments. This is likely because the breach face is the steepest at the start of the experiments, and reduces over time, leading to a smaller resisting force needed to stabilize the slope. However, it is also possible that other factors (for example, the effects of lifting the removable gate at the start of the experiment) cause the increase in slides at the start of the experiment. To test this hypothesis, experiments with different initial slopes of the breach face should be carried out.

The dilation factor and the equilibrium concentration have a significant effect on the results. When varying the dilatancy factor, which controls the relation between shear rate and dilation rate, shear slides appear only for lower dilatancy factors. This indicates that by calibrating the dilatancy factor, the shear slides can be modelled. However, lowering the dilatancy factor also

influences the wall velocity and excess pore pressure. It is also possible that the lifting of the removable gate at the start of the experiments, which is not modelled, influences the amount of slides.

8.2 Recommendations

8.2.1 Laboratory experiments

During the experiments only two types of sand were investigated. Repeating the experiments with more kinds of sand will likely give a better insight into the effects of different sand properties on the breaching process.

The experiments always started with a flat bed at the toe of the breach. It will be interesting to see how starting with different slopes angles affects the results. It is interesting to see what happens to slope when a slope equal to or larger than the expected equilibrium slope is applied at the toe.

The initial slope of the breach face was fixed 90°. Varying the initial slope angle should give interesting insights. This can also confirm the importance of the slope of the breach face on the formation of shear slides during the experiments.

Most large slides occur at the start of experiments, right after the gate has been lifted. It is expected that this is because the breach wall is the steepest at the start of the experiment, but lifting the gate could also influence the amount of slides. Therefore it might be worthwhile to investigate the breaching process with different starting mechanisms.

Finally, it is recommended to design and carry out three dimensional experiments, which can act as validation material for the three dimensional model.

8.2.2 Numerical method

The dilation factor C_{dil}, which controls the ratio between shear rate and dilation rate, has a significant effect on the results. Therefore, it is recommended to develop methods for determining this factor for different sand types. The method of Pailha and Pouliquen (2009) could be applied. They looked at the slope angle where motion was initiated, for varying initial sand concentrations. It is also worthwhile to investigate the relation between C_{dil} and other variables like the shear rate, $\dot{\gamma}$, and the effective pressure, p_{eff}.

In the current model, only a single fraction of sand, with a single grain diameter is used. In reality, sands have a large range of different grain diameters. This has a large effect, for example, on the settling velocity of the

sediment, as larger grains settle faster. This effect can be seen clearly when the settling in the model is compared to experiments. Due to the variety of grain diameters, there is a spread in fall velocities not seen in the model. Therefore, it is recommended to include multiple fractions in the model.

In the current model, the pick-up flux equation of van Rijn (1984), combined with the retarded erosion correction of van Rhee (2010), is used. However, there are several pick-up flux equations available. It is recommended investigate different equations, and chose the equation which fits the problem best.

The model has been used to simulate 2D cases, or 3D cases with limited widths. It would be interesting to see what happens during 3D simulations with a wider domain, as this would come closer to breach failures observed in nature.

Shear slides, as observed during physical experiments, were not seen in most simulations. While it is expected that slides can be simulated if the correct variables are used, it is worth investigating different methods of simulating the sand in the frictional regime.

Bibliography

Allouche, M., I. A. Frigaard, and G. Sona (2000). "Static wall layers in the displacement of two visco-plastic fluids in a plane channel". In: *Journal of Fluid Mechanics* 424, pp. 243–277. DOI: 10.1017/S0022112000001956.

Alonso, E., A. Yerro, and N. Pinyol (2015). "Recent developments of the Material Point Method for the simulation of landslides". In: *IOP Conference Series: Earth and Environmental Science* 26.1, p. 012003. DOI: 10.1088/1755-1315/26/1/012003.

Bagnold, R. (1954). "Experiments on a gravity-free dispersion of large solid spheres in a Newtonian fluid under shear". In: *Proceedings of the Royal Society of London A: Mathematical, Physical and Engineering Sciences* 225.1160, pp. 49–63. DOI: 10.1098/rspa.1954.0186.

Bandara, S. and K. Soga (2015). "Coupling of soil deformation and pore fluid flow using material point method". In: *Computers and Geotechnics* 63, pp. 199–214.

Been, K., M. G. Jefferies, and J. Hachey (1991). "The critical state of sands". In: *Géotechnique* 41.3, pp. 365–381. DOI: 10.1680/geot.1991.41.3.365.

Beinssen, K., D. Neil, and D. Mastbergen (2014). "Field observations of retrogressive breach failures at two tidal inlets in Queensland, Australia". In: *Australian Geomechanics* 49.3, pp. 55–64.

Bercovier, M. and M. Engelman (1980). "A finite-element method for incompressible non-Newtonian flows". In: *Journal of Computational Physics* 36.3, pp. 313–326. DOI: 10.1016/0021-9991(80)90163-1.

Bisschop, F. (2018). "Erosion of Sand at High Flow Velocities: An Experimental Study". PhD. Delft University of Technology.

Bisschop, F., P. J. Visser, C. van Rhee, and H. J. Verhagen (2010). "Erosion due to high flow velocities: a description of relevant processes". In: *Coastal Engineering*. Vol. 1. 32, pp. 1–10. DOI: 10.9753/icce.v32.sediment.24.

Boyer, F., E. Guazzelli, and O. Pouliquen (Oct. 2011). "Unifying Suspension and Granular Rheology". In: *Physical Review Letters* 107 (18), p. 188301. DOI: 10.1103/PhysRevLett.107.188301.

Brennan, D. (2001). "The numerical simulation of two phase flows in settling tanks". PhD thesis. Imperial College London (University of London).

Breusers, H. N. C. (Dec. 1974). "Suction of sand". In: *Bulletin of the International Association of Engineering Geology - Bulletin de l'Association Internationale de Géologie de l'Ingénieur* 10.1, pp. 65–66. DOI: 10.1007/BF02634636.

Breusers, H. N. C. (1977). "Hydraulic excavation of sand". In: *Proceedings International Course in Modern dreding*.

Burgos, G. R., A. N. Alexandrou, and V. Entov (1999). "On the determination of yield surfaces in Herschel–Bulkley fluids". In: *Journal of Rheology* 43.3, pp. 463–483. DOI: 10.1122/1.550992.

Caldwell, W. K. (1966). *Verification of empirical method for determining riverbank stability, 1964 data*. Technical Report. U.S. Army Engineer Waterways Experiment Station.

Carman, P. (1937). "Fluid flow through granular beds". In: *Chemical Engineering Research and Design* 75, S32–S48. DOI: 10.1016/S0263-8762(97)80003-2.

Cassar, C., M. Nicolas, and O. Pouliquen (2005). "Submarine granular flows down inclined planes". In: *Physics of fluids* 17, p. 103301. DOI: 10.1063/1.2069864.

Ceccato, F. (2015). "Study of large deformation geomechanical problems with the Material Point Method". PhD thesis. Università degli Studi di Padova.

Chatzimina, M., C. Xenophontos, G. C. Georgiou, I. Argyropaidas, and E. Mitsoulis (2007). "Cessation of annular Poiseuille flows of Bingham plastics". In: *Journal of Non-Newtonian Fluid Mechanics* 142.1. Viscoplastic fluids: From theory to application, pp. 135–142. DOI: 10.1016/j.jnnfm.2006.07.002.

Clift, R., J. R. Grace, and M. E. Weber (2005). *Bubbles, drops, and particles*. Courier Corporation.

Comte-Bellot, G. and S. Corrsin (1966). "The use of a contraction to improve the isotropy of grid-generated turbulence". In: *Journal of Fluid Mechanics* 25.4, pp. 657–682. DOI: 10.1017/S0022112066000338.

Courrech du Pont, S., P. Gondret, B. Perrin, and M. Rabaud (Jan. 2003). "Granular Avalanches in Fluids". In: *Physical Review Letters* 90 (4), p. 044301. DOI: 10.1103/PhysRevLett.90.044301.

Crowe, C. T., J. D. Schwarzkopf, M. Sommerfeld, and Y. Tsuji (2011). *Multiphase flows with droplets and particles*. CRC press.

Darcy, H. (1856). *Les fontaines publiques de la ville de Dijon.*

De Groot, M. and D. Mastbergen (2008). *Inscharing Hooidijk februari 2008, Verklaring en herstel.* 418361-0012. Deltares.

De Josselin De Jong, G. (1980). "Application of the calculus of variations to the vertical cut off cohesive frictionless soil". In: *Geotechnique* 30.1, pp. 1–16. DOI: 10.1680/geot.1980.30.1.1.

de Wit, L. (2010). "Near field 3D CFD modelling of overflow plumes". In: *Proceedings of the 19th World Dredging Conference (WODCON XIX), Beijing, China*, pp. 9–14.

Delft Hydraulics (1972). "Systematic investigation of two-dimensional and three-dimensional scour". In: M648 M.

Doppler, D., P. Gondret, T. Loiseleux, S. Meyer, and M. Rabaud (2007). "Relaxation dynamics of water-immersed granular avalanches". In: *Journal of Fluid Mechanics* 577.1, pp. 161–181. DOI: 10.1017/S0022112007004697.

Durst, F., D. Miloievic, and B. Schönung (1984). "Eulerian and Lagrangian predictions of particulate two-phase flows: a numerical study". In: *Applied Mathematical Modelling* 8.2, pp. 101–115. DOI: 10.1016/0307-904X(84)90062-3.

Einstein, A. (1906). "Eine neue Bestimmung der Moleküldimensionen". In: *Annalen der Physik* 324.2, pp. 289–306. DOI: 10.1002/andp.19063240204.

Eke, E., E. Viparelli, and G. Parker (2011). "Field-scale numerical modeling of breaching as a mechanism for generating continuous turbidity currents". In: *Geosphere*, pp. 1063–1076. DOI: 10.1130/GES00607.1.

Fellenius, W. K. A. (1948). *Erdstatische Berechnungen: Mit Reibung und Kohäsion (Adhäsion) und Unter Annahme Kreiszylindrisher Gleitflächen.* 53. W. Ernst.

Fernandez Luque, R. and R. Van Beek (1976). "Erosion and transport of bedload sediment". In: *Journal of hydraulic research* 14.2, pp. 127–144. DOI: 10.1080/00221687609499677.

Fox, R. O. (2012). "Large-Eddy-Simulation Tools for Multiphase Flows". In: *Annual Review of Fluid Mechanics* 44.1, pp. 47–76. DOI: 10.1146/annurev-fluid-120710-101118.

Garside, J. and M. R. Al-Dibouni (1977). "Velocity-voidage relationships for fluidization and sedimentation in solid-liquid systems". In: *Industrial & engineering chemistry process design and development* 16.2, pp. 206–214. DOI: 10.1021/i260062a008.

GDR MiDi (2004). "On dense granular flows". In: *European Physical Journal E* 14, pp. 341–365.

George, W. K. (Mar. 2007). "Is there a universal log law for turbulent wall-bounded flows?" In: *Philosophical Transactions of the Royal Society A:*

Mathematical, Physical and Engineering Sciences 365.1852, pp. 789–806. DOI: 10.1098/rsta.2006.1941.

Goeree, J. C., G. H. Keetels, E. A. Munts, H. H. Bugdayci, and C. van Rhee (2016). "Concentration and velocity profiles of sediment-water mixtures using the drift flux model". In: *The Canadian Journal of Chemical Engineering* 94.6, pp. 1048–1058. DOI: 10.1002/cjce.22491.

Goeree, J. C. (2018). "Drift-flux modeling of hyper-concentrated solid-liquid flows in dredging applications". PhD thesis. Delft University of Technology. DOI: 10.4233/uuid:2d432d11-cce4-40de-b951-e89dfebbef27.

Graf, W. H. and G. Pazis (1977). "Desposition and erosion in an alluvial channel". In: *Journal of Hydraulic Research* 15.2, pp. 151–166. DOI: 10.1080/00221687709499653.

Greenshields, C. (n.d.). *OpenFOAM — Free CFD Software — The OpenFOAM Foundation*. http://www.openfoam.org. Accessed 27 january 2017.

Hölzer, A. and M. Sommerfeld (2008). "New simple correlation formula for the drag coefficient of non-spherical particles". In: *Powder Technology* 184.3, pp. 361–365. DOI: 10.1016/j.powtec.2007.08.021.

Hvorslev, M. J. (1949). *Subsurface exploration and sampling of soils for civil engineering purposes*. Technical Report. U.S. Army Engineer Waterways Experiment Station.

Ishii, M. and T. Hibiki (2011). *Thermo-fluid dynamics of two-phase flow*. Springer Science+ Business Media.

Issa, R., B. Ahmadi-Befrui, K. Beshay, and A. Gosman (1991). "Solution of the implicitly discretised reacting flow equations by operator-splitting". In: *Journal of Computational Physics* 93.2, pp. 388–410. DOI: 10.1016/0021-9991(91)90191-M.

Iverson, R. M. (2013). "Mechanics of Debris Flows and Rock Avalanches". In: *Handbook of Environmental Fluid Dynamics*. Ed. by H. J. S. Fernando. Boca Raton: Taylor & Francis, pp. 573–587.

Jasak, H. (1996). "Error Analysis and Estimation for Finite Volume Method with Applications to Fluid Flows". PhD thesis. Imperial College London (University of London).

Johansen, S., N. Anderson, and S. de Silva (1990). "A two-phase model for particle local equilibrium applied to air classification of powders". In: *Powder Technology* 63.2, pp. 121–132. DOI: 10.1016/0032-5910(90)80034-V.

Jop, P., Y. Forterre, and O. Pouliquen (2006). "A constitutive law for dense granular flows". In: *Nature* 441.7094, pp. 727–730. DOI: 10.1038/nature04801.

Jop, P. (2008). "Hydrodynamic modeling of granular flows in a modified Couette cell". In: *Physical Review E* 77.3, p. 032301. DOI: 10.1103/PhysRevE.77.032301.

Kármán, T. V. (1930). "Mechanische Ähnlichkeit und Turbulenz". In: *Nachrichten von der Gesellschaft der Wissenchaften zu Göttingen*.

Kawanisi, K. and R. Shiozaki (2008). "Turbulent Effects on the Settling Velocity of Suspended Sediment". In: *Journal of Hydraulic Engineering* 134.2, pp. 261–266. DOI: 10.1061/(ASCE)0733-9429(2008)134:2(261).

Klebanoff, P. S. (1955). *Characteristics of turbulence in a boundary layer with zero pressure gradient*. Tech. rep. National Bureau Of Standards Gaithersburg, MD.

Lagrée, P., L. Staron, and S. Popinet (2011). "The granular column collapse as a continuum: validity of a two-dimensional Navier–Stokes model with a μ (i)-rheology". In: *Journal of Fluid Mechanics* 686.1, pp. 378–408. DOI: 10.1017/jfm.2011.335.

Lalli, F. and A. Di Mascio (1997). "A numerical model for fluid-particle flows". In: *International Journal of Offshore and Polar Engineering*.

Lalli, F., P. Esposito, R. Piscopia, and R. Verzicco (2005). "Fluid–particle flow simulation by averaged continuous model". In: *Computers & fluids* 34.9, pp. 1040–1061.

Launder, B. and D. Spalding (1974). "The numerical computation of turbulent flows". In: *Computer Methods in Applied Mechanics and Engineering* 3.2, pp. 269–289. DOI: 10.1016/0045-7825(74)90029-2.

Launder, B. E. and D. B. Spalding (1983). "The numerical computation of turbulent flows". In: *Numerical Prediction of Flow, Heat Transfer, Turbulence and Combustion*. Elsevier, pp. 96–116. DOI: 10.1016/B978-0-08-030937-8.50016-7.

Maele, K. V. and B. Merci (2006). "Application of two buoyancy-modified k–epsilon turbulence models to different types of buoyant plumes". In: *Fire Safety Journal* 41.2, pp. 122–138. DOI: 10.1016/j.firesaf.2005.11.003.

Manninen, D., V. Taivassalo, and S. Kallio (1996). *On the mixture model for multiphase flow*. Tech. rep. Technical Research Centre of Finland.

Mastbergen, D. R. and J. Van Den Berg (2003). "Breaching in fine sands and the generation of sustained turbidity currents in submarine canyons". In: *Sedimentology*, pp. 625–637. DOI: 10.1046/j.1365-3091.2003.00554.x.

Mastbergen, D. (2001). *Analyse inbressingen zandwinputten Overijssel*. z3014. WL—Delft Hydraulics.

Mastbergen, D. (2009). *Stabiliteitsanalyse zandwinning Oosterweilanden*. 1002701. Deltares.

Mastbergen, D. R., A. Bezuijen, and J. C. Winterwerp (1988). "On the construction of sand fill dams. 1: Hydraulic aspects". In: *Modelling Soil–Water Structure Interactions*. International Association for Hydro-Environment Engineering and Research, pp. 353–362.

Mei, R. (1994). "Effect of turbulence on the particle settling velocity in the nonlinear drag range". In: *International Journal of Multiphase Flow* 20.2, pp. 273–284. DOI: https://doi.org/10.1016/0301-9322(94)90082-5.

Meijer, K. L. and A. G. van Os (1976). "Pore pressures near moving underwater slope". In: *Journal of the Geotechnical Engineering Division*, pp. 361–372.

Moin, P. and K. Mahesh (1998). "Direct numerical simulation: a tool in turbulence research". In: *Annual review of fluid mechanics* 30.1, pp. 539–578. DOI: 10.1146/annurev.fluid.30.1.539.

Murray, S. P. (1970). "Settling velocities and vertical diffusion of particles in turbulent water". In: *Journal of geophysical research* 75.9, pp. 1647–1654. DOI: 10.1029/JC075i009p01647.

Nabi, M., H. De Vriend, E. Mosselman, C. Sloff, and Y. Shimizu (2013). "Detailed simulation of morphodynamics: 2. Sediment pickup, transport, and deposition". In: *Water resources research* 49.8, pp. 4775–4791. DOI: 10.1002/wrcr.20303.

Nakagawa, H. and T. Tsujimoto (1980). "Sand bed instability due to bed load motion". In: *Journal of the Hydraulics Division* 106.12, pp. 2029–2051.

Nedelec, Y. and J. Revel (May 2015). "Phénomènes d'érosion côtière : instabilité et consolidation de talus littoraux sur la façade est du cap Ferret (Gironde)". In: *Rencontres Universitaires de Génie Civil*. Bayonne, France.

O'Donovan, E. and R. Tanner (1984). "Numerical study of the Bingham squeeze film problem". In: *Journal of Non-Newtonian Fluid Mechanics* 15.1, pp. 75–83. DOI: 10.1016/0377-0257(84)80029-4.

Oñate, E., M. A. Celigueta, S. R. Idelsohn, F. Salazar, and B. Suárez (2011). "Possibilities of the particle finite element method for fluid–soil–structure interaction problems". In: *Computational Mechanics* 48.3, p. 307. DOI: 10.1007/s00466-011-0617-2.

Padfield, C. J. (1978). "The stability of river banks and flood embankments". PhD thesis. University of Cambridge.

Pailha, M. and O. Pouliquen (2009). "A two-phase flow description of the initiation of submarine granular avalanches". In: *Journal of Fluid Mechanics* 633, pp. 115–135. DOI: 10.1017/S0022112009007460.

Papanastasiou, T. C. (1987). "Flows of Materials with Yield". In: *Journal of Rheology* 31.5, pp. 385–404. DOI: 10.1122/1.549926. eprint: http://sor.scitation.org/doi/pdf/10.1122/1.549926.

Paphitis, D. (2001). "Sediment movement under unidirectional flows: an assessment of empirical threshold curves". In: *Coastal Engineering* 43.3, pp. 227–245. DOI: 10.1016/S0378-3839(01)00015-1.

Pastor, J., T.-H. Thai, and P. Francescato (2000). "New bounds for the height limit of a vertical slope". In: *International Journal for Numerical and Analytical Methods in Geomechanics* 24.2, pp. 165–182. DOI: 10.1002/(SICI)1096-9853(200002)24:2<165::AID-NAG62>3.0.CO;2-A.

Patankar, N. and D. Joseph (2001). "Modeling and numerical simulation of particulate flows by the Eulerian–Lagrangian approach". In: *International Journal of Multiphase Flow* 27.10, pp. 1659–1684. DOI: 10.1016/S0301-9322(01)00021-0.

Patankar, S. V. and D. B. Spalding (1972). "A calculation procedure for heat, mass and momentum transfer in three-dimensional parabolic flows". In: *International journal of heat and mass transfer* 15.10, pp. 1787–1806. DOI: 10.1016/0017-9310(72)90054-3.

Poroseva, S. and H. Bezard (2001). "On ability of standard k-epsilon model to simulate aerodynamic turbulent flows". In: *CFD J* 9, pp. 464–470.

Prandtl, L. (1949). *Report on investigation of developed turbulence. Translation of "Bericht über Untersuchungen zur ausgebildeten Turbulent." Zeitschrift für angewandte Mathematik und Mechanik, vol. 5, no. 2, April 1925.* National Advisory Committee for Aeronautics.

Reynolds, O. (1885). "LVII. On the dilatancy of media composed of rigid particles in contact. With experimental illustrations". In: *The London, Edinburgh, and Dublin Philosophical Magazine and Journal of Science* 20.127, pp. 469–481. DOI: 10.1080/14786448508627791.

Rhee, C. van and A. M. Talmon (2010). "Sedimentation and erosion of sediment at high solids concentration". In: *Proceedings of the 18th International Conference on Hydrotransport.* BHR Group, Cranfield, UK, pp. 211–222.

Rhie, C. M. and W. L. Chow (1983). "Numerical study of the turbulent flow past an airfoil with trailing edge separation". In: *AIAA journal* 21.11, pp. 1525–1532.

Richardson, J. and W. Zaki (1954). In: *Chemical Engineering Science*, pp. 65–73. DOI: 10.1016/0009-2509(54)85015-9.

Rijkswaterstaat (Mar. 2017). *Strandval op westkust Ameland.* URL: https://www.rijkswaterstaat.nl/over-ons/nieuws/nieuwsarchief/p2017/03/strandval-op-westkust-Ameland.aspx (visited on 07/21/2018).

Rondon, L., O. Pouliquen, and P. Aussillous (2011). "Granular collapse in a fluid: role of the initial volume fraction". In: *Physics of Fluids* 23.7, p. 73301. DOI: 10.1063/1.3594200.

Roux, S. and F. Radjaï (2002). "Statistical Approach to the Mechanical Behavior of Granular Media". In: *Mechanics for a New Mellennium*. Ed. by H. Aref and J. W. Phillips. Dordrecht: Springer Netherlands, pp. 181–196. DOI: 10.1007/0-306-46956-1_12.

Rowe, P. W. (1962). "The stress-dilatancy relation for static equilibrium of an assembly of particles in contact". In: *Proceedings of the Royal Society of London. Series A. Mathematical and Physical Sciences* 269.1339, pp. 500–527. DOI: 10.1098/rspa.1962.0193.

Runge, A. (1999). "Eendimensionale beschouwing van de bezinking van hooggeconcentreerde zandwatermengsels onder turbulente omstandigheden". Master's thesis. Delft University of Technology.

Schlatter, P. and R. Örlü (2010). "Assessment of direct numerical simulation data of turbulent boundary layers". In: *Journal of Fluid Mechanics* 659, pp. 116–126. DOI: 10.1017/S0022112010003113.

Schofield, A. and P. Wroth (1968). *Critical state soil mechanics*. Vol. 310. McGraw-Hill London.

Shepard, F. P. (1951). "Mass movements in submarine canyon heads". In: *Eos, Transactions American Geophysical Union* 32.3, pp. 405–418. DOI: 10.1029/TR032i003p00405.

Shields, A. (1936). *Anwendung der Aehnlichkeitsmechanik und der Turbulenzforschung auf die Geschiebebewegung*. Tech. rep. Preussischen Versuchsanstalt für Wasserbau.

Shipway, I. (Nov. 25, 2015). *Risks associated with nearshore instability Inskip Point, Qld*. Technical Report. EDG Consulting Pty Ltd.

Soulsby, R. L. and R. J. S. Whitehouse (1997). "Threshold of sediment motion in coastal environments". In: *Pacific Coasts and Ports' 97: Proceedings of the 13th Australasian Coastal and Ocean Engineering Conference and the 6th Australasian Port and Harbour Conference; Volume 1*. Centre for Advanced Engineering, University of Canterbury, p. 145.

Tavoularis, S. and S. Corrsin (1981). "Experiments in nearly homogenous turbulent shear flow with a uniform mean temperature gradient. Part 1". In: *Journal of Fluid Mechanics* 104, pp. 311–347. DOI: 10.1017/S0022112081002930.

Taylor, D. W. (1948). *Fundamentals of soil mechanics*. Chapman and Hall, Limited.; New York.

Torrey III, V. H., J. B. Dunbar, and R. W. Peterson (1988). *Retrogressive Failures in Sand Deposits of the Mississippi River. Report 1. Field Investigations, Laboratory Studies and Analysis of the Hypothesized Failure Mechanism*. Tech. rep. Army Engineer Waterways Experiment Station Vicksburg MS Geotechnical Lab.

Turton, R. and O. Levenspiel (1986). "A short note on the drag correlation for spheres". In: *Powder technology* 47.1, pp. 83–86. DOI: 10.1016/0032-5910(86)80012-2.

van den Berg, J., A. Martinius, and R. Houthuys (2017). "Breaching-related turbidites in fluvial and estuarine channels: Examples from outcrop and core and implications to reservoir models". In: *Marine and Petroleum Geology* 82, pp. 178–205. DOI: 10.1016/j.marpetgeo.2017.02.005.

van den Berg, J. H., A. van Gelder, and D. R. Mastbergen (2002). "The importance of breaching as a mechanism of subaqueous slope failure in fine sand". In: *Sedimentology* 49.1, pp. 81–95. DOI: 10.1111/j.1525-139X.2006.00168.x-i1.

van der Ruyt, M., M. de Groot, and D. Mastbergen (2008). *Depot Hollandsch Diep. Analyse taludinstabiliteiten en faalkans in exploitatiefase*. Deltares.

van Rhee, C. (2002). "On the sedimentation process in a Trailing Suction Hopper Dredger". PhD thesis. Delft University of Technology.

van Rhee, C. (2010). "Sediment entrainment at high flow velocity". In: *Journal of Hydraulic Engineering*, pp. 572–582. DOI: 10.1061/(ASCE)HY.1943-7900.0000214.

van Rhee, C. and A. Bezuijen (1998). "The breaching of sand investigated in large-scale model tests". In: *Coastal Eengineering Conference*. American Society of Civil Engineers, pp. 2509–2519. DOI: 10.1061/9780784404119.189.

Van Rhee, C. (2002). "The Influence of the Bed Shear Stress on the Sedimentation of sand". In: *11th International Symposium on Transport and Sedimentation of Solid Particles, Gent, Belgium*.

van Rhee, C. (2015). "Slope failure by unstable breaching". In: *Proceedings of the Institution of Civil Engineers-Maritime Engineering*. Vol. 168. 2. Thomas Telford Ltd, pp. 84–92.

van Rhee, C. and A. Bezuijen (1992). "Influence of seepage on stability of sandy slope". In: *Journal of Geotechnical Engineering* 118.8, pp. 1236–1240. DOI: 10.1061/(ASCE)0733-9410(1992)118:8(1236).

van Rijn, L. C. (1984). "Sediment pick-up functions". In: *Journal of Hydraulic Engineering* 110.10, pp. 1494–1502. DOI: 10.1061/(ASCE)0733-9429(1984)110:10(1494).

Vand, V. (1948). "Viscosity of Solutions and Suspensions. II. Experimental Determination of the Viscosity–Concentration Function of Spherical Suspensions". In: *The Journal of Physical and Colloid Chemistry* 52.2, pp. 300–314. DOI: 10.1021/j150458a002. eprint: http://dx.doi.org/10.1021/j150458a002.

Vanoni, V. A. (1975). *Sedimentation engineering*. American Society of Civil Engineers. DOI: 10.1061/9780784408230.

Verdugo, R. and K. Ishihara (1996). "The steady state of sandy soils". In: *Soils and foundations* 36.2, pp. 81–91. DOI: 10.3208/sandf.36.2_81.

Wachem, B. G. M. van, J. C. Schouten, C. M. van den Bleek, R. Krishna, and J. L. Sinclair (2004). "Comparative analysis of CFD models of dense gas–solid systems". In: *AIChE Journal* 47.5, pp. 1035–1051. DOI: 10.1002/aic.690470510.

Wan, R. and P. Guo (1999). "A pressure and density dependent dilatancy model for granular materials". In: *Soils and Foundations* 39.6, pp. 1–11. DOI: 10.3208/sandf.39.6_1.

Wang, C., Y. Wang, C. Peng, and X. Meng (2017). "Dilatancy and compaction effects on the submerged granular column collapse". In: *Physics of Fluids* 29.10, p. 103307. DOI: 10.1063/1.4986502.

Weller, H. G., G. Tabor, H. Jasak, and C. Fureby (1998). "A tensorial approach to computational continuum mechanics using object-oriented techniques". In: *Computers in physics* 12.6, pp. 620–631.

Winterwerp, J. C., W. T. Bakker, D. R. Mastbergen, and H. van Rossum (1992). "Hyperconcentrated sand-water mixture flows over erodible bed". In: *Journal of Hydraulic Engineering* 118.11, pp. 1508–1525. DOI: 10.1061/(ASCE)0733-9429(1992)118:11(1508).

Xingkui, W. and Q. Ning (1989). "Turbulence Characteristics of Sediment-Laden Flow". In: *Journal of Hydraulic Engineering* 115.6, pp. 781–800. DOI: 10.1061/(ASCE)0733-9429(1989)115:6(781).

You, Y., P. Flemings, and D. Mohrig (2012). "Dynamics of dilative slope failure". In: *Geology* 40.7, pp. 663–666. DOI: 10.1130/G32855.1.

You, Y., P. Flemings, and D. Mohrig (2013). "Dynamics of dilative slope failure". PhD thesis. The University of Texas at Austin, pp. 663–666. DOI: 10.1130/G32855.1.

You, Y., P. Flemings, and D. Mohrig (2014). "Mechanics of dual-mode dilative failure in subaqueous sediment deposits". In: *Earth and Planetary Science Letters* 397, pp. 10–18. DOI: 10.1016/j.epsl.2014.04.024.

Zalesak, S. T. (1979). "Fully multidimensional flux-corrected transport algorithms for fluids". In: *Journal of Computational Physics* 31.3, pp. 335–362. DOI: 10.1016/0021-9991(79)90051-2.

Zeng, Z. and R. Grigg (Apr. 2006). "A Criterion for Non-Darcy Flow in Porous Media". In: *Transport in Porous Media* 63.1, pp. 57–69. DOI: 10.1007/s11242-005-2720-3.

Zienkiewicz, O. C., R. L. Taylor, O. C. Zienkiewicz, and R. L. Taylor (1977). *The finite element method*. Vol. 3. McGraw-Hill London.

Curriculum Vitae

Dave Weij was born in Amstelveen on January 10th, 1988. In 2007 he completed his high school education at Alkwin Kollege Uithoorn. In the same year he started his Bachelor in Civil Engineering at the Delft University of Technology, which he completed in 2010. In 2010 he started his Master in Civil Engineering at the Hydraulic Engineering department at the same university. Under the supervision of dr.ir. E. Mosselman he wrote his master thesis on 'The interaction between bed-load transport and dune orientation'. In 2012 he obtained is M.Sc. degree cum laude. In 2013 he started as Ph.D. student at the Maritime and Transport Technology department of the Delft Univeristy of Technology. In 2019 he started working as software engineer for Plaxis bv, in Delft.

List of Publications

- An Approach to Research of the Breaching Process, 2016, World Dredging Conference XXI, At Miami, FL, USA
- An Extension Of The Drift-flux Model For Submarine Granular Flows, 2016, International Journal of Computational Methods and Experimental Measurements

Acknowledgements

First, I would like to express my appreciation to my promotor Cees van Rhee and copromotor Geert Keetels without whom this research would not have been possible. I would also like to thank them for always being available for advice and encouragement, and for staying positive when I was often more negative.

I want to thank Joep Goeree for sharing his valuable knowledge on numerical modelling and in particular on the mixture model.

I am grateful for the invaluable help of Freek Brakel and Ed Stok during the laboratory experiments.

I am thankful to Dick Mastbergen and Geeralt van den Ham of Deltares, Ronald van der Hout and Joop van der Meer of van Oord, Ike van Giffen and Richard de Jager of Boskalis, and Paul Cools and Koos Saathof of Rijkswaterstaat, for their support and advice from a less academic and more practical viewpoint.

I want to acknowledge the secretaries of the Maritime and Transport Technology department, Pauline, Anouk, Monique and Patty, for their valuable support.

I want to thank my fellow PhD candidates, Bas, Frans, Lynyrd, Xiuhan, Ershad, Rudy, Jort, Rik, Ralf, Thijs, Jian, and Stefano, for the many interesting discussions on a wide range of topics during our lunch/coffee/drink breaks.

I would like to thank several people from the Numerical analysis group, Reinaldo, Manuel, Gaby, Luis, Fahim, Abdul, Roel, Baljinnyam, Lisa, Behrouz, and Mohamed, for accepting me as an honorary member. Thanks also go out to the rest of the Krylov Tigers: Sławek, Keshav, Nirmal, Shuaiqiang, Soumya, Wissam, and Tómas. And other fellow Ph.D and post-docs not belonging to these groups: Lorenzo, Eduardo, Swej, Michele, Jiakun, Boris.

A special thanks go out to Bishnu Raj Baral and Umesh Singh, for their help during my stay in Nepal.

I want to thank the players of D.S.V. Full Speed 4, for many fun days battling against relegation, especially Jeroen en Michel, for sacrificing many hours of their free time organizing things.

I also want to thank my family for their support and patience.

And finally I want to thank the most important person, Chiara, for your unconditional support and encouragement, and for always being there to listen to my complaints and putting me at ease. I might not have finished this thesis without you.